IMPLEMENTING RADIOSTEREOMETRIC ANALYSIS IN A LOW DOSE BIPLANAR SLOT SCANNER

by

Saad Rehan

Submitted in partial fulfilment of the requirements
for the degree of Master of Applied Science

at

Dalhousie University
Halifax, Nova Scotia
December 2015

© Copyright by Saad Rehan, 2015

TABLE OF CONTENTS

LIST OF TABLES

LIST OF FIGURES

ABSTRACT

Slipped Capital Femoral Epiphysis (SCFE) is a condition affecting young adolescents in which the proximal femoral metaphysis 'slips' in relation to the capital epiphysis. If left untreated, children are at an increased risk of developing avascular necrosis and secondary osteoarthritis. In-situ fixation remains central in the standard of care. Conventional radiography does not afford accurate post-surgical assessment of physeal fusion; leading to avascular necrosis in cases of persistent physeal non-union. Therefore, a clinical need exists to accurately quantify post-surgical physeal micromotion as an indicator of surgical success. RadioStereometric Analysis (RSA) offer better accuracy than conventional radiography, but requires serial X-ray exams increasing cumulative radiation exposure, concerning in paediatric populations. In the pursuit of the As Low As Reasonably Achievable (ALARA) principle and predominantly in the paediatric realm, there is a need to reduce radiation dose; the EOS imager offers to redefine ALARA. The EOS imager is a biplanar imaging system with three-dimensional capabilities and has demonstrated radiation reduction of 6 to 9 times depending on anatomical location. The purpose of this thesis was to uniquely demonstrate the RSA technique in the EOS imager.

A phantom study was conducted to compare RSA accuracy and precision in the digital flat-panel and the EOS imaging modalities. The accuracy and precision of RSA in the EOS imager and in the standard technique was better than 0.05mm±0.06mm and 0.37°±0.36° and 0.07mm±0.05mm and 0.18°±0.32°, respectively. The phantom study demonstrated RSA accuracy and precision deemed acceptable for successful post-surgical physeal micromotion assessment in the EOS modality.

Next, a human study was conducted to demonstrate the feasibility of the RSA technique in the EOS imager in human subjects, and to provide an indication of the precision of the system. Three subjects were recruited from an on-going Total Knee Arthroplasty (TKA) research study at the local hospital. Employing a zero displacement double exam protocol, subjects were imaged in the EOS imager. The precision of EOS RSA was better than ±0.84mm and ±0.91°, near the limit of accepted RSA precision and was confounded by patient motion during EOS scans.

This thesis is the first demonstration of the EOS RSA technique and the results of the thesis suggest acceptable accuracy in quantifying post-surgical SCFE micromotion. Improvements in precision can be explored with patient restraints. This technique can then be used to quantify post-surgical longitudinal micromotion or instantaneous micromotion with an inducible displacement protocol. Metrics stemming from the increasing employment of this assessment technique can be used to indicate post-surgical stability and outcomes in the SCFE population.

LIST OF ABBREVIATIONS USED

CAD	-	Computer Aided Design
CN	-	Condition Number
CT	-	Computed Tomography
DLT	-	Direct Linear Transform
EOS	-	Biotech Company Headquartered in Paris, France
FOV	-	Field of View
GCS	-	Global Coordinate System
kVp	-	kiloVoltage Potential
LCS	-	Local Coordinate System
LoCS	-	Limits of Clinical Significance
mAs	-	milliAmpere seconds
MERBF	-	Mean Error Of Rigid Body Fitting
MB-RSA	-	Model Based RSA Software by RSAcore, Leiden, The Netherlands
PI	-	Prediction Interval
POV-Ray	-	Persistence of Vision Raytracer developed by Persistence of Vision Raytracer Pty. Ltd.
RSA	-	Radio Stereometric Analysis
RMSE	-	Root Mean Square Error
SCFE	-	Slipped Capital Femoral Epiphysis
SD	-	Standard Deviation
TKA	-	Total Knee Arthroplasty
THA	-	Total Hip Arthroplasty

GLOSSARY

Accuracy
closeness of agreement between a measurement result and the true value. Accuracy refers to a combination of trueness and precision. Accuracy was based on the 95% Prediction Intervals (Onsten et al. 2001; Madanat et al. 2005). In this application, the micrometer is the accepted reference or true value and the output of the RSA technique is the measurement result.

Aligned Pose

The phantom anatomical axes aligned with the axes of the RSA environment.

Control Marker

Markers used in the standard technique, on the calibration box, to determine the x-ray foci.

Condition Number

A measure of the non-linearity of a marker cluster. The Condition Number equation is presented where *d* is the distance between markers and a line propagating through the cluster which minimizes said distances (ISO 16087:2013).

Condition Number: Equation $$CN = \frac{1}{\sqrt{d_1^2 + d_2^2 + \cdots + d_n^2}}$$

Centroid

The geometric center of a bead cluster.

Crossing Line Distance

The shortest norm of the vector connecting two marker projections (ISO 16087:2013).

Fiducial Markers

Marker cluster on the calibration box, in the standard technique, used to define the global coordinate system.

Global coordinate system

The coordinate system of the RSA environment; defined by the calibration box in the standard technique and by the lowest plane capable of being imaged in the EOS imager.

Inducible Displacement

Micromotion induced between bone segments with load modulation. Synonymous with reversible displacement (Green et al, 1983).

Local coordinate system

An orthogonal coordinate system defined by anatomical features.

Phantom Model

A physical anatomical model built to simulate in-vivo conditions.

Precision

Likened to a system's repeatability. Based on 95% confidence interval of measurement results from each RSA techniques (ISO 16087:2013).

Repeatability

The degree of confluence of RSA measurements obtained in identical conditions.

Revision

Repeated surgery following rise of clinical complications.

Right-handed coordinate system

A 3-dimensional coordinate system which satisfies the right-hand rule.

Rigid Body Error

The root mean square error in 3d positions of bead clusters between time points (ISO 16087:2013).

Slipped Capital Femoral Epiphysis

Decreased in osseous integrity in the capital femoral epiphysis resulting in slippage.

Matched Markers

Implanted RSA beads visible and matched on both stereo images

Maximum Total Point Motion

The norm of the translation vector of the marker with the largest migration (ISO 16087:2013).

Long-term Migration

Irreversible subsidence of implant in bone spanning extended time periods.

Micromotion

Small relative motions at the implant-bone interface or between bone segments.

ACKNOWLEDGEMENTS

I am deeply indebted to my supervisors, Dr. Ron El-Hawary and Dr. Janie Astephen-Wilson, for imparting their expertise and countless insight into this project.

I would like to thank my Dr. Edward Valstar and Dr. Michael Dunbar for their time and effort spent reviewing the work of this thesis.

I am very grateful for the help Alan, Jen, Steve, Elise and Benoit provided. All of their help was fundamental in the success of this project.

I would like to acknowledge the DOHM group and SBME for making grad school a very enjoyable experience.

I would like to express my deep gratitude for the endless support my parents and sisters have provided me throughout this undertaking. I dedicate this work to them.

Chapter 1: Introduction

Overview

Slipped Capital Femoral Epiphysis (SCFE) is a common adolescent disorder of the hip joint with a prevalence of 10.8 cases for 100,000 children in the United States. The disorder affects children ranging from eight to 15 years in age and the ratio of prevalence in males to females is 3:2 (Loder, 1996). The disorder is linked to obesity, peak growth velocity and trauma. Endocrine disorders are also associated with prevalence of this disorder. Clinical presentation includes grossly localized pain in the inner thigh, groin, hip and knee. SCFE is characterized by a Trendelenburg gait and in severe cases inability to ambulate. The untreated condition can lead to avascular necrosis of the proximal femur and deterioration of the hip joint cartilage, increasing likelihood of developing coxarthrosis in later life (Ordeberg et al. 1987). Surgical intervention is the current standard of care and in-situ fixation remains the most effective method (Wensaas et al. 2011). Current radiographic techniques assessing successful bone fusion in post-surgical patients fail to provide sufficient accuracy and expose children to repeated x-ray exams at an early age. Surgical revision is usually dictated by the rise of post-surgical complications further deteriorating the affected hip joint. There is a need for high accuracy technique allowing early detection of physeal disunion. One such technique is Radiostereometric Analysis (RSA).

Radiostereometric analysis, pioneered by (Selvik 1989), has been used to quantify post-surgical implant-related micromotion as an indicator of implant stability. Using stereo x-rays at two time points, it is a method to track migration of bony landmarks and/or implanted hardware. This migration is linked then to implant stability. There have been several previous successful attempts to link post-operative implant migration to implant survivorship (Ryd et al. 1995; Karrholm et al. 1994; Pijls et al. 2012). This technique requires serial radiographic exposures, increasing the cumulative dose each subject is exposed to. Although, relatively common in adult populations, there has been limited application of RSA in the paediatric population. One plausible reason is the x-ray radiation dose inherent in this technique. Cumulative x-ray radiation over one's lifetime has been linked to increased prevalence of cancer later on in life (Ronckers et al. 2010). There exists a need to demonstrate this highly accurate technique in a lower radiation dose modality before implementation in paediatric population.

A novel low radiation dose biplanar x-ray slot scanner, the EOS imager, is one such alternative imaging modality. Based on a new particle detector, developed by Georges Charpak, awarding him the 1992 Nobel prize in physics, the EOS imager is a biplanar imaging system with 3D capabilities. It has demonstrated reduced radiation dose by 6-9 times compared to computed radiography depending on anatomical location (Deschênes et al. 2010). The x-ray sources and detectors are mounted on a C-arm which vertically descends during a scan. This allows 1:1 magnification full body standing images providing its own diagnostic value.

The aim of this thesis is to demonstrate the RSA technique in the low radiation dose EOS imager. The advantage of the technique lies in the reduced radiation dose of the EOS modality, which is particularly desirable for adolescent surgical outcome assessment, as well as the improved accuracy and precision of RSA for fusion assessment. RSA combined with EOS will allow for earlier and improved ability to predict post-surgical problems such as non-union, allowing for earlier, and therefore more successful, intervention.

Owing to the limited application of RSA in paediatric population, there has been no previously known application of RSA in the paediatric hip. This thesis will be the first to implement RSA in the EOS imaging modality (Chapter 3). Using the SCFE model, the fixation screw and dimensional constraints of the proximal femur are hypothesized to be challenges in the implementation of this technique. The conventional technique relies on instantaneous exposure of x-ray sources to capture stereo radiographs. The effect of vertical translation of the EOS C-arm on the accuracy of the RSA technique will be investigated in this study. The effects of larger pixel size of the EOS imager compared to the flat panel detector will also be investigated. A human study will be conducted to characterize the in-vivo precision of this technique (Chapter 4). Patient motion artefact stemming from delayed exposure time, on the order of several seconds, is hypothesized to negatively affect the precision.

This thesis aims to provide part of the framework in developing a longitudinal or instantaneous post-surgical fusion assessment protocol employing the EOS RSA technique and a hip inducible displacement protocol; ultimately allowing the development of metrics associated with physeal fusion in the post-surgical SCFE population.

1.1 Slipped Capital Femoral Epiphysis

Slipped capital femoral epiphysis (SCFE) is a term used to describe a pediatric condition affecting the femur. In healthy individuals the osseous integrity of the proximal femoral physis is resilient to rigorous load. “Slippage” in SCFE occurs through compromised structural integrity of this physis and results in the relative displacement of proximal femoral metaphysis and epiphysis (Wheeless 2011). Compromised structural integrity is linked to obesity, pubertal peak growth velocity and endocrinopathies (Witbreuk et al., 2013). A radiograph of a normal and SCFE femoral head is illustrated in Figure 1.

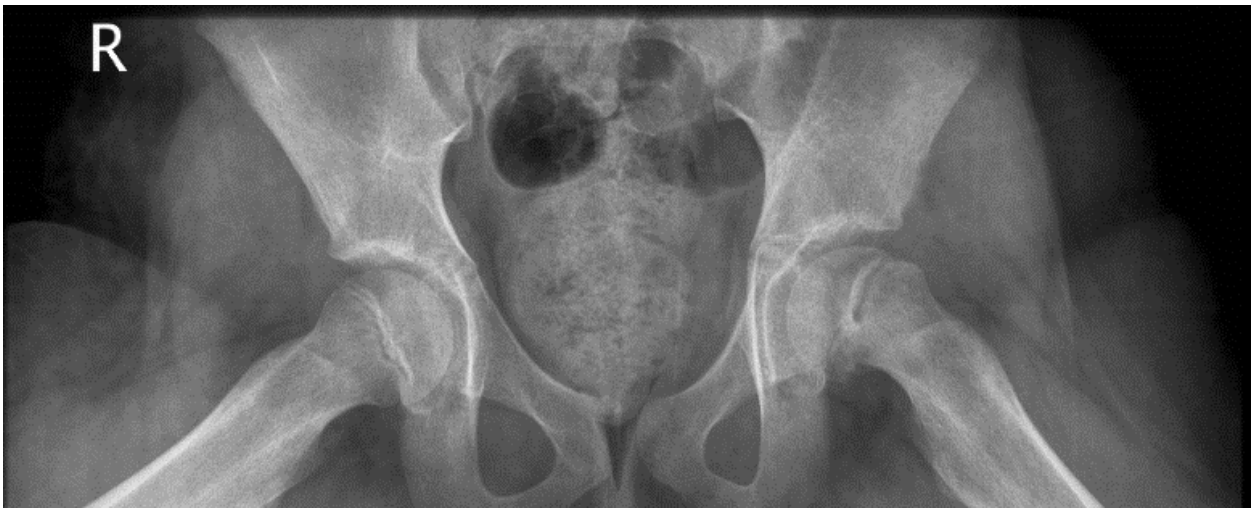

Figure 1: Radiograph of a healthy (right) and a SCFE (left) femoral head.

The lack of mechanical strength across the physis, often combined with abnormally high load through the femur sometimes stemming from obesity, results in bone deformation. The metaphysis “slips” and moves in the anteriosuperior direction while also undergoing external rotation (Wheeless 2011). This shearing motion produces pain and variations in gait including increased pelvic obliquity, step width, hip external rotation, external foot progression angle, and decreased knee flexion (Song, et al. 2004). Invariably, the blood supply to the cancellous bone is fragile and increases in risk of being obstructed as the “slipping” progresses (Wheeless 2011).

1.1.1 Demographics

A recent review suggests the prevalence of SCFE to be between 0.33 and 24.58 per 100,000 children 8 to 15 years in age (Loder & Skopelja 2011). SCFE more commonly affects young male adolescents with a ratio of 3:2 males to females (Wheeless 2011). It is most

prevalent in males during ages 12 to 16 years and females during ages 10 to 15 years. African and Polynesian heritage and obesity are prominent disposing factors in the development of this disease (Loder & Skopelja 2011). No conclusive theory exists explaining the discrepancy in the increased occurrence of SCFE in males; however, researchers have indicated that the bone resorption effect of testosterone may favourably decrease physis integrity in males (Witbreuk et al. 2013).

1.1.2 Classification

Loder and others (1993) suggest ambulatory patients be classified as stable and those unable to weight bear with or without assistance classified as unstable. Without surgical intervention, less than 10% risk of osteonecrosis exists for stable SCFE patients while this increases to 47% for unstable patients (Loder et al. 1993). The increased risk of osteonecrosis in unstable cases stems from higher likelihood of the retrograde blood supply withdrawal as slipping increases.

Acute cases present with symptoms ranging below 3 weeks. Chronic slips are more common and present with symptoms existing for more than 3 weeks. Acute on chronic slips occur following an acute exacerbation (i.e. trauma) and in most cases present with no symptoms prior to the exacerbation (Wheeless 2011).

The Southwick Slip Angle is also used to classify severity of slippage (Figure 2). The Southwick Angle, also known as the epiphyseal-shaft angle, is the angle, in frog-lateral view, between the axis of the femoral shaft and the line perpendicular across the physis. This classification is divided into mild with an angle of less than 30°, moderate for an angle between 30° and 60°, while severe is an angle greater than 60° (Wheeless 2011). Frog lateral is a supine radiograph obtained while the hip is abducted 45° and the knee is flexed 40° (Clohisy et al. 2007).

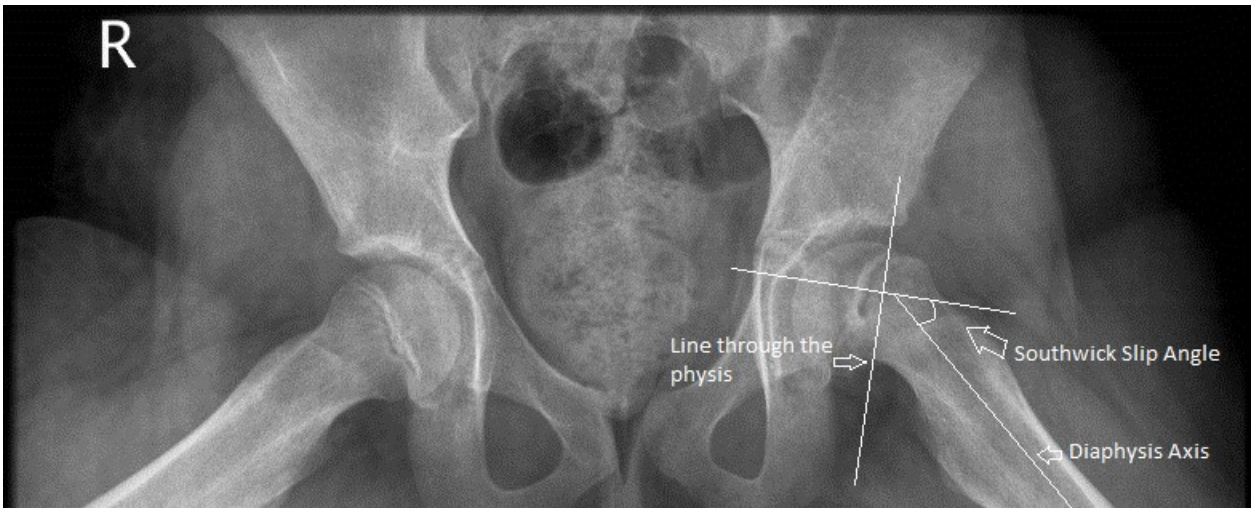

Figure 2: A radiograph illustrating the Southwick Slip Angle of a SCFE patient.

1.1.3 Clinical Presentation

This condition is associated with widespread unlocalized pain in the joints of the affected lower extremity. Pain is predominantly present in inguinal area, however; also in the knee, hip and medial thigh. Pain may also only occur during retroversion of the lower extremity. Some mild cases present with painless limps, and serious cases present with inability to weight bear or ambulate. Bilateral slips occur in about 17-50% of previously unilateral diagnosed patients with the second slip occurring within 6 months of the first (Wheeless 2011).

1.1.4 Etiology

One international multicenter study found 65% of SCFE patients were in the 95 percentile of the weight for their respective age group. Endocrinopathies, including but not limited to, hypothyroidism, growth hormone deficiency and hypogonadism increase risk of developing SCFE and increase the risk of bilateral slippage. Trauma, often combined with the aforementioned, can result in SCFE (Loder et al. 1996).

Several mechanical factors have been linked to etiology. Increasing relative femoral retroversion, coxa valga, an increased relative femur neck-shaft angle, and thinning of the perichondrial ring. The perichondrial ring is a chondrocytic ring encircling the physis, with the aim of providing mechanical stability to the proximal femur during growth (Wheeless 2011).

1.1.5 Treatment

Blood supply to the trabecular bone in 20% of severe SCFE cases withdraws leading to necrosis, hypoxia and vascular destruction (Sankar et al. 2010). To decrease the risk of blood supply withdrawal and to maintain osseous vitality surgeons recommend halting further slippage in place of corrective measures (Souder et al. 2014). Therefore, clinical treatment is mostly limited to in-situ fixation. The use of multiple implants has been linked to increased risk of trabecular bone necrosis (Riley et al. 1990; Tokmakova, et al. 2003). Prophylactic pinning of the contralateral hip is usually recommended in cases with endocrine disorders, early occurrence of slip (less than 10 years old) and obesity (Kocher et al. 2004).

Recently, screws extendable in length corresponding to femoral expansion following pubescent growth spurts have been introduced into the market. This is particularly desirable as osseous deformation in response to growth increases the susceptibility of bone-implant uncoupling in conventional fixation screws (Dujovne et al. 2014). Conventional radiography provides challenges in characterizing growth or bone-implant uncoupling following fixation with extendable screws.

1.1.6 Limitations

Surgeons are currently unable to reliably determine the presence of physeal fusion post operatively. Prognosis and recommendations for return to weight bearing and unrestricted activity are based predominantly on anecdotal evidence. Generally, surgeons recommend strenuous activity cessation and reduced weight bearing on the affected hip ranging between 3 and 6 months, postoperatively. There exists a need for surgeons to determine prognosis and recommend lifestyle modifications based on an accurate post-operative physeal fusion assessment protocol.

The overall risk of slip progression despite surgical intervention is less than 10% (Wheeless 2011). Nevertheless, surgeons need to determine physeal non-fusion so corrective intervention is performed in surgical failure cases before the rise of clinical complications. Case reports have been published that indicate the need to determine the presence of physeal fusion after in situ pinning. In one such report, an obese 15-year-old boy with uncomplicated in situ pinning had the pins removed after 11 weeks. The symptoms returned several months later and

radiographs reveled severe SCFE of 70° (Engelsma et al. 2012). Similarly, in the same report a 13-year-old female with mild SCFE underwent in situ pinning. Mild pain persisted and the pin was removed four months post operatively. The slip progressed to 50° and underwent revision surgery. Another case report presents the slip progression in a child undergoing thyroid hormone replacement therapy (Walter et al. 2013). This report highlights the confounding nature of endocrine disorders in affecting the success and time to success of physeal fusion; both of which have yet to be elucidated. A group reporting on two unsuccessful physeal fusion cases, point to possible micromotion existing across the physis manifesting in non-fusion. In this report one patient, after hip trauma, presented with broken screws and another patient after one year revealed radiographic evidence of physeal non-fusion. The researchers were unable to assess this micromotion but pointed to its existence due to persistence of bone non-union. The persistence of physeal non-fusion is hypothesized to be facilitated by micromotion across the physis by the authors (Murphy et al. 2013). In all discussed cases there exists a need to determine the presence of physeal fusion after in situ fixation to avoid slip progression and clinical complications which is currently unable to be detected with standard radiography. Specifically, these case reports show visual inspection of radiographs is an unreliable method to determine surgical failure. Visual inspection offers a translational accuracy of 2.5 mm. This detection threshold combined with an inter-observer variability of ±2.5 mm equates to a movement of at least 5.0 mm to confirm movement in standard hip radiographs (Sutherland, et al., 1982). The level of detection needed to assess micromotion at the bone implant interface of SCFE patients is currently unknown however, the physiological growth rate of the capital femoral physis during periods of rapid growth is 0.7 mm per six weeks (Shapiro 2002). The level of micromotion is hypothesized to exist below the detection threshold afford by conventional radiography. An accurate method is required to determine physeal fusion in the post-operative SCFE population. RadioStereometric Analysis (RSA) is a method to determine relative rigid body movement and offers improved accuracy over visual inspection. It is hypothesized in this thesis the accuracy offered by RSA in determining micromotion will allow for reliable physeal assessment in the post-surgical SCFE population.

1.2 Radiostereometric Analysis

Radiostereometric Analysis or RSA, also known as Roentgen Stereophotogrammetric Analysis, is a stereo X-ray technique in orthopaedic applications to characterize relative motion between rigid bodies. Its current embodiment is credited to Selvik G. from 1989. The technique requires identifying points of interest in rigid bodies from two perspectives. This stereo regimen allows the three-dimensional representation of rigid bodies in space. Tracking bodies in the time domain allows the characterization of motion.

1.2.1 Description

The RSA technique is based on photogrammetry; which, in the orthopaedic application, is the study of geometrical transformation dictating the spatial representation of an implant on stereo radiographs and utilizing them to reconstruct the implant in Euclidian space. Radio in RSA refers to using roentgen or x-ray beams. The radiographic presentation and the geometric properties and location of implant in Euclidean space are related by systems of equations known as Direct Linear Transform (DLT) (Selvik 1989).

The x-ray beam configuration in the standard imager is a cone beam and exhibits scatter along all axes as it propagates from the source. Figure 3 illustrates the configuration of the x-rays utilized in the standard imager.

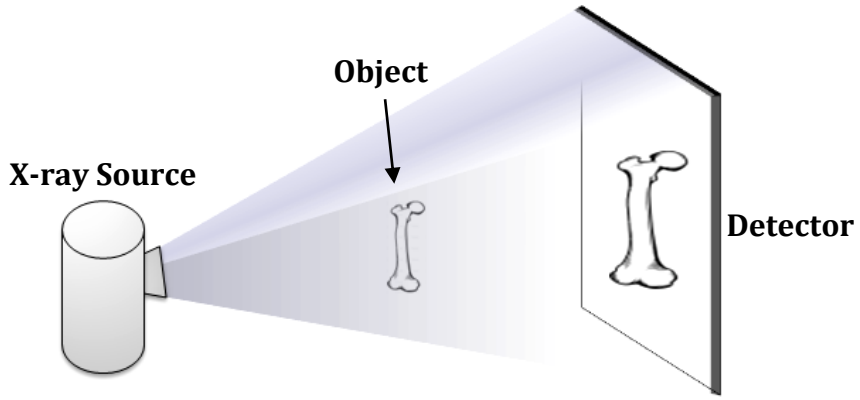

Figure 3: Side view of the cone-beam x-ray used in the standard flat-panel detector.

1.2.2 Calibration box

In conventional RSA imaging suites, a calibration box is a vital aspect of the design (Selvik 1989). An RSA suite contains two X-ray tubes and detectors oriented in space to allow

for stereo radiographs of an anatomical area of interest. The calibration box is situated within the imaging area, (Figure 4). The calibration box contains two sets of non-collinear markers. Control marker cluster is used to determine the foci of X-ray beams. Fiducial marker cluster is used to define the global coordinate system in the RSA environment. The lower left fiducial marker of the calibration box in the local RSA suite defines the origin of the RSA coordinate system. The inter-marker distances for both control and fiducial clusters are known allowing the solving of geometrical transformations resulting in the radiographic presentation of the calibration markers. These transformations are applied to implanted markers and prostheses allowing their reconstruction in 3D space.

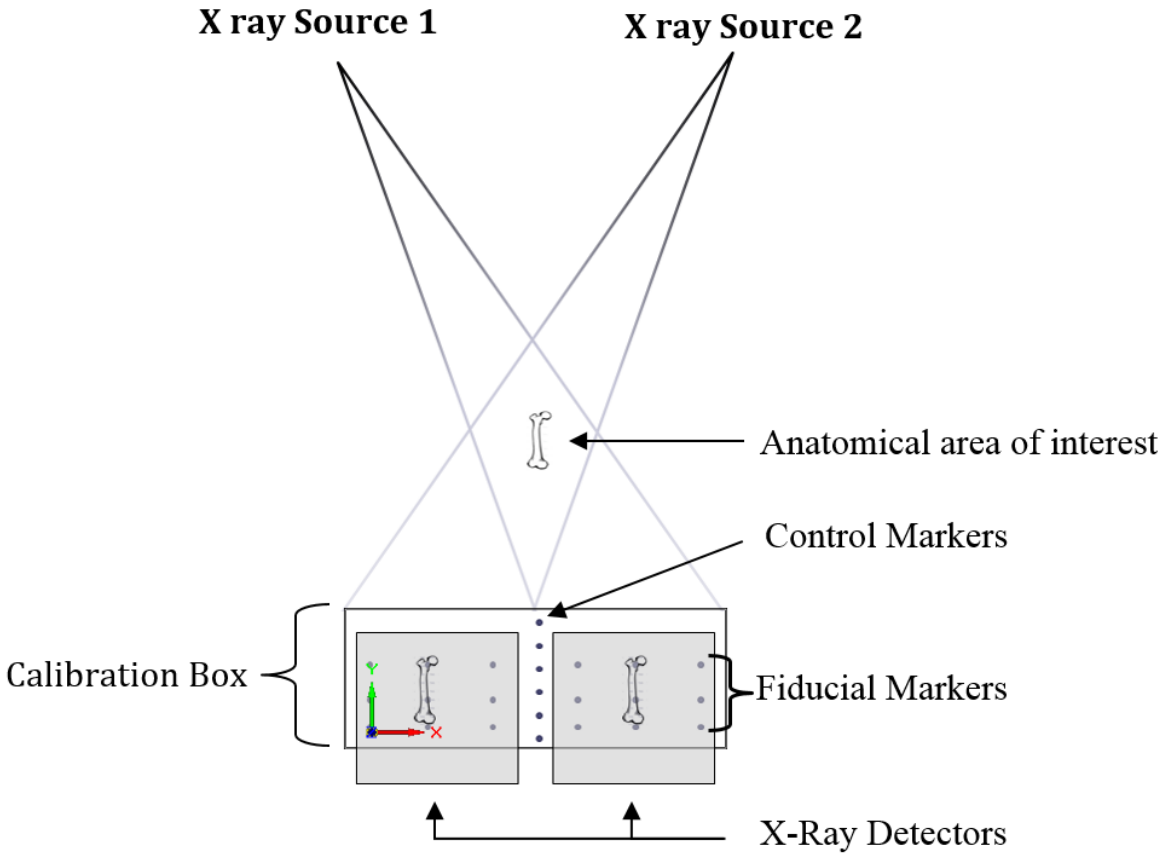

Figure 4: Bottom up perspective of conventional uniplanar RSA set up. Not to scale.

1.2.3 System designs

Prevalent RSA suites can be divided into uniplanar and biplanar set ups. The uniplanar design has two flat panel detectors mounted coplanarly. Usually, the X-ray tubes are oriented so the beams intersect less than 90°. Bi-planar systems have orthogonal X-ray tube and detector

configurations. One limitation of the conventional RSA technique is the requirement of a dedicated RSA suite with a calibration box.

1.2.4 Markers

RSA is typically performed after the implantation of radio-opaque beads into the osseous structure of interest. The radio-opaque markers are elemental tantalum (Atomic Number 73) and usually in sizes of 1.0, 0.8, or 0.6 mm (Bottner et al. 2005). At least 3 beads, or markers, in a non-colinear fashion are required to facilitate representation of the rigid body in Euclidian space and detection of movement (Valstar et al. 2005). Implant modification was previously explored with modifying implants with markers analogous to the tantalum beads (Kaptein et al. 2003). Contemporarily, markerless RSA technique is increasingly being employed in research centres (Li et al. 2014; Seehaus et al. 2012). The markerless technique is possible using Computer-aided Design (CAD) geometrical model fitting to radiographic projections for pose estimation allowing migration tracking, providing acceptable accuracy and precision (Lorenzen et al. 2013). Several parameters, part of a standardized output, quantify bead cluster characteristics. The Condition Number quantifies marker cluster scatter; the Mean Error of Rigid Body Fitting indicates bead cluster stability while the crossing line distance of each marker indicates degree of correct marker registration.

1.2.5 Condition Number

The condition number (CN) expresses the degree of non-linearity and spread of marker cluster. Increasing distance from the centroid and an isotropic configuration minimizes the condition number. An upper limit of 150 for the condition number has been recommended (ISO 16087:2013) alongside the excellent reliability of marker clusters with CN below 100 (Valstar et al. 2005). A condition number of less than 40 leads to a 3-fold increase in rotational accuracy of RSA compared to a condition number above 143 (Bottner et al. 2005). The equation of the Condition Number is described by d, the distance of a marker from the line of decreased distances (LDD), and n, the number of markers in a cluster. LDD is a line propagating through the marker cluster which minimizes the distances between the line and all markers.

Equation 1 - Condition Number

$$CN = \frac{1}{\sqrt{d_1^2 + d_2^2 + \cdots + d_n^2}}$$

The equation of the Condition Number (CN); where d is the distance from the line of decreased distances (LDD), and n is the number of markers in a cluster.

1.2.6 Mean Error of Rigid Body Fitting

The RSA technique stipulates no intra-cluster independent marker movement. As this stipulation may not be met, the Mean Error of Rigid Body Fitting (MERBF) characterizes intra-bead cluster migration as an indication of marker cluster stability in bone, with an acceptable upper limit of 0.35 mm (ISO 16087:2013). The mean error of rigid body fitting is mean difference in the relative 3D locations of the marker cluster at time points 1 and 2; the mathematical expression of which is provided in Equation 2.

Equation 2 - Mean Error of Rigid Body Fitting

$$\text{MERBF} = \sqrt{\frac{1}{n}\sum_{i=1}^{n} \varepsilon_i^2}$$

Where ε is the relative distance between each marker and itself at time points 1 and 2, respectively.

1.2.7 Crossing Line Distance

Crossing Line Distance (CLD) is the distance of the shortest perpendicular line connecting two marker projections, (Figure 5). Back projections from marker shadows do not intersect due to system noise and CLD is indicative of the degree of this discrepancy. Higher crossing lines distances indicate larger errors, and accepted upper limit of CLD is 0.1 mm in Model-Based RSA software (RSAcore, Leiden, The Netherlands). The location of a matched marker is approximated to be at the midpoint of the crossing line.

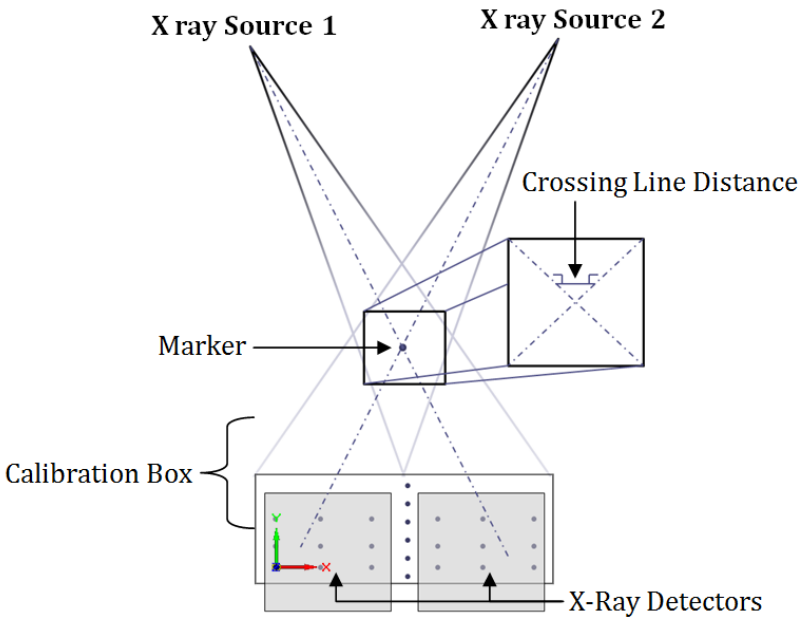

Figure 5: A visual representation of the crossing line distance.

1.2.8 Subpixel Localization

The centre of the circular bead projection is defined to be the spatial location of the marker centroid. Accurate marker centroid detection with subpixel accuracy has previously been attempted using modified circular Hough Transform based on the work of (Duda & Hart 1972). Coarse localization in this technique is based on contour detection and subpixel localization is based on paraboloid curve fitting to signal intensity under marker projections. Nevertheless, this technique is susceptible to contrasting edges and non-uniform background intensity. Complete background image intensity removal is unachievable in heterogeneous images leading to proximal structures immoderately influencing marker centroid detection (Vrooman et al. 1998).

A unique approach devoid of contour detection algorithms employs template matching. Sigmoidal curve simulation used as a template is matched to detected marker projections. An array of subpixel-shifted simulated signal is cross correlated with the normalized signal to determine subpixel location (Briechle & Hanebeck 2001). This technique is more robust against edges and artefacts in close proximity and has been recommended in C-arm applications. In C-arm applications, marker projection pixel width variation exists within a narrow range due to higher confidence in source and detector spatial locations in comparison to the conventional RSA technique (Borlin 2000).

Equation 3 – Normalized Cross Correlation $(f \cdot g) = \frac{\sum_{x,y}[f(x,y) - \bar{f}_{u,v}][t(x-u,y-v) - \bar{t}]}{\left\{\sum_{x,y}[f(x,y) - \bar{f}_{u,v}]^2 \sum_{x,y}[t(x-u,y-v) - \bar{t}]^2\right\}^{0.5}}$

Where $t_{(x,y)}$ is the template, in this case the simulated signal, $\bar{t}$ is the mean intensity of the template bead projection, and $\bar{f}_{u,v}$ is the mean of $f_{(x,y)}$ in the region under the bead projection.

1.3 Precision and Accuracy of RSA

A displacement of 5 mm on conventional Total Hip Arthroplasty (THA) radiographs is required to confirm movement (Sutherland et al. 1982). Translational and rotational accuracy of RSA has been reported to exist between 0.05mm and 0.5 mm and between 0.15° and 1.15°, respectively (Valstar et al. 2002). The high accuracy of RSA in micromotion detection accounts for its increasing implementation in research centres. Accuracy and precision of RSA in both uniplanar and biplanar RSA system designs has been determined in various anatomical models.

1.3.1 Definitions

ISO publishes definitions and guidelines for characterizing accuracy and precision of a system. Accuracy according to ISO is defined as the degree of similarity between the measured and the true or reference value. RSA accuracy has previously been quantified with 95% Prediction Intervals (Laende et al. 2009; Onsten et al. 2001). Equation 4 provides the equation for the Prediction Intervals.

Equation 4 - Prediction Interval $PI = y \pm f\sqrt{s^2 + xSx^T}$

Where s^2 is the mean squared error, t is depends on the confidence interval, f depends on the confidence interval, S is the covariance matrix of the coefficient estimates, x is a row vector of the design matrix.

Precision is defined as the degree of similarity between two or more independent measurements (Ranstam & Ryd 2000). ISO 16087:2013 recommends precision be based on the 95% Confidence Intervals, (Equation 5).

Equation 5 - Confidence Interval

$$CI = \overline{X} \pm t\frac{s}{\sqrt{n}}$$

Where s is the Standard Deviation defined as: $s = \sqrt{\frac{\sum(x - \bar{x})^2}{n - 1}}$

In this expression, x is the observed value, $\bar{x}$ is sample mean, t is the t-statistic adjusted for degrees of freedom, and n is number of data points in the sample.

1.3.2 Phantom Hip Studies

Bragdon and colleagues used THA phantom models to determine the accuracy and precision of their RSA system (Bragdon et al. 2002). Employing a uniplanar design with X-ray tubes situated 40° apart, the researchers exposed radiographs after moving the stem 50, 100, 150 and 200 μm separately in the posterior and superior directions; simulating femoral stem penetration due to hip wear. Accuracy was obtained after performing Analysis of Variance or ANOVA, and precision was obtained from the Standard Error of the differences between applied and observed movements. In their experiment, accuracy was 0.033 mm for the coronal plane, 0.022 mm for the sagittal plane, 0.086 mm for the transverse plane and the resultant 3D accuracy vector was 0.055 mm. The precision was calculated by obtaining five radio-pairs of the model after repositioning with zero-displacement. The precision presented was 0.0084 mm along the x-axis, 0.0055 mm along the y-axis, 0.016 mm along the z, and the resultant 3D precision vector was 0.0135 mm.

In another study, the precision was based on the Standard Deviation of the errors and the accuracy was based on the Root Mean Square of errors (Ioppolo et al. 2007). It is wise to be cognizant of potential incongruity in the calculations and methodology of papers presenting identical data parameters. The researchers found accuracy and precision for translations and rotations along the three Euclidian axes. Displacements were administered to the femoral stem in each anatomical plane while rotations were administered to knee phantom about each anatomical axis. The hip phantom was imaged in a zero-displacement double exam protocol five times before being translated 50, 100, 150, 200 μm and imaged after each. The knee rotations ranged from 0 to 150° simulating flexion-extension and 0 to 9° simulating internal-external rotation. The precision of translations in the transverse plane was 0.058 mm, in the frontal plane was 0.039 mm, and in the sagittal plane was 0.522 mm. Rotational precision about the transverse axis 0.9°,

about the longitudinal axis was 0.9°, and about the sagittal axis was 0.5°. The accuracy of displacement in the transverse plane was 0.065 mm, 0.049 mm in the frontal plane and 0.619 mm in the sagittal plane. Rotational accuracy was presented again as 0.9º about the transverse axis, 0.9º about the longitudinal axis and 0.5º about the frontal axis.

The effects on the precision of a RSA system in two different rigid body movement scenarios, inducible displacement and patient movement, have been explored (Seehaus et al. 2009). In one scenario researchers administered movement to the implant while the surrounding bone was static, analogous to inducible displacement. In the other, movement was applied to both rigid bodies, analogous to patient positioning discrepancies between exposures. In addition to a reference image, single radio-pairs were captured after displacing the tibial and femoral components of Total Knee Arthroplasty (TKA) and the femoral stem component of Total Hip Arthroplasty (THA) in non-anthropomorphic phantoms. The components were translated 1 mm and rotated 1.31 degrees along the x and y-axes, and 1.19 degrees in the z-axis. This sequence was repeated 10 times resulting in the stem component translation of 10 mm in each plane. Precision was defined on the 95% confidence interval. The precision for translations was 0.107 mm for in-plane movement and 0.217 mm for out-of-plane movement. For rotations the precision range was 0.162° for in-plane and 1.316° for out-of-plane rotation. The researchers found no significant differences between either of the movement regimens. This study suggests RSA systems are equally precise in detecting movement and rotation in inducible displacement as patient movement scenarios.

1.3.3 Hip Arthroplasty Studies

RSA has notably been used in the Hip Resurfacing Arthroplasty (HRA) model to characterize implant stability, migration and bone-implant micromotion in response to inducible displacement (Green et al. 1983; Kärrholm et al. 1994; Pineau, et al., 2010). A recent study aimed to demonstrate the in-vivo precision of RSA in detecting translation and rotation in a hip resurfacing model (Lorenzen et al. 2013). The researchers compared marker-based and Computer-Aided Design (CAD) RSA techniques. Eight HRA patients underwent double exams. The Standard Deviation of the discrepancies between double exams constituted the precision. Translational precision in all planes for marker based RSA was 0.2 mm while for CAD RSA was 0.5 mm. Rotational precision in all planes was 1° for both RSA techniques.

Marker based RSA technique was previously compared to Model-Based RSA (MB-RSA) in detecting total hip prosthesis micromotion (Li et al. 2014). Fifty Total Hip Arthorplasty (THA) patients underwent double radio-pair examinations. Generally, MB-RSA was inferior in detecting femoral stem rotation. There was no other significant difference between translational and rotational precision along and about all three cardinal axes. Precision for subsidence ranged from ±0.141 mm for marker based to ±0.136 mm for MB-RSA. Detecting retroversion was nearly half as precise for MB-RSA as detecting rotation about the remaining two axes.

1.4 Orthopaedic Applications of RSA

RSA has previously been used to study micromotion in various anatomical regions including spinal fusion cases (Selby et al. 2012), implant stability in shoulders (Nuttall et al. 2012), hips (Edmondson, et al. 2014), and knees (Barbadoro et al. 2014). Notably during the early 1990s, Karrholm and others (1994) used RSA to link implant stability to future clinical loosening of hip implants. Thereafter, another group linked knee implant migration to future clinical complications (Ryd et al., 1995). RSA has also been proven useful in detecting implant integrity for hip prosthesis by quantifying the deterioration of the polyethylene liner in total hip prostheses (Thomas et al. 2011). Recently, the value of using RSA to characterize motion in soft tissue has been described (Solomon & Callary, 2011) and modifications allowing this application have been presented (Ashmore et al. 2012).

1.4.1 Total Hip Arthroplasty

Long term migration

In 1986, Mjöberg and colleagues were one of the first groups to characterize movement of hip prosthesis in THA patients (Mjöberg et al. 1984). In this study, implant instability was linked to long term migration. Another group is credited with quantifying long term migration of hip prostheses finding 0.33mm of micromotion and 0.85 mm of maximum total point motion (MTPM) within 6 months post operatively, a strong predictor for future prosthesis revision (Karrholm et al. 1994). It is theorized that insufficient coupling at bone-implant interface manifests in future clinical loosening (Mjöberg 1997; Karrholm et al. 1994).

Inducible displacement

Inducible displacement (ID) is the instantaneous displacement of prosthesis in response to load variation. ID has been explored in THA subjects (Glyn-Jones et al. 2006). These researchers sought to determine the level of micromotion that could be induced by load modulation. RSA was performed in 21 hips as THA subjects switched from double leg to single leg stance. Images were taken as single radio-pairs at 6 and 12 months. ID was determined at both these time points to be similar and upon loading (switching to single leg stance) the head of the stem, on average, displaced posteriorly 0.10 ±0.16 mm and inferiorly 0.08 ± 0.12 mm. Another study demonstrated a link between clinical symptoms due to implant-loosening using inducible displacement (Green et al. 1983). The researchers proposed ID below 0.4 mm does not culminate into clinical complications. Patients with asymptomatic loosening demonstrated ID between 0.3 mm and 1.9 mm. Patients with clinical symptoms related to implant loosening demonstrated ID between 0.4 mm to 4.5 mm. These studies indicate the combined value of RSA and Inducible Displacement to determine prosthesis integrity.

Patient Positioning

The effect of patient positioning on the precision of model-based RSA has been explored and consensus is absent. A recent study looked at the accuracy of object to X-ray tube orientation in a uniplanar designed RSA suite (Gascoyne et al. 2014). This study showed maximum precision when a total knee arthroplasty phantom was imaged along the frontal and transverse axes. The translational precision values ranged below 0.036 mm and total rotational precision values ranged below 0.089° in all three planes.

Another group compared the accuracy and precision of varying patient positioning in three biplane imaging modalities. The researchers used fluoroscopic RSA and optical tracking systems in comparison with a conventional RSA system as the gold standard. Phantoms were positioned parallel to one tube, at 45° to both tubes, and then parallel to the other. In all imaging modalities the accuracy and precision was maximized when the phantom was positioned 45° to each detector (Kedgley et al. 2009).

These studies indicate optimal phantom and patient positioning may vary depending on the RSA set up. For uniplanar, anterioposterior and mediolateral perspective while for biplanar, 45° offset to each X-ray tubes may be ideal.

Supine vs. Standing Radiographs

Investigators have previously sought differences in the radiograph presentation of patient imaged in supine and standing orientations (Bragdon et al. 2006). The researchers analyzed 117 THA patients with radiographs in both standing and supine positions. Femoral head penetration did not vary with modulating patient orientation at the 6 month, 1-, 2- and 5-year time points, postoperatively. This study indicates that there is minimal joint laxity in THA patients 6 months postoperatively. Study findings support the direct comparison of standing and supine radiographs.

1.4.2 Paediatric Applications

Previously, the utility of RSA in studying physeal growth following epiphysiodesis has been highlighted (Kärrholm et al. 1984; Hägglund et al. 1986). Recently, researchers using RSA sought to link micromotion after percutaneous epiphysiodesis to post-surgical phyeal arrest (Gunderson et al. 2013). Physiodesis was performed in children and post-surgical physeal fusion was quantified with RS analysis 6 to 12 weeks, postoperatively. On average, 0.22mm to 0.52mm of post-surgical micromotion existed preceding physeal fusion and fusion was achieved in all children within 6 to 12 weeks, postoperatively. Another study exploring the use of RSA to determine post-physiodesis micromotion found mean growth of 0.26mm preceding physeal arrest (Horn et al. 2013). Rotational micromotion has not been quantified with RSA, however 1.12° has been shown to exist following growth plate ablation in the knee model (Khoury et al. 2007). Additionally, RSA has been applied in hemifacial microsomia cases to study mandible widening and micromotion at the bone-implant interface (Sarnäs et al. 2012). There are no known applications of RSA specific to paediatric hip disorders.

Researchers have demonstrated a link between frequent X-ray radiation and increased incidence of cancer later on during one's life. Paediatric patients requiring serial X-ray exams are at an especially increased risk of developing cancer later on life due to exposure at an early age. Nearly 5,500 women with scoliosis or other spine disorder requiring frequent X-ray radiographs

between 1912 and 1965 were included in a study linking radiation dose to incidence of cancer. On average, one women cumulatively received 109, 41, 74, and 10 mGy to the breast, lung, thyroid and bone marrow, respectively, over her lifetime. This cohort exhibited an 8% increase in death due to cancer, while breast cancer deaths was significantly increased in this cohort compared to baseline. They concluded increased radiation exposure and cumulative radiation are both linked to increased risk of cancer (Ronckers et al. 2010).

There has been widespread application of RSA in adult populations assessing a variety of anatomical regions. Application of RSA to the paediatric population has been limited possibly due to the radiation dose associated with serial RSA exams. In the pursuit of As Low As Reasonably Achievable (ALARA) principle, there is a perpetual need to decrease the effective radiation dose for RSA exams. Reduction in radiation dose is desirable and beneficial to adults, but particularly more so to the paediatric population due to increased lifespan post radiation exposure. An alternative to standard cone-beam X-ray imager is the EOS imager, a biplanar slot scanner with 3D capabilities (EOS Imaging, Paris, France). This imager provides similar image quality to standard flat-panel detector radiography with a substantial decrease in radiation dose (Deschênes et al. 2010). Paediatric patients stand to benefit from the reduced radiation dose of the EOS imager for their RSA exams.

1.5 EOS imager

The EOS imager (EOS Imaging, Paris, France) is a slot scanner utilizing biplanar oriented X-ray sources and detectors to construct frontal and sagittal radiographs (Figure 6). The imager utilizes tubes producing 'fan-beam' X-rays instead of 'cone beam' of conventional X-ray systems. These tubes are translated vertically during a scan allowing the capture of 1:1 magnification full-body weight bearing radiographs (Deschênes et al. 2010). It is shown to administer significantly reduced effective radiation dose in comparison to computed tomography (CT) and standard X-ray (Delin et al. 2014). The imager is based on a novel multiwire proportion chamber for particle detectors for which G. Charpak was awarded the 1992 Nobel Prize in Physics.

a) 

b) 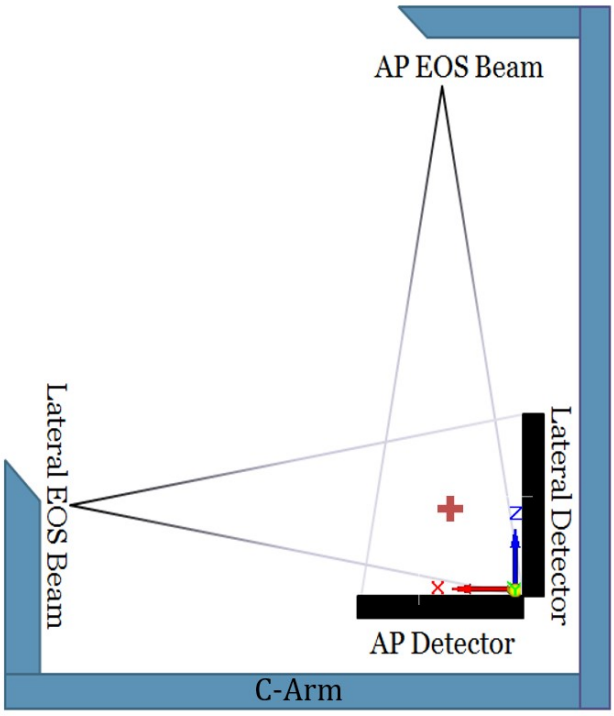

Figure 6: a) The EOS Imaging System **b)** Deconstructed view identifying the C-arm and the EOS Source and Detectors. (EOS Imaging, Paris, France). Red cross indicates location of isocenter.

The imager can scan 175 cm, or any part thereof depending on the area of interest. Full body scans require approximately 20 seconds dependent on patient height. Smaller regions like the hip and knee require significantly less time (Deschênes et al., 2010).

Beam Configuration

The EOS utilizes fan-beam X-rays that exhibit a degree of curvature at the leading edge of the beam. As the beam propagates within the imaging column towards the detectors, the width of the beam expands at increasing distances from the source. This results in X-rays in the centre of the field of view reaching the detector slightly before x-rays reach the extremities of the detector; as the latter have larger distances to travel. This also means the x-rays in the centre of the field of view are incident on the detector at 90° while those at detector extremities are incident at decreasing angles. The decreasing angle distorts the shadow of a spherical object from being circular at the center of the detector to ellipsoid with increasing eccentricity farther away from the center. As illustrated in Figure 7, the shadow of an object at location C is more

distorted compared to the shadow of the same object at location B. Radiographic post-processing, part of the EOS modality, significantly rectifies distortions in the final radiograph.

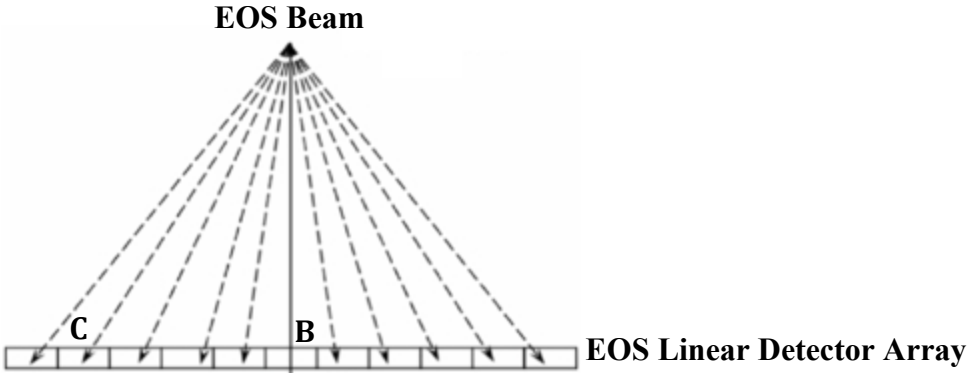

Figure 7: Top down illustration of the fan-beam x-rays used in the EOS imager. B is shadow on the detector of an object centered in the field of view. C is the projection of an object off-centre.

System resolution

The EOS imager has X-ray tubes and detectors mounted on the same C-arm which translate vertically during a scan, (Figure 6B). Being mounted on a C-arm means there is minimal discrepancies in the movement pattern of the sources and detectors. This results in the accurate spatial determination of each source and detector at any point during a scan. The patient is situated approximately 1.0 m from the two sources while the sources and detectors are 1.3 m apart. The system produces two orthogonal X-ray images captured in both the frontal and sagittal planes. The height of each detector is 0.5 mm and the detector array contains 1764 sensors with an isotropic resolution of 254 μm. As the scan progresses, both detector arrays, undergoes image capture every vertical translation of 0.25 mm; these slices are concatenated forming the complete image (Deschênes et al. 2010).

The distance from the AP source to the isocenter is 987 mm, while the distance from the lateral source to the isocenter is 918mm. Effective resolution, due to asymmetric distances from source to isocenter, results in a frontal perspective resolution of 193 x 185 μm and 179 x 185 μm in the lateral perspective. Post-processing artificially increases frontal perspective image resolution to coincide with the resolution of the lateral perspective. This artificial increase of resolution by backsolving radiographic projections from a distance of 987mm to 918mm from the isocenter does not add actual signal to the image (Deschênes et al. 2010).

3D reconstruction

The production of two orthogonal radiographs allows the reconstruction of osseous structures in 3D space. The sterEOS system incorporates the 3D position of bony landmarks and produces a relatively accurate 3D reconstruction of osteoarticular structures in the body (Delin et al. 2014). These reconstructions are comparable to Computerized Tomography (CT) scans with the added benefit of substantial reduction in radiation dose (Folinais et al. 2013).

Quantifying dose reduction

A recent study aimed to quantify the dose reduction offered by the EOS in relation to computed radiography (CR) (Deschênes et al. 2010). The researchers used 13 dosimeters dispersed throughout an anthropomorphic phantom to determine radiation dose. Regions of interest including the proximal point on the lateral chest received 0.27 mGy with the EOS while with the CR received 2.38 mGy. Proximal anterosuperior iliac spine received 0.16 mGy with the EOS and 1.47 mGy with the CR system. The EOS exposed the proximal iliac crest to 0.30 mGy of radiation and the CR exposed it to 2.47 mGy. Similarly, the distal iliac crest received 0.11 mGy and 0.73 mGy of radiation with the EOS and CR system, respectively. The dose reduction with the EOS ranges from 2.9x in the cervical spine to 9.2x at the pelvis as shown in Table 1.

Table 1: Radiation Dose comparison between an EOS and Computed Radiography system Adapted from (Deschênes et al., 2010).

Anatomic Entrance Point	Slot scanner (EOS) Dose (mGy)	Flat Panel Detector (Fuji) Dose (mGy)	Ratio (CR/EOS)
Nape of the Neck	0.20	0.59	2.9
Center of the back	0.18	1.04	5.9
Proximal lateral point	0.27	2.38	8.8
Outer side of the proximal breast	0.11	0.83	7.6
Proximal anterosuperior iliac spine	0.16	1.47	9.2
Proximal iliac crest	0.30	2.47	8.2
Distal iliac crest	0.11	0.73	6.5

Accuracy and Precision in EOS system

Researchers have recently characterized the accuracy and precision offered by the EOS system in relation to conventional radiography. Image acquisition in AP and lateral directions from standard cone beam X-ray and EOS imager were obtained in sitting and standing stances for five unilateral THA subjects. Images were observed by two observers three times. Angular clinical measures were extracted from each radiograph. 95% confidence interval for inter and intraobserver reproducibility of pelvic parameters ranged from ±4.26° to ±7.83° for conventional and from ±2.97° to ±6.46° for the EOS radiographs. In acetabular parameters, the 95% CI values ranged between 4.79° to 10.22° and ±3.83° to±6.27° for conventional and EOS radiographs, respectively. Nearly all parameters obtained from EOS radiographs displayed statistically reduced offsets and variance compared to the conventional radiography pointing to the increased quality of EOS radiographs for clinical measurements (Lazennec et al. 2011).

Using CT as the gold standard, a group has correlated the accuracy and precision of the EOS imager (Guenoun et al. 2014). Twenty-eight femoral stems were surgically implanted into phantom femurs and imaged with CT and the EOS imager. The average femoral offset, the horizontal distance between the femoral shaft and the center of the femoral head, with CT was determined to be 52.11 mm with Standard Deviation (SD) of 7.75 mm. The EOS radiographs provided an average femoral offset of 52.78 mm with SD of 7.75 mm. Femoral anteversion was determined with CT to be 3.82° with SD 12.49 ° and with EOS to be 4.06° with SD 12.50°. Statistically, only the femoral offset differed between the imaging modalities.

These studies indicate improved accuracy and precision of EOS radiography over conventional radiography while showing comparatively similar to the accuracy offered by CT. However, no previous studies have characterized the accuracy and precision of 3D triangulation of implanted 1-mm tantalum markers and intercluster translation and rotation using the EOS modality. It is hypothesized the comparable image quality of the EOS to conventional radiography will translate to comparable accuracy and precision of RSA in the EOS modality. There likely is much benefit to be derived from the application of RSA in the EOS imager by the paediatric and adult population due to its reduced radiation dose and image quality. The C-arm configuration allows the precise spatial determination of the sources and detectors at all points during the scan potentially allowing RS analysis without a calibration object. The application of

RSA in the EOS imager without the necessity of a calibration object would make it more clinically accessible for a wide range of research and clinical centers.

Chapter 2: Thesis objectives

Thesis Purpose: To implement the RSA technique in the EOS imaging modality and indicate the accuracy and precision of the EOS RSA technique. Specific objectives include:

1. Through an in-vitro study, compare the translational and rotational accuracy and precision of RSA in the EOS imaging and digital radiography modalities for a SCFE model.

2. Through an in-vivo pilot study, demonstrate the EOS RSA technique in subjects and indicate in-vivo precision of this novel implementation.

Objective #1

Motivation

There exists a need to analyze micromotion in the post-surgical SCFE femoral head as a clinical indicator of surgical success. It is hypothesized this micromotion detection is attainable solely through the level of sensitivity offered by RSA. With the reduced radiation dose offered by the EOS system, particularly warranted for the paediatric population, this thesis aims to employ RSA within the EOS imaging modality to verify a protocol allowing micromotion detection across the SCFE capital physis.

Approach

The accuracy and precision of RSA in a SCFE model will help determine the suitability of RSA from EOS radiographs for the SCFE population. While the diaphysis is aligned vertically to mimic expected patient positioning, the phantom will be imaged after application of translation and rotation to the metaphysis in the three planes. Standard suite radiographic analysis will be performed in MB-RSA 3.41 (RSAcore, Leiden, The Netherlands) and EOS radiographic analysis in custom-built software in MATLAB 2014a (The Mathworks, Inc., Natwick, MA). Statistical analysis of the observed values will determine accuracy and precision.

Hypothesis

It is expected that the vertical translations of the EOS C-arm along with larger pixel size than the standard flat panel detector, will negatively affect the accuracy and precision of the EOS RSA technique in comparison to the flat-panel RSA technique.

Objective #2

Motivation

The application of RSA in the EOS modality is novel and the utility of this novel implementation will be indicated through in-vivo testing. This study will primarily explore the effects of patient positioning, patient motion and soft-tissue artefacts on the in-vivo precision.

The utility of RSA in predicting total joint replacement prosthesis loosening has previously been widely demonstrated. Additionally, no cohort of paediatric patients exists at the local hospital with RSA beads implanted in the femur. Total Knee Arthroplasty (TKA) subjects are readily available and are in a sufficient population in a study at the adult hospital to allow invitation into this study. Therefore, TKA patients will be imaged; to demonstrate the benefit and safety of this novel implementation before its application in the paediatric SCFE population.

Approach

EOS images of TKA subjects will be captured in controlled conditions as per a zero displacement double exam methodology (ISO 16087:2013). The initial step will be to visualize the implanted RSA markers in EOS radiographs of TKA subjects. At least three non-collinear markers are required to quantify motion and the matching of which will facilitate migration analysis.

Assuming adequate bead visibility, migration calculations will be performed. In this pilot study, double exam EOS radiographs in double leg stance will be obtained for three TKA subjects. Each RSA exam will be compared to the subsequent for each subject. As the scan will be obtained in controlled conditions, migration analysis output will indicate the precision of this technique.

Hypothesis

A potential source of error of the RSA technique in the EOS system is the radiograph acquisition time spanning several seconds as opposed to milliseconds in conventional radiography. This is expected to introduce patient motion artefact in radiographs potentially negatively affecting the precision of this technique.

Chapter 3: The Accuracy and Precision of Radiostereometric Analysis in Determining Physeal Motion in Slipped Capital Femoral Epiphysis: A Phantom Model Study

INTRODUCTION

One of several ways of determining prosthesis stability is with a technique called Radiostereometric Analysis (RSA). RSA allows the quantification of relative rigid body motion and has been instrumental in linking post-operative implant stability to implant survivorship (Valstar et al. 2000; Kärrholm et al. 1994; Kendrick et al. 2015; Salemyr et al. 2014; Dunbar et al. 2009). Phantom studies have previously been used to characterize the accuracy of RSA systems with replica models increasingly being employed to better simulate in-vivo settings (Bojan et al. 2015; Stilling et al. 2012; Gascoyne et al. 2014). This allows the determination of model specific shortcomings and steps required to address these issues before the in-vivo implementation of RSA. The primary motivation of this phantom study was to characterize the accuracy and precision of the RSA technique in the EOS imaging modality for the SCFE model. Additionally, the study will indicate proper patient positioning and orientation in the imaging column among other elements of a successful EOS RSA exam.

The EOS imager, based on a novel particle detector, is a low radiation dose biplanar imaging system with 3D capabilities. It employs x-ray sources and detectors on a vertically translating C-arm allowing for standing full-body images of subjects. Pixel size at detector is 254x500µm but effective resolution due to magnification factors in the frontal and lateral perspectives is 185x193µm and 179x185µm, respectively. EOS pixel sizes are larger than in flat panel detectors which are isotropic at 160x160µm. The study was motivated to investigate the effect of differing pixel size and vertical translation of the x-ray sources and detectors on the accuracy of the RSA technique.

The post-operative proximal SCFE femur has substantial dimensional constraints in addition to the presence of bead occluding hardware; fixation screw(s). This results in minimal area in the femur for RSA bead implantation and achieving recommended condition numbers for two bead clusters (ISO 16087:2013).

The purpose of the study was to assess the translational and rotational accuracy and precision of RSA in the EOS imager and the standard uniplanar RSA suite. The primary motive of this study was to explore the effects of larger pixel size and vertical translation of C-arm on the effects of bead localization on radiographs and therefore accuracy and precision of the EOS RSA technique. This study also investigated the dimensional challenges of achieving a recommended marker cluster configuration in the proximal SCFE femur as recommend in (ISO 16087:2013).

METHODS

Translations and rotations were applied to the phantom with three-dimensional micrometers. The SCFE femur model was divided into two rigid bodies; proximal epiphysis and metaphysis. Translations were applied to the metaphysis while the epiphysis was stationary. An 'overshooting' methodology was employed during the applications of all displacements in which the controls on the micrometer were rotated past the target and then rotated in the reverse direction to converge on the target.

Femur Phantom Set Up

A sawbones SCFE femur phantom (Pacific Research Laboratories, Vashon Island, WA) catalog number #1611, was cut across the physis, determined by the circumferential prominence at the neck-epiphysis interface (Figure 8). The femur was implanted with a 7.3mm-diameter 45 mm-long fully threaded cannulated fixation screw (DePuy Synthes, West Chester, PA). The cut and fixation was performed by a paediatric orthopaedic fellow at the local children's hospital. Next, the cannula was further widened by 10 mm. Eleven 1 mm-diameter tantalum beads were implanted into the widened cannulation. Four beads comprised the epiphyseal bead cluster while seven beads were implanted distal to the proximal physis comprising the metaphyseal bead cluster. A computer simulation was performed (Appendix C) that showed an increased likelihood of bead occlusion when epiphyseal beads were implanted inferior to the screw. To mitigate bead occlusion, all epiphyseal beads were implanted superior to the screw. Bead occlusion was not problematic in the metaphyseal bead cluster in the computer simulation, therefore, four beads were implanted inferior and three beads superior to the screw with the aim of increasing cluster scatter.

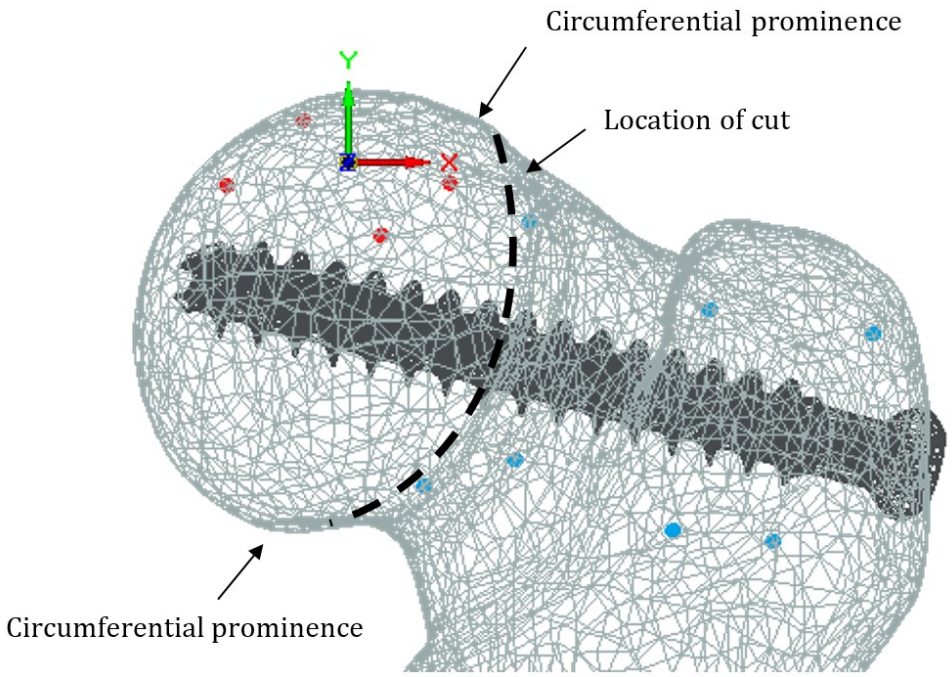

Figure 8: Bead cluster developed from the computer simulation study. Blue and red circles indicate metaphyseal and epiphyseal beads, respectively.

Femur Anatomical Coordinate system

The **longitudinal axis** was defined as the line extending proximal-distal through the intramedullary canal (Moreland et al. 1987). The femur was horizontally cut 10 cm distal to the center of the femoral head. The cut face was attached to the micrometer, with an acrylic base plate, so that the **transverse axis**, extending from the center of the femoral neck through the proximal tip of the greater trochanter was aligned to the x-axis of the micrometer, defined by the direction of the x-axis dial. Similarly, the longitudinal axis of the femur was aligned to the y-axis of the micrometer. The line orthogonal to the longitudinal and the transverse axes defined the **sagittal axis** which was aligned with the z-axis of the micrometer. The epiphysis was then secured to the base plate in the following manner: the epiphysis was positioned so the epiphyseal and metaphyseal faces produced by the physeal cut were parallel. Visually, the phantom construct was positioned in the RSA environment so the right handed anatomical coordinate system aligned with the right handed coordinate system of the RSA environment.

Phantom Translations

According to the right handed anatomical coordinate system of the left-sided SCFE femur phantom used in this study, lateral, superior and anterior displacements correspond, respectively, to positive translations along the x-, y- and z-axes (ISO 16087:2013), (Figure 9). Translations were applied to the metaphysis sequentially with a translational micrometer (M3946M, Parker Daedal, Irwin, PA) along all axes.

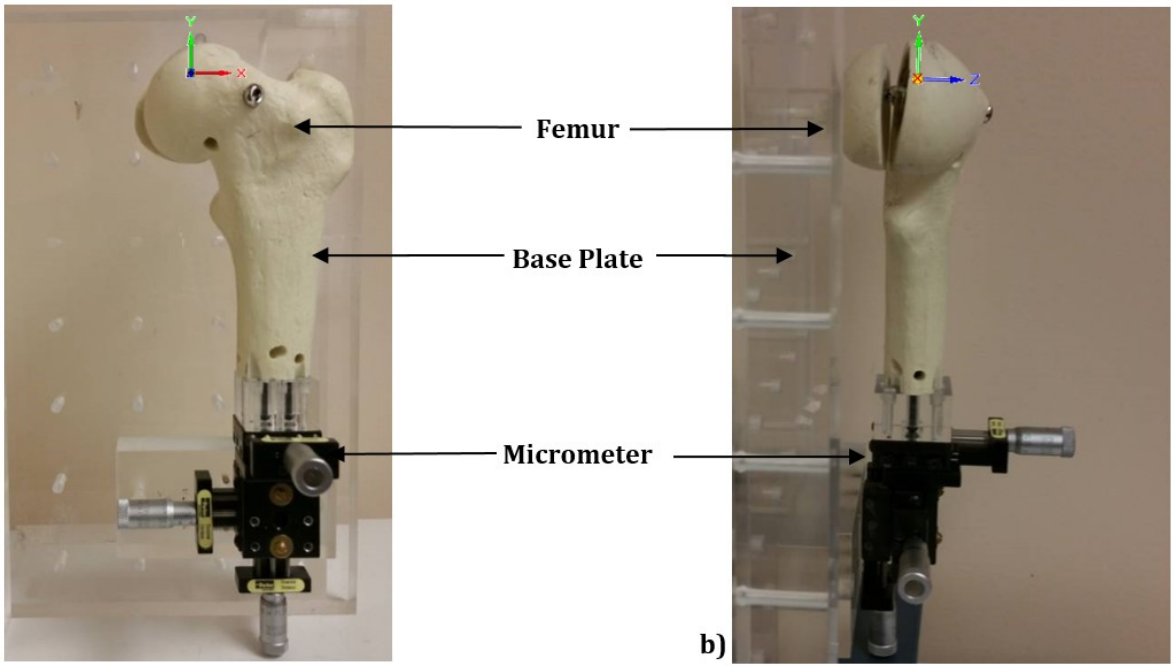

Figure 9: The setup of the translational phantom model study with the anatomical coordinate system provided. A) Anterior view b) Left Sagittal view (Note: Positive x-axis projects into page).

Images were captured after the application of each movement and compared to the reference image. A reference image commenced this study. Thereafter, along the transverse, longitudinal and sagittal axes, displacement values applied to the phantom were guided by limits of clinical significance of 0.22mm (Gunderson et al. 2013). Translational values presented in Table 2 were applied sequentially without zeroing the micrometer. Three radiographs were captured for each applied displacement with repositioning following each image capture.

Table 2: The displacements applied to the metaphysis in relation to the stationary epiphysis in the phantom model study.

Axis of Translation / Translation of Metaphysis	**Displacement (mm)**						
X Axis / Medial	-0.10	-0.25	-0.50	0.75	-1.00	-1.50	-2.00
Y Axis / Superior	0.10	0.25	0.50	0.75	1.00	1.50	2.00
Z Axis / Anterior	0.10	0.25	0.50	0.75	1.00	1.50	2.00

Phantom Rotations

A high precision rotational stage (Newport, Irvine, CA) with an accuracy of 0.017° and a wobble rating of 0.003° was used to apply rotations to the metaphysis.

As in the translational study, the femoral epiphysis was rigidly fixed to the base plate. The metaphysis was attached to the rotational micrometer and positioned to mimic anterior-tilt, external and varus rotations. According to the local coordinate system, anterior tilt, external and varus rotations occur about the + x-, + y- and - z-axes, respectively, ISO 16087:2013. Rotations guided by the limits of clinical significance of 1.12° were applied (Khoury et al. 2007) (Table 3). The phantom set up is presented in Figure 10. This experiment utilized the same image capture protocol as the translational study.

Table 3: The rotations applied to the proximal femoral metaphysis in relation to the epiphysis in the phantom model study.

Axis of Rotation / Rotation applied to the metaphysis	**Rotations in degrees (°)**					
X axis / Anterior Tilt	+0.17	+0.33	+0.50	+1.00	+2.00	+4.00
Y axis / External rotation	-0.17	-0.33	-0.50	-1.00	-2.00	-4.00
Z axis / Varus rotation	+0.17	+0.33	+0.50	+1.00	+2.00	+4.00

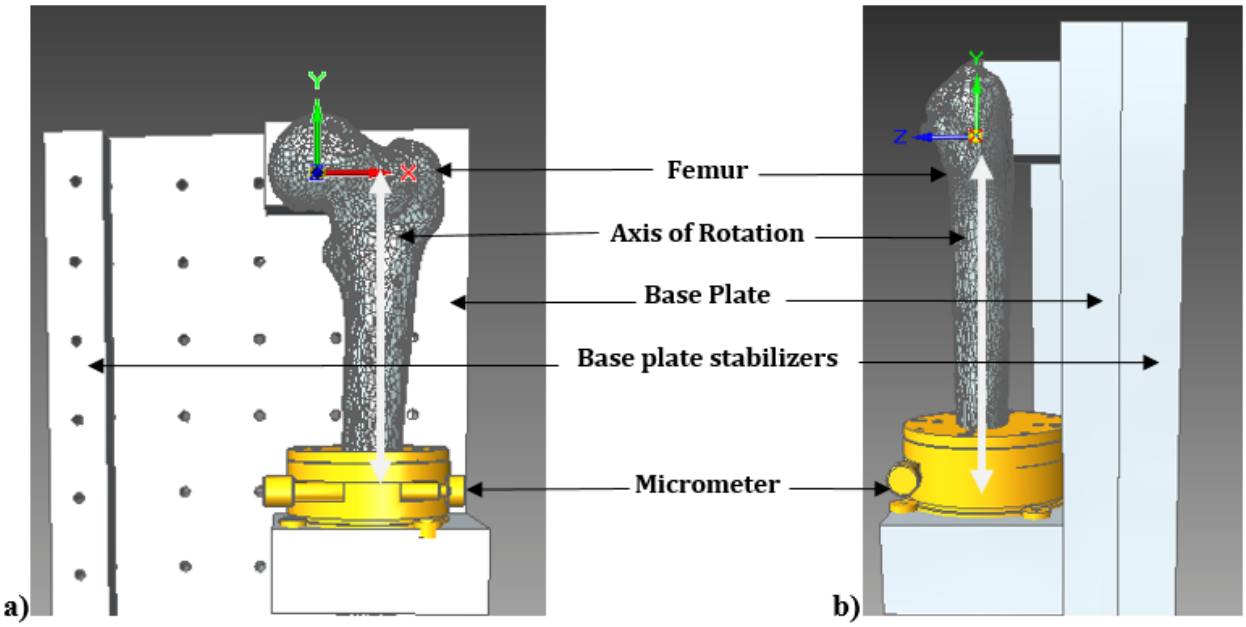

Figure 10: The setup of the rotational phantom model study. A) anterior view b) right sagittal view (Positive X-axis projects out of page). The illustrated set up mimics external rotation of the metaphysis.

Image Capture Protocol

EOS Imager

In the EOS imager, the phantom was positioned so that the sagittal axis of the femur aligned with the Anterio-Posterior (AP) X-ray beam and the transverse axis with the Lateral Beam. The femoral head was positioned at the isocenter; the location where the AP and Lateral beams of the EOS imager intersect Using the laser projections and markings on the base of the EOS imager the phantom was positioned and vertically oriented within the imaging column with visual guidance. The whole construct was imaged at a height of 90 cm above the base of the EOS imager (Figure 11). Four 40x30x5 cm polymethyl methacrylate blocks were included in the front, back, left and right of the phantom construct to emulate front and back soft tissue scattering in both AP and lateral perspectives.

At the EOS workstation, the scan distance was set to 40 cm commencing at a height of 110 cm and terminating 70 cm from the base of the EOS with the phantom located 90 cm above the base. The scan height was adjusted as appropriate in the precision study. In the EOS workstation, scan speed was set to 4.57 cm/sec. Both beams were set to a kiloVoltage (kV) and milliAmperes (mA) of 120 and 20, respectively. The reference planes remained at the isocenter. The isocenter is the line of intersection of the AP and Lateral EOS beams. The patient orientation

module, was rotated to reflect the AP positioning of the femur. The pressing of the 'scan' button concluded the image capture protocol, leading to the production of two EOS radiographs.

a) 

b) 

Figure 11: The location of the phantom within the EOS imager. A) Side view B) top down view within imaging column.

Calibration of the EOS imager

The calibration procedure of the EOS imager described here was developed by LIO (Laboratoire de recherche en imagerie et orthopédie, Montreal, Canada). The calibration of the EOS imager was completed with a calibration object; an empty Nalgene bottle (Thermo Fisher Scientific Inc., Waltham, MA) with 27 radio-opaque tantalum beads randomly melted to the circumference (Figure 12).

Figure 12: Radiographic representation of the calibration object used in the EOS calibration protocol.

The calibration object was imaged four times, with repositioning, at a height of 90 cm above the base so the longitudinal axis of the bottle was vertically aligned and positioned at the EOS isocenter indicated by intersection of the laser projections in the imaging column. In the subsequent four images, the bottle was displaced 10 cm away from and towards the frontal and lateral beam sources. For the final two images, the bottle was half-filled with water and placed at the isocenter in the EOS imager so the longitudinal axis of the bottle was aligned horizontally. In this orientation the bottle was rotated so the longitudinal axis intersected the frontal and lateral beams at 45°. Images were captured following the subsidence of oscillations in the waterline. Table 4 presents the sequence of image capture of this protocol.

Table 4: The sequence of image acquisition for calibration of the EOS imager.

Image pair	Location in EOS	Longitudinal axis of bottle aligned with:	Water present?
1	At isocenter (382,900,313)	Y axis	No
2	At isocenter (382,900,313)	Y axis	No
3	At isocenter (382,900,313)	Y axis	No
4	At isocenter (382,900,313)	Y axis	No
5	10 cm closer to Lateral Source (482,900,313)	Y axis	No
6	10 cm farther from Lateral Source (282,900,313)	Y axis	No
7	10 cm closer to AP Source (382,900,413)	Y axis	No
8	10 cm farther from AP Source (382,900,213)	Y axis	No
9	At isocenter (382,900,313)	225° to X-axis	Yes
10	At isocenter (382,900,313)	315° to X-axis	Yes

Radiographic Analysis

The radiographs were loaded into MATLAB 2014a and analyzed with programming code jointly developed with LIO. Parameters defining the location and orientation of each EOS source and detector are optimized in the calibration protocol, including: the distance of each source to the isocenter, the differences in height of the sources and detectors during a scan (Figure 13A) and the perturbation in the sources' and detectors' orthogonal axes (Figure 13B).

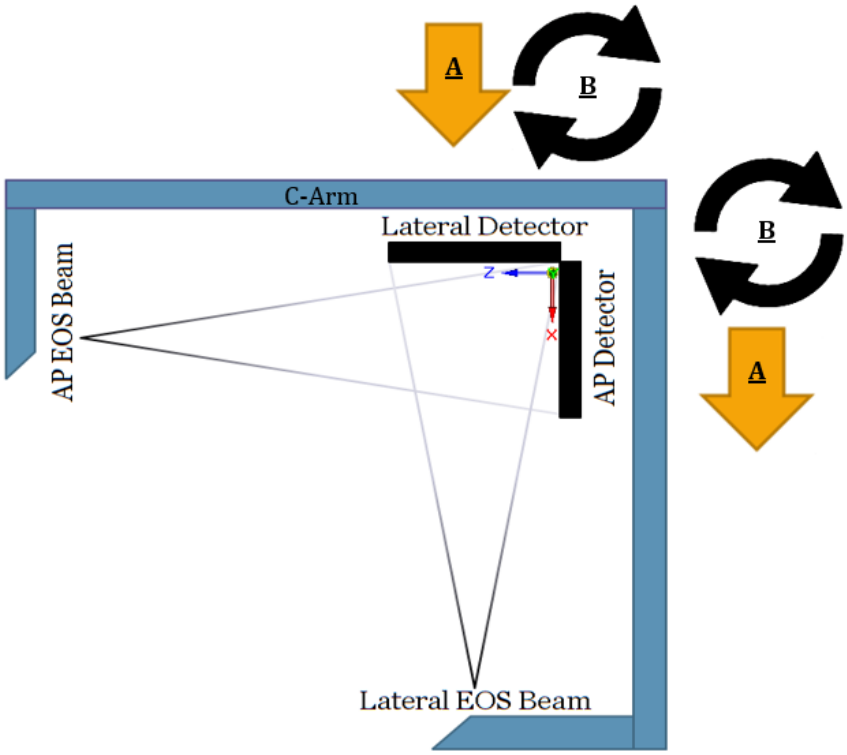

Figure 13: Top down deconstructed view of the EOS imager. The sources of error in an EOS imager scan are **A)** Vertical translation of sources and detectors (into page) **B)** In-plane rotation of detectors.

The calibration procedure employed an iterative method. Using the first four image pairs, (Table 4), an average model of 3D points of the bottle bead cluster was built. This model was back-projected onto the marker projections obtained in subsequent radiographs. The EOS parameters minimizing the differences between the average model and new samples were converged upon in an iterative process. In this calibration procedure, the Root Mean Square Error (RMSE) in 3D positions of beads was minimized to below 35 µm. The waterline was used to determine the x-z plane of the EOS frame and to correct for the vertical drift on the micron scale that occurs in the radiographs. Optimal calibration parameters following the calibration protocol were used in analysis of all EOS images in the phantom model study.

Standard RSA suite

The uniplanar RSA suite was configured to obtain standing RSA exams, to mimic the expected patient stance during a post-operative hip RSA exam. The X-ray tubes were lowered from the ceiling to a height of 90 cm above the floor and the calibration box was situated 30 cm behind the isocenter, the convergence point of the X-ray beams. The detectors were positioned

130 cm away from the X-ray sources. The center of the femoral head of the phantom was positioned at the isocenter. The phantom anatomical planes were visually aligned to the RSA environment coordinate system. Soft tissue equivalents were included in this environment similar to in the EOS imager. The location of the phantom is presented in Figure 14.

At the RSA workstation, beam characteristics were set to 140 kVp (peak kiloVoltage) and 32 mAs (milliAmpere seconds). With this, the simultaneous exposure of both X-ray tubes produced standard RSA suite images.

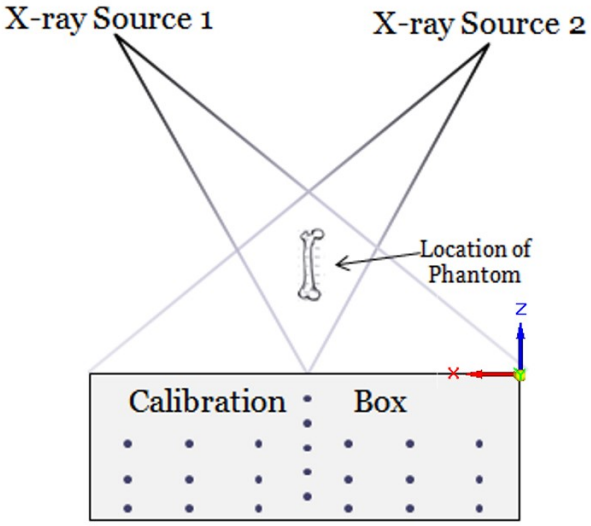

Figure 14: Top down view of the uniplanar RSA suite denoting the location of the phantom. RSA coordinate system provided in bottom right corner. Note: Positive y-axis projects out of page.

Phantom Precision

Table 5 includes the iterations used to assess RSA precision. The additive effects on the precision of the RSA technique of 1) the femur phantom not being centered in the field of view (Exams ii, iv and v in Table 5) and 2) the phantom's anatomical axes misaligned with the axis of the RSA environment were elucidated (Exams iii, iv and vi in Table 5). A note on terminology, aligned pose denotes anatomical and global coordinate system alignment.

Table 5: The nature of RSA exam and the imager it was completed in.

Type of RSA exam	Completed in?	
	Standard Imager	EOS Imager
i) Centered in FOV	Yes	Yes
ii) Phantom displaced by ±10 cm in standard pose	Yes	Yes
iii) ±15° rotation about each axis and centered in FOV	Yes	Yes
iv) ±15° rotation about each axis and ±10 cm displacement	Yes	Yes
v) EOS Detector Extremities	No	Yes
vi) 45° vertical axis rotation	No	Yes

i) Standard phantom pose centered in FOV

The phantom was positioned at the isocenter in the EOS and seven radiograph pairs were captured following repositioning. For each capture, the phantom was positioned at the EOS isocenter defined by the intersection of the AP and lateral beams and indicated by the laser projections in Figure 11b. In the standard RSA suite, the phantom was centered in the FOV in aligned pose. Roman numeral i in Figure 15 and Table 6 presents the location of the phantom during image captures.

ii) Aligned pose with ±10 cm displacements in FOV

The phantom was imaged in the aligned pose with ±10 cm displacements along each cardinal axes. Roman numeral ii in Figure 15 and Table 6 presents the location of the phantom during image captures.

iii) Phantom misaligned by ±15° rotation centered in FOV

The phantom was rotated ±15° about the x-, y- and z-axes at the isocenter. The sequence of image capture, location of phantom and misalignment introduced to the phantom construct in each image capture are presented by Roman numeral i in Figure 15 and Table 6.

iv) Phantom misaligned by ±15° rotation and ±10 cm off-center in FOV

To capture the compounded effects on precision of i) misalignments between the anatomical and RSA coordinate systems and ii) imaging off-center, the phantom construct was

imaged following the ±15° rotation and ±10cm displacement to the whole construct. This investigation started and ended with the phantom imaged centered and in aligned pose. Roman numeral ii indicates location of phantom during image capture in this test in Figure 15.

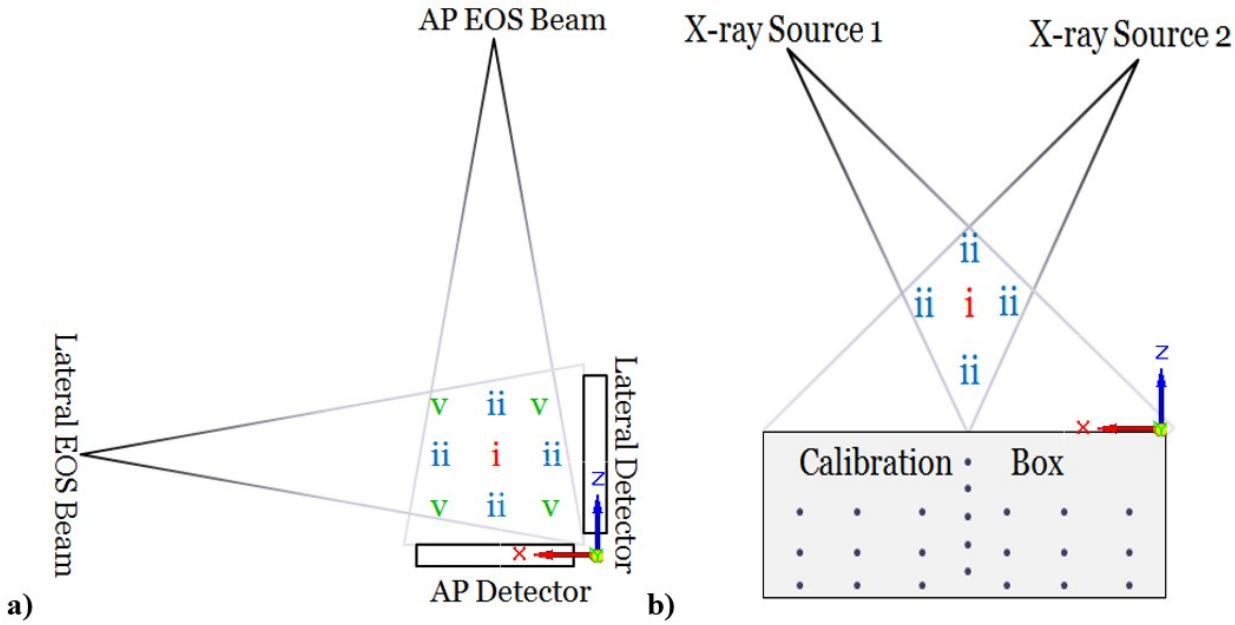

Figure 15: Top down perspective of **a)** EOS imager and **b)** standard RSA suite. The location of the phantom is indicated by the roman numerals corresponding to location of each test in Table 6.

Table 6: Sequence of image capture and analysis during Experiments ii, iii and iv in the precision study.

	Test ii	**Test iii**	**Test iv**
RSA exam 1	Centered in the FOV and no misalignment	Centered in the FOV and no misalignment	Centered in the FOV, No misalignment
RSA exam 2	+10cm X-axis displacement	+15° X-axis rotation	+10cm X-axis displacement and +15° X-axis rotation
RSA exam 3	-10cm X-axis displacement	-15° X-axis rotation	-10cm X-axis displacement and -15° X-axis rotation
RSA exam 4	+10cm Y-axis displacement	+15° Y-axis rotation	+10cm Y-axis displacement and +15° Y-axis rotation
RSA exam 5	-10cm Y-axis displacement	-15° Y-axis rotation	-10cm Y-axis displacement and -15° Y-axis rotation
RSA exam 6	+10cm Z-axis displacement	+15° Z-axis rotation	+10cm Z-axis displacement and +15° Z-axis rotation
RSA exam 7	-10cm Z-axis displacement	-15° Z-axis rotation	-10cm Z-axis displacement and -15° Z-axis rotation
RSA exam 8	Centered in the FOV and no misalignment	Centered in the FOV and no misalignment	Centered in the FOV and no misalignment

v) Phantom imaged at EOS detector extremities

This test was conducted only in the EOS imager, with the phantom imaged at detector extremities in aligned pose. The construct was positioned at four locations, corresponding to left and right edges of both detectors. At these locations, denoted by roman numeral v in Figure15, the phantom was imaged in seven iterations.

vi) 45° vertical axis rotation of phantom

Anecdotal evidence indicates due to substantial periarticular soft tissue mass and the contralateral hip, EOS RSA exams will potentially be conducted with a 45° rotation of the subject's sagittal axis to the AP beam. To emulate this orientation, the phantom was rotated in the vertical column about the vertical axis 45° and positioned at the isocenter. In this orientation, seven radiograph pairs were captured with repositioning.

Radiographic Analysis

Radiographs were analyzed for bead cluster movement with each exam compared to the subsequent and the last RSA exam was compared to the first. For the purposes of analysis, the metaphysis bead cluster was the reference and the epiphysis bead cluster was the migrating rigid body. This was a notable departure from the phantom model set up in which the metaphysis and the epiphysis were migrating and stationary bodies, respectively. The improved accuracy of relative motion detection when the cluster with the higher number of beads is the reference explains this departure.

EOS image analysis

EOS images were analyzed with custom built software in MATLAB 2014a (The MathWorks Inc., Natick, MA). Coarse bead detection was based on user prompted initial estimate while subpixel localization was based on template matching with simulated signal normalized cross correlation. At each detected bead, 144 sub-pixel shifted beads were simulated. The simulated template with the highest correlation to the normalized detected signal was used to determine the subpixel location. Registering marker projections on the stereo images, using the height of the scan and distance from the left edge of the detector in each perspective, the 3 dimensional position of each marker was calculated. Rigid body kinematic analysis followed and

was based on singular value decomposition method explained in detail by Challis (1995) and Valstar et al. (2002). Number of matched markers used in analysis was recorded from the output.

Standard RSA suite analysis

Standard RSA suite images were analyzed in Model-Based RSA 3.41 (RSAcore, Leiden, The Netherlands). Bead detection algorithms were run and the images were analyzed for the locations of all beads in 3D space. Visual inspection followed to ensure proper detection of beads and the bead detection crosshair were modified in size and location in cases of inaccurate bead detection. Next the beads corresponding to the epiphyseal and metaphyseal bead clusters were respectively labeled and visual inspection of crossing line distances and the highlighted marker model followed. Relative marker migration calculations followed. Translations detected along the x-, y- and z-axes and rotations about the x-, y-, z-axes were recorded in addition to the Condition Number for each bead cluster, Maximum Total Point Motion (MTPM) and Mean Error of Rigid Body Fitting.

Statistical Analysis

Statistical analysis was performed with an independent Student's t-test to compare differences in prediction interval widths between imagers (Wilson 2007). Bland-Altman method was used to determine the limits of agreement of both RSA techniques against the micrometer reference value (Bland & Altman 1986; Krouwer 2008; Stilling et al. 2012). Limits of agreement and percentage bias from both techniques were compared to the limits of clinical significance.

Equation 6 - Limits of Agreement

$$LA = mean \pm 1.96*SD$$

Where SD is the standard deviation.

The precision of the RSA technique from both imagers was analyzed firstly with Anderson-Darling test to assess normal distribution and then variances of all precision tests between imagers were compared with an F-Test. The measurement bias for each nature of movement in each technique was calculated as a percentage of the Limits of Clinical Significance (Spurway 2012).

Accuracy

Accuracy was based on the 95% Prediction Intervals (Onsten et al. 2001; Madanat et al. 2005). The applied and observed displacements were loaded in MATLAB 2014a software and the 95% Prediction Intervals were calculated. The Prediction Intervals were averaged for each nature of movement in each plane and divided by two. The accuracy of the RSA technique was presented as half the average width of the intervals for each nature of movement and each imaging modality.

Precision

The precision of the techniques was based on the Standard Deviations (ISO 16087:2013). The Standard Deviation was calculated in Microsoft Excel 2014 software (Microsoft Corporation, Redmond, WA). The output was adjusted for degrees of freedom and presented as the confidence interval around zero (ISO 16087:2013).

RESULTS

Phantom Translations

Medial Displacement Accuracy (x-axis)

Detecting medial displacements in the standard technique was accurate to 0.05 mm, while the EOS technique was accurate to 0.04 mm (Figure 16). A statistical difference was found in medial displacement accuracy of RSA in the EOS and standard imagers ($p<0.01$).

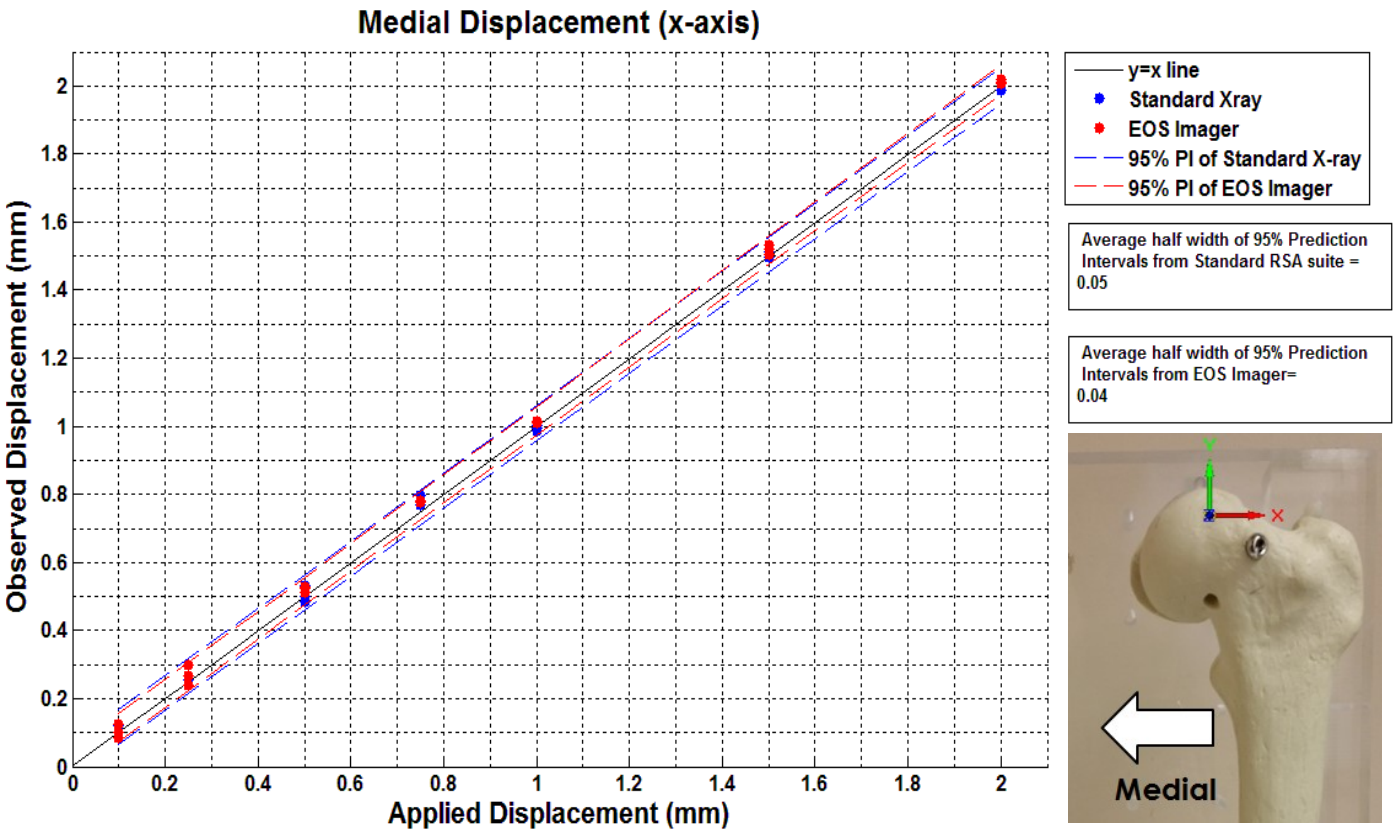

Figure 16: The accuracy of RSA in detecting medial displacements between the epiphyseal and metaphyseal bead cluster in the standard RSA suite and the EOS imager. The average half widths of the 95% Prediction Intervals is presented on the top right. Direction of **metaphyseal movement** is illustrated on the bottom right.

Superior Displacement Accuracy (y-axis)

The standard RSA technique was accurate to 0.03 mm in detecting superior migration, while the EOS technique exhibited lower accuracy at 0.04 mm (Figure 17) ($p<0.01$).

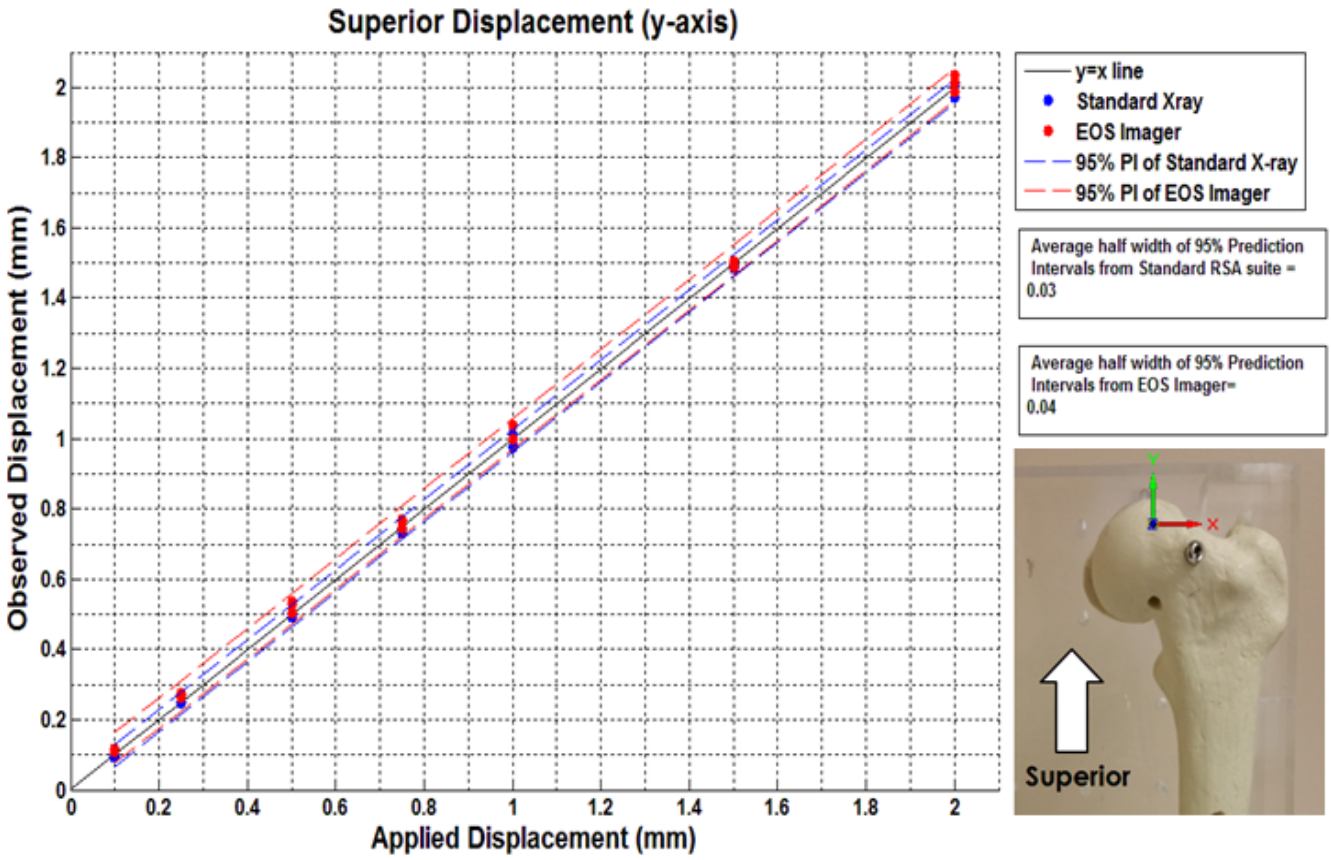

Figure 17: The accuracy of RSA in detecting superior displacements between the epiphyseal and metaphyseal bead cluster in the standard RSA suite and the EOS imager. The average half widths of the 95% Prediction Intervals is presented on the right. Direction of **metaphyseal movement** is illustrated on the bottom right.

Anterior Displacement Accuracy (z-axis)

In anterior displacement detection the accuracy of the standard technique was 0.07 mm, while the EOS RSA technique exhibited higher accuracy at 0.05 mm ($p<0.01$) (Figure 18).

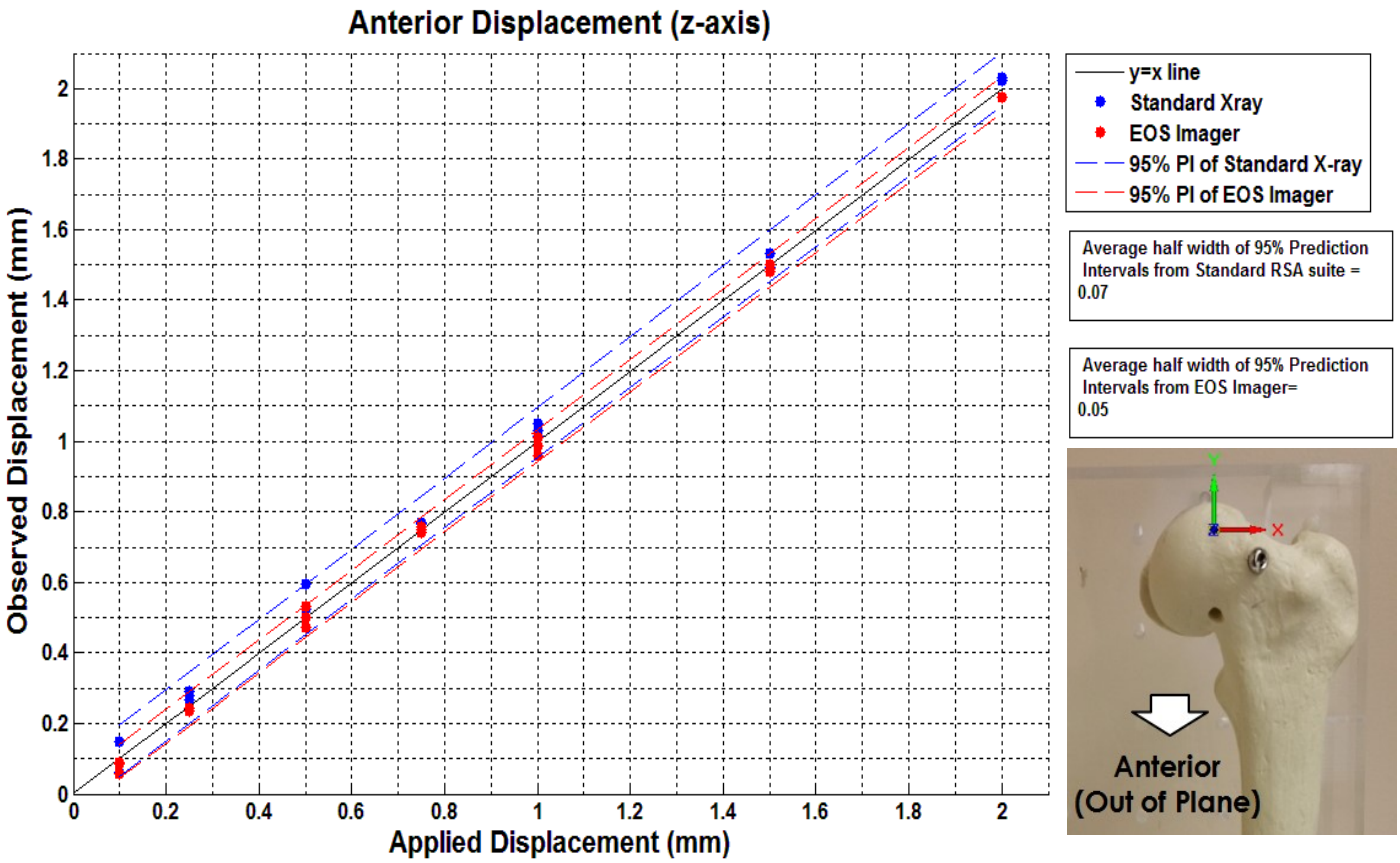

Figure 18: The accuracy of RSA in detecting anterior displacements between the epiphyseal and metaphyseal bead cluster in the standard RSA suite and the EOS imager. The average half widths of the 95% Prediction Intervals is presented on the right. Direction of **metaphyseal movement** is illustrated on the bottom right.

Phantom Rotations

Anterior-Tilt Rotation (about x-axis)

According to Figure 19, anterior tilt detection accuracy was 0.18° in the standard technique and lower in the EOS RSA technique at 0.25°, ($p<0.01$).

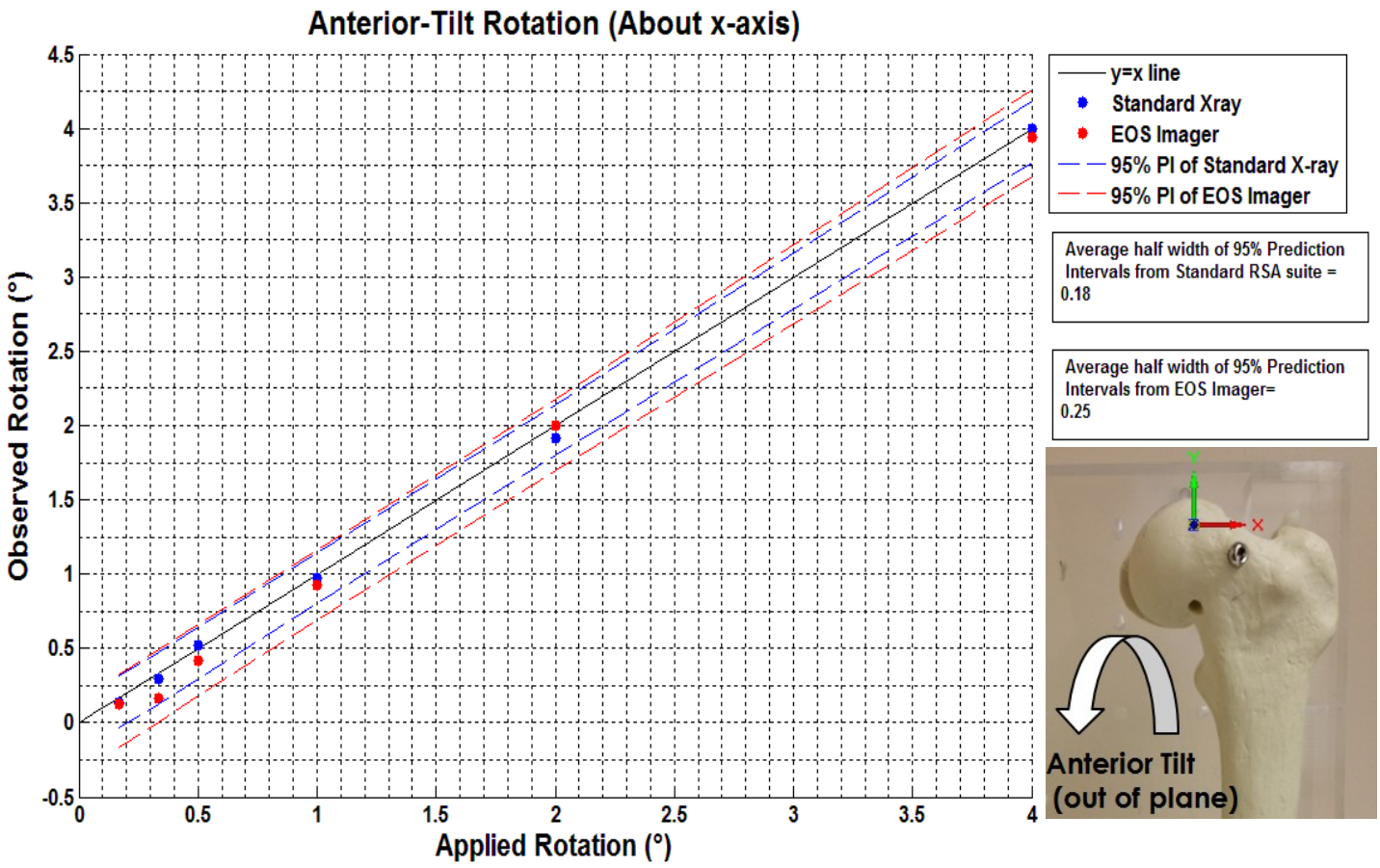

Figure 19: The accuracy of RSA in detecting anterior tilt rotations between the epiphyseal and metaphyseal bead cluster in the standard RSA suite and the EOS imager. The average half widths of the 95% Prediction Intervals is presented on the top right. Direction of metaphyseal movement is illustrated on the bottom right.

External Rotation (about y-axis)

The EOS technique was less accurate than the standard technique in detecting external rotations ($p<0.01$). The standard technique was accurate to 0.15° and the EOS RSA technique to 0.37° (Figure 20).

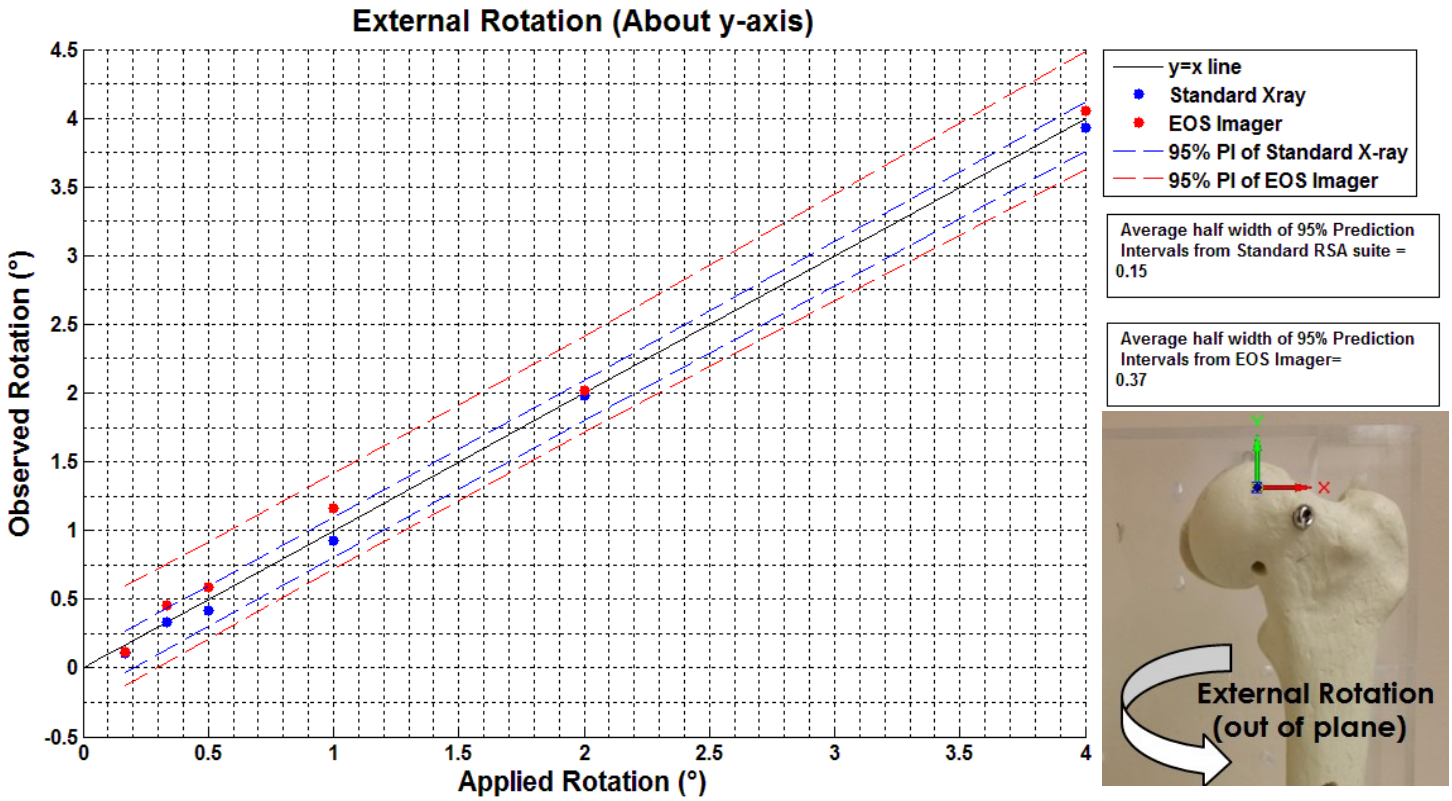

Figure 20: The accuracy of RSA in detecting external rotation between the epiphyseal and metaphyseal bead cluster in the standard RSA suite and the EOS imager. The average half widths of the 95% Prediction Intervals is presented on the top right. Direction of **metaphyseal movement** is illustrated on the bottom right.

Varus Rotation (about z-axis)

The accuracy of detecting varus rotation of the metaphysis was 0.14° in the standard technique and higher in the EOS at 0.08°, ($p<0.01$). The data is illustrated in (Figure 21).

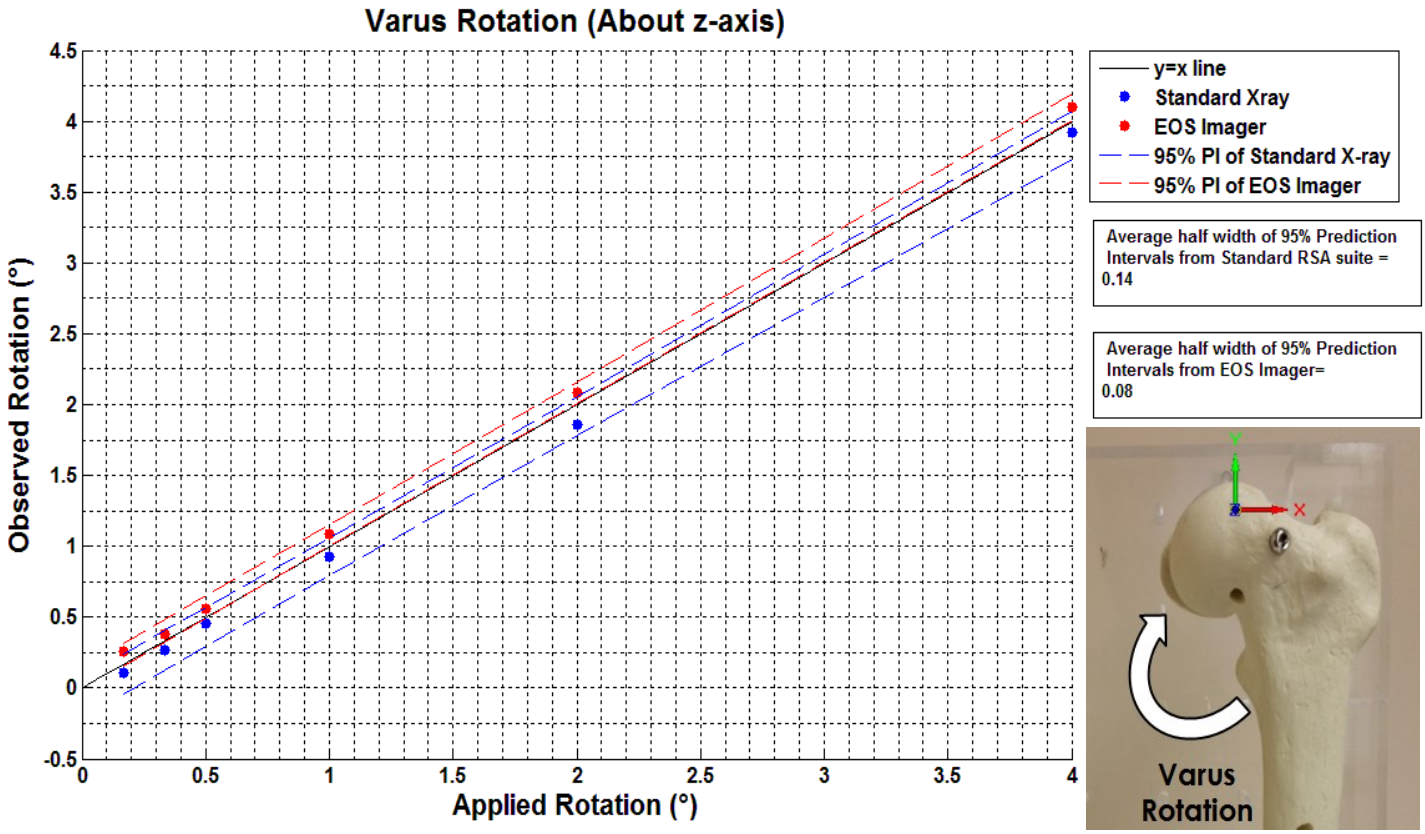

Figure 21: The accuracy of RSA in detecting varus rotation between the epiphyseal and metaphyseal bead cluster in the standard RSA suite and the EOS imager. The average half widths of the 95% Prediction Intervals is presented on the top right. Direction of **metaphyseal movement** is illustrated on the bottom right.

Accuracy Statistical Analysis

Measurement Bias

Table **7** presents the measurement bias for each nature of movement in each RSA technique.

Table 7: Measurement bias as a percentage of limit of clinical significance for both RSA techniques.

	Translation			Rotation		
	x	y	z	Rx	Ry	Rz
Standard RSA	4.8%	2.5%	11.3%	2.5%	4.4%	6.7%
EOS RSA	7.6%	6.5%	5.2%	6.1%	5.8%	7.0%

Bland Altman Plots

Figure 22 presents the limits of agreements of both imager-specific RSA techniques.

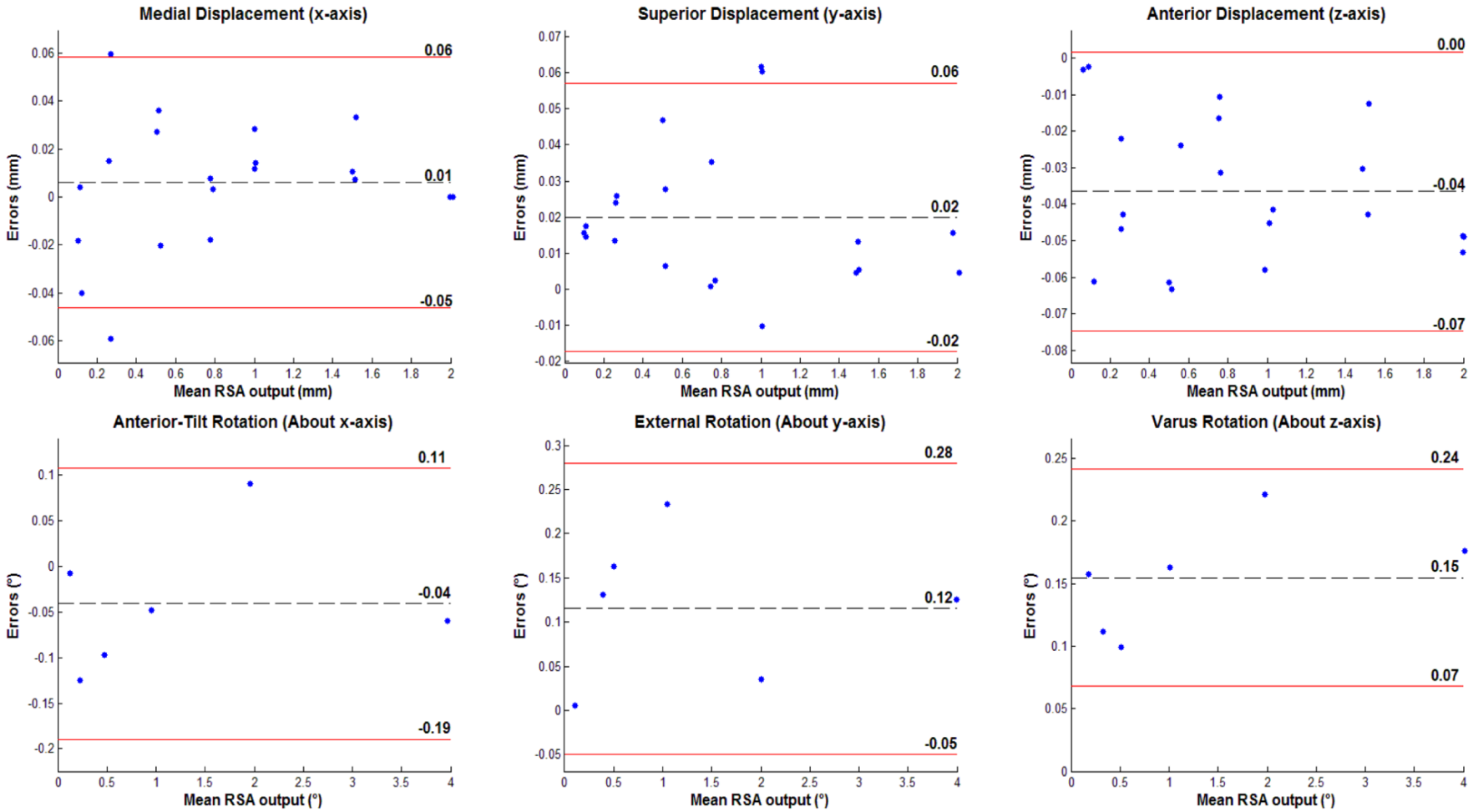

Figure 22: The Bland Altman limits of agreement for each nature of movement in each RSA technique (Bland & Altman 1986).

Phantom Precision

As a summary, Table 8 presents the results of all phantom precision tests completed in both systems.

Table 8: The results of the precision tests part of the phantom precision study. † indicates significant difference from conventional RSA technique.

Type of RSA exam	Completed in?		Precision Results (mm)						F-test		
	Standard Imager	EOS Imager	Standard Imager			EOS Imager			p-value		
			x Rx	y Ry	z Rz	x Rx	y Ry	z Rz			
i) Aligned pose at Isocenter	Yes	Yes	±0.05 0.32°	±0.03 0.24°	±0.02 0.06°	±0.04 0.36°	±0.03 0.15°	±0.06† 0.09°	*0.37* *0.90*	*0.87* *0.46*	*0.03* *0.27*
ii) Phantom displaced by ±10 cm in aligned pose	Yes	Yes	±0.09 0.36°	±0.16 0.18°	±0.06 0.12°	±0.12 0.38°	±0.17 0.28°	±0.07 0.10°	*0.62* *0.86*	*0.83* *0.27*	*0.89* *0.66*
iii) ±15° rotation about each axis at Isocenter	Yes	Yes	±0.11 0.30°	±0.37 0.31°	±0.25 0.09°	±0.22† 0.22°	±0.46 0.43°	±0.11 0.18°	*0.03* *0.46*	*0.37* *0.35*	*0.09* *0.07*
iv) ±15° rotation about each axis and ±10 cm displacement	Yes	Yes	±0.16 0.35°	±0.31 0.30°	±0.15 0.17°	±0.28 0.25°	±0.31 0.34°	±0.13 0.20°	*0.17* *0.24*	*0.98* *0.99*	*0.70* *0.86*
v) EOS Detector Extremities	No	Yes	Refer to Figure 23						Not applicable		
vi) 45° vertical axis rotation	No	Yes	Not Applicable			±0.06 0.19°	±0.10 0.12°	±0.07 0.14°	Not applicable		

RSA precision at EOS detector extremities

Figure 23 contains the precision of the EOS RSA technique centered and at detector extremities.

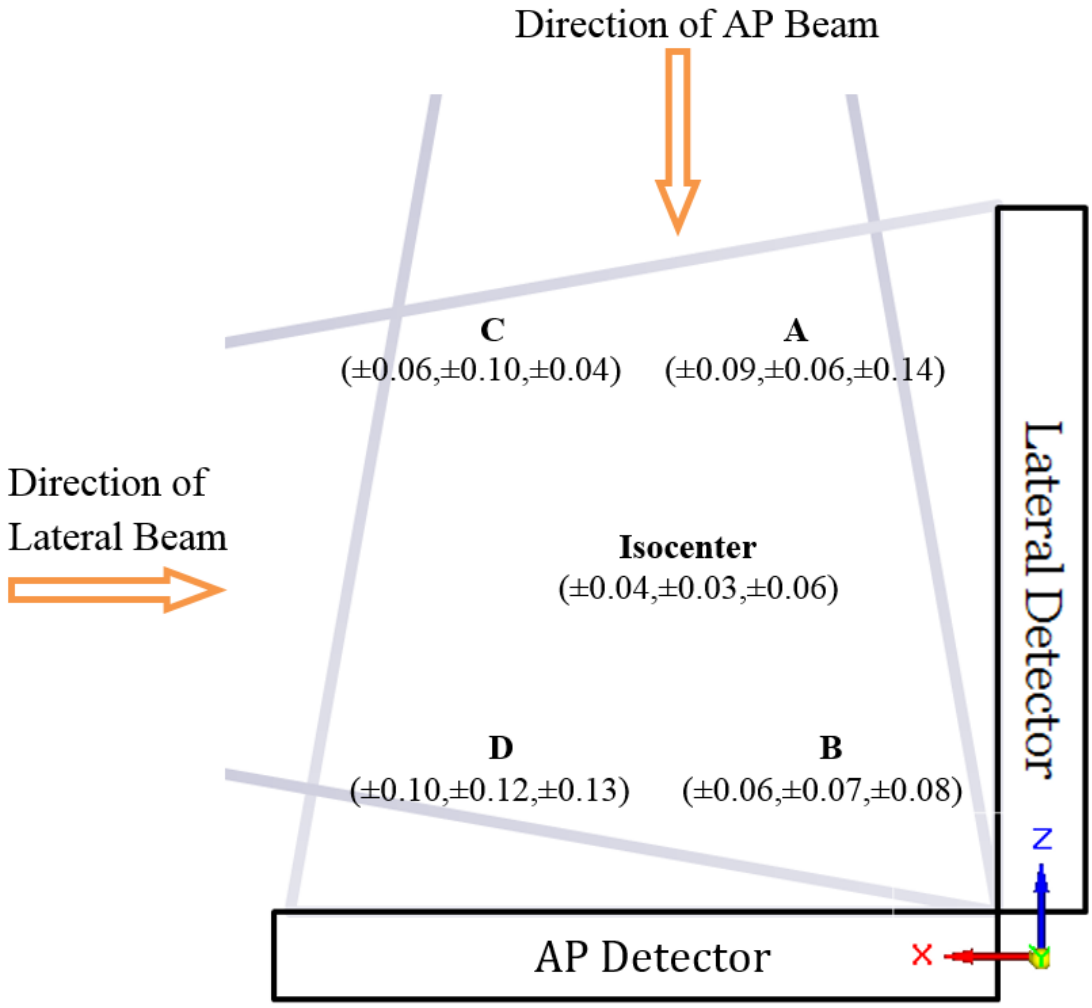

Figure 23: The locations of the phantom is represented with A, B, C, and D. The translational precision of the RSA technique in the EOS system (in mm), in Euclidian coordinates, is presented for each location.

DISCUSSION

Bead visibility was not problematic in analysis as more than 3 beads were matched in all clusters and in all radiographs, signifying adequate spatial freedom for an acceptable bead cluster in the proximal femur. Notably, bead implantation in the phantom was not constrained by intraoperative challenges of achieving an acceptable marker cluster configuration. The condition numbers and mean error of rigid body fitting in this phantom study were acceptable, residing

below 150 and 0.35mm, respectively (ISO 16087:2013). As markers were fixed in the model with liquid adhesive and the model was not subject to any load, variations in the mean error of rigid body fitting condition number output represents the noise in the RSA system and the effects of significant digits used in software.

Phantom Translations

The standard imager exhibited an accuracy in detecting medial, superior and anterior displacements of 0.05mm, 0.03mm and 0.07mm, respectively. Medial and superior movements occurred in-plane of both sources, while anterior migration occurred out-of-plane, resulting in lower accuracy in anterior migration detection. The explanation behind higher accuracy in detecting superior displacements over medial was inconclusive as both occur in-plane. Nevertheless, within the limits of clinical significance, a 20 μm difference in migration detection accuracy between axes can be considered negligible.

In the EOS imager, medial, superior and anterior displacement detection accuracy was 0.04mm, 0.04mm and 0.05mm, respectively. In medial displacements, beads migrated out of plane of the lateral source but in-plane of the AP source and during superior migration the beads migrated in-plane of both EOS x-ray sources explaining the equal accuracy in detecting both movements.

Anterior migration detection accuracy was lower than detecting superior and medial migration in the EOS by 10 μm likely due to the asymmetric source-detector distances in the two perspectives. Because the AP source was farther from the isocenter than the lateral, equal out-of-plane bead migration in both sources produced smaller magnification changes in the AP perspective than in the lateral. Subpixel marker centroid detection was prone to higher errors when detecting smaller changes in magnification. Moreover, the artificial increase in the resolution, part of EOS post-processing, in the AP radiograph interpolated bead projections onto a plane in the AP perspective that is equal to the lateral source-to-detector distance. This interpolation did not add actual signal to the image and therefore could not rectify the lower accuracy in detecting out-of-plane migration of the AP perspective. Generally, for movement along any of the three axes, beads migrated in-plane of at least one EOS source leading to nearly homogenous migration detection accuracy along any axis.

Overall, the standard RSA technique displayed higher accuracy in detecting superior migration while the EOS technique displayed higher accuracy in detecting medial and anterior displacements. The C-arm configuration allowing the precise localization of the source and detectors vital to the reconstruction of markers in Euclidean space potentially account for the improvement. A possible explanation for the worse superior migration detection accuracy in the EOS RSA technique is marker projection drift caused by vertical displacement of the EOS C-arm. This was primarily rectified in post-processing however could exist on a scale to bias superior migration detection accuracy producing the 10μm discrepancy observed between the standard and the RSA technique.

Phantom Rotations

In the standard technique, the accuracy of detecting anterior-tilt, external and varus rotation was 0.18°, 0.15° and 0.14°, respectively. Varus detection was more accurate than anterior-tilt and external rotation detection because in the latter two, metaphyseal beads moved out-of-plane of both sources. During varus rotation, the beads migrated in-plane of both imagers which led to higher accuracy in triangulating the beads and therefore rotational accuracy. Moreover, detecting anterior-tilt was less accurate than external rotation despite the beads migrating out-of-plane in both rotations due to influence of the marker cluster configuration. The small scatter of beads from the rotational axis during anterior-tilt rotations explains this departure. Small scatter around the axis of rotation led to lower induced bead migration thereby reducing detection accuracy.

The accuracy of detecting anterior tilt rotation was higher in the standard technique compared to the EOS likely due to the asymmetric source-to-detector distances in the AP and lateral perspectives in the EOS system. During anterior-tilt rotations, beads migrated out-of-plane of the AP source and in-plane of the lateral. The larger source to detector distance in the AP perspective meant that out-of-plane translations produced smaller bead magnification changes in the AP perspective. Smaller magnification changes resulted in less accurate overall subpixel localization during migration analysis; producing the lower accuracy in anterior-tilt rotation detection observed in the EOS imager.

External rotation accuracy was lower in the EOS than in the standard imager due to the metaphyseal bead cluster moving out-of-plane of both EOS sources. This out-of-plane movement, as previously described, correlated to increased errors in 3D reconstruction which produced increased errors in migration calculations. A previous report contains similar findings of biplanar RSA setups (Trozzi et al. 2008).

Detecting varus rotational accuracy was higher in the EOS than in the standard technique. This was despite the beads migrating in-plane of both sources in the standard technique and only in-plane of the AP detector in the EOS migrating. It is theorized that in the lateral perspective the smaller source-isocenter distance produced higher bead magnification changes during out-of-plane movement leaving this perspective not as susceptible to reduced subpixel detection as the AP perspective. Furthermore, the C-arm configuration likely contributed to highly accurate subpixel localization in the EOS RSA technique explaining the difference in varus rotation detection accuracy over the conventional technique.

Overall, the EOS imager exhibited statistically higher accuracy in only detecting varus rotations over the standard technique. In this phantom study, the accuracy limits of agreement of both techniques fell within the limits of clinical significance of 0.22mm and 1.12° and detection bias for all natures of movement existed below 10% of this threshold. Furthermore, the accuracy of both techniques in this work lie within the accepted RSA accuracy bounds of 0.05mm and 0.5mm and 0.15° and 1.15° (Valstar et al. 2002).

Phantom Precision

Precision centered in FOV

The translational and rotational precision of the EOS RSA technique was not significantly different than the standard technique, except in detecting z-axis translations. The explanation for this phenomenon is related to the larger AP source to detector distance in the EOS imager and potentially the absence of contour detection step in the EOS subpixel localization technique. Markers migrating out of plane of the AP source produce small variations in marker projection radii; these changes can be more precisely detected with contour detection. Incidentally, the higher z-axis precision in the conventional technique seen in this study is atypical of previous reports (Solomon et al. 2010; Laende et al. 2009). Nevertheless, the overall

precision of both techniques in this work lie on the same order of magnitude seen in these reports.

Phantom axes aligned with ±10 cm Displacements

The standard and EOS RSA techniques were susceptible to reduced precision at ±0.16mm and ±0.17mm, respectively, when the phantom was imaged ±10 cm off-center with no statistical significance between techniques. The likely explanations for the decrease in both techniques over their isocenter-precision stems from the dispersive nature of x-ray beams unique in each imager. Beam dispersion off-centre increased eccentricity of bead projections thereby increasing errors in subpixel marker centroid detection. Notably, calibration markers, part of the standard technique and significant post-processing, part of the EOS technique, counteracted said distortion leading to precision on the same magnitude order observed in both techniques.

Phantom imaged centered in FOV with ±15° rotation

The introduction of misalignments to the phantom construct the precision of the technique decreased to ±0.3mm in the standard imager and to ±0.4mm in the EOS, with no statistical difference. Misalignments decreased RSA fidelity because modulating bead cluster pose between RSA exams also influenced 3D location of marker cluster centroids. Errors in 3D locations of cluster centroids produced the errors seen in this test; especially so in y-axis precision. Due to the spatial constraints of the proximal femur the epiphyseal marker cluster did not exhibit high scatter along the y-axis. The nearly coplanar nature of the epiphyseal markers is susceptible to higher errors in cluster centroid detection along the y-axis producing the lower precision observed in this test.

Statistical difference was found in detecting x-axis translations between imagers in this test; it however, was not considered to have clinical implications as it was below the clinical significance threshold.

Phantom imaged with ±10 cm Displacement with ±15° Rotations

There were no statistical differences found between techniques in this test. The beam configuration unique to each imager and errors in marker cluster centroid locations as a result of

pose modulation accounts for the lower precision of both techniques in relation to the test at isocenter. Although a displacement of 10 cm and a rotation of 15° between scans is unlikely in the in-vivo setting; in this worst-case scenario, a precision better than ±0.3mm and ±0.4° is expected in the EOS and in the standard technique. Similarly, perfect patient positioning repeatedly centered in the field of view is unexpected as well. Therefore, true RSA precision solely due to improper patient positioning irrespective of imaging modality lies between ±0.06mm and ±0.5mm and ±0.3° and ±0.4°.

EOS RSA precision at detector extremities

The RSA technique in the EOS was susceptible to lower precision when imaged at detector extremities. At detector extremities, the precision of the technique decreased to ±0.14 mm. The reason behind this decrease stems from the EOS x-ray beam configuration. The dispersive nature of the fan-beam x-rays increased eccentricity of bead projections when imaged off-center; increasing errors in subpixel localization and thereby decreasing precision.

The EOS RSA technique was further susceptible to reduced accuracy when imaged off the line equidistant to both detectors (Figure 24). Positions A and D, exist off said line and exhibited a subsequently lower precision. At position A, the distance to the AP detector was greater than the distance to the lateral detector and at position D, the distance to the lateral detector was greater than the distance to the AP. This led to asymmetric marker projections on both detectors. The differing marker projection sizes unduly influenced subpixel localization in one perspective producing the lower precision observed. Positions B, C and the isocenter exist on the line equidistant to both detectors where magnification factors in both perspectives were equivalent. When imaged on this line, improved accuracy was observed.

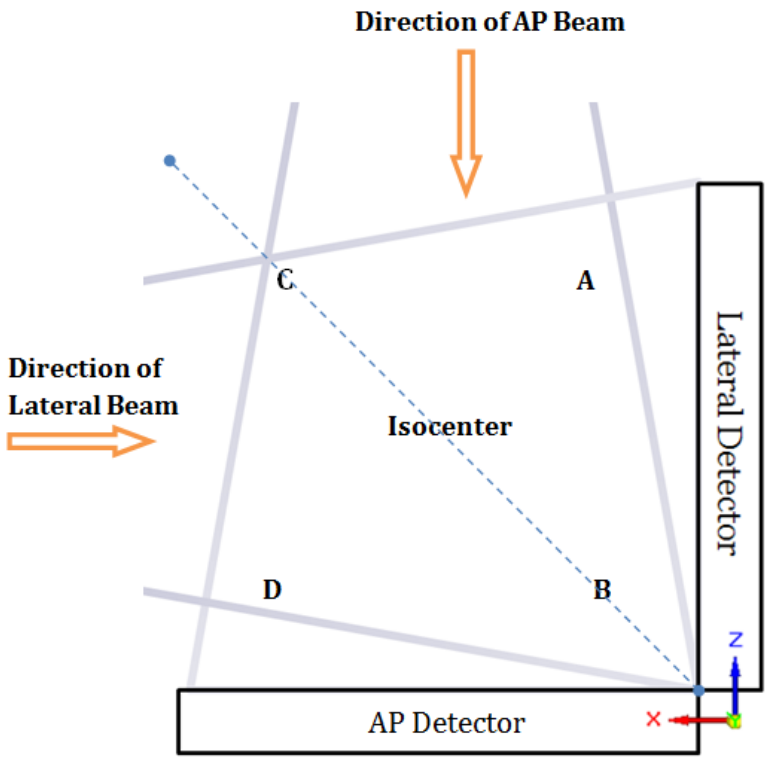

Figure 24: The precision of the EOS RSA technique in a SCFE model at various locations within the imaging volume.

Precision with 45° anatomical rotation in the EOS imager

The precision of the EOS RSA technique was not found to be affected by 45° anatomical rotation about the vertical axis. Translational precision values below ±0.1mm were observed comparable to the aligned pose precision at isocenter. Rotational precision was homogenous about each axis due to the crosstalk between axes of higher and lower precision, supported by previous reports employing biplanar setups (Trozzi et al. 2008; Gascoyne et al. 2014).

Generally, the results of the phantom study conducted in the standard and EOS RSA technique coincide well with previous reports indicating true RSA precision existing between 0.05mm and 0.6mm and 0.3° and 2° (Kärrholm et al. 1997). Literature reported values indicate that limits of clinical significance following growth plate ablation are between 0.22 and 0.52 mm and 1.12° (Gunderson et al. 2013; Khoury et al. 2007). The novel implementation of the RSA technique exhibited precision below these thresholds.

Current limitations and Future Work

The absence of calibration markers for RS analysis is a welcome change over the conventional technique however, the EOS RSA technique is susceptible to lower precision off-center. To reconcile this shortcoming, subpixel localization software robust against differing marker projection magnification, introducing calibration markers on EOS radiographs or further testing off-center allowing the characterization and therefore rectification of marker projection distortion in post-processing can all offset the lower off-center precision.

Another shortcoming of the phantom approach was the absence of stochastic x-ray attenuation common in the in-vivo setting as a result of osseous structures and soft tissue mass. Non-uniform attenuation would better simulate the in-vivo setting and therefore would better reconcile potential differences between phantom and in-vivo applications. With non-uniform x-ray attenuation, occlusion of implanted beads is a larger possibility and the variable occlusion of beads would better simulate the in-vivo setting.

An avenue for improved accuracy is improved image segmentation techniques. Improved bead contour detection software and signal simulation in template matching robust against bias from nearby contrasting edges will allow better feature detection contributing to improved subpixel localization. This will result in more accurate 3D triangulation and therefore improved accuracy of this novel implementation.

In an effort to exclude errors in the in-vivo setting stemming from patient misalignment and improper positioning, an implant- or patient-specific local coordinate system could be developed based on bony landmarks and/or conspicuous anatomical features to define the cardinal axes. Doing so would exclude kinematic crosstalk resulting from anatomical and global coordinate system misalignment during clinical implementation. One approach is using a line intersecting the femoral head centers to define a transverse axis and the longitudinal axis of the femur to define the vertical axis. The axis orthogonal to the aforementioned would define the sagittal axis. Inter-cluster movement can then be defined using this anatomical coordinate system excluding kinematic crosstalk as a result of patient misalignment.

CONCLUSION

Within the SCFE model, the EOS RSA technique exhibited comparable translational and rotational accuracy and precision to the standard technique. Furthermore, the EOS RSA technique demonstrated an accuracy and precision better than the threshold indicated clinically significant for post-surgical physeal fusion assessment. The EOS technique was susceptible to lower precision when imaged off-center indicating paramount need for proper patient positioning during in-vivo exams. Steps were taken to mimic soft tissue attenuation, however a greater potential source of bead occlusion and deformation due to osseous structure and patient motion artefact was not emulated in this study. These are expected to negatively affect the in-vivo precision. Nevertheless, this phantom study demonstrated an RSA accuracy and precision better than 0.05mm±0.06mm and 0.37°±0.36° in the EOS modality while the standard application of RSA displayed an accuracy and precision better than 0.07mm±0.05 mm and 0.18°±0.32°. A side by side comparison of the accuracy of the RSA technique within both imaging modalities is presented in Table 9.

Table 9: Side by side comparison of the accuracy of the RSA technique in the standard RSA suite and the EOS imager.

Nature of Movement	Standard RSA	EOS imager
Medial Displacement	0.05 mm	0.04 mm
Superior displacement	0.03 mm	0.04 mm
Anterior Displacement	0.07 mm	0.05 mm
Anterior Tilt	0.18°	0.25°
External Rotation	0.15°	0.37°
Varus Rotation	0.14°	0.08°
Precision (x,y,z) (Rx, Ry, Rz)	(±0.05mm, ±0.03mm, ±0.02mm) (±0.32°,±0.24°,±0.06°)	(±0.04 mm, ±0.03 mm, ±0.06 mm) (±0.36°,±0.15°,±0.09°)

Several other applications stand to benefit from the accuracy and reduced radiation dose of the novel implementation of this RSA technique. These improvements can be extended to scoliosis, fracture fixation, and percutaneous epiphysiodesis models, among others. A

supplemental benefit of the EOS RSA technique is the reduced radiation dose associated with this modality. This is a welcome advantage over conventional methods in the adult and paediatric populations; more so for the latter.

Chapter 4: In-Vivo Demonstration of Radiostereometric Analysis in the EOS imaging modality

INTRODUCTION

Radiostereometric Analysis (RSA) is a technique to quantify rigid body motion in orthopaedic applications (Selvik 1989). It has previously been used in research studies to link post-surgical motion to post-surgical implant survivorship (Ryd et al. 1995; Kärrholm et al. 1994). Through the use of implanted markers and a stereo perspective, it allows the three-dimensional tracking of markers facilitating post-surgical implant stability assessment. The utility of this technique lies in its accuracy which is reported to exist between 0.05 and 0.5 mm and 0.15° and 1.15° (Valstar et al. 2002). RSA has been instrumental in linking post-surgical knee and hip implant micromotion to implant survivorship (Kärrholm et al. 1994; Ryd et al. 1995; Pijls et al. 2012); however, its application in paediatric populations has been limited. This is potentially due to the radiation dose associated with each RSA exam. Cumulative radiation dose resulting from repeated exposures has been shown to increase prevalence of cancer (Ronckers et al. 2010).

The EOS system (EOS Imaging, Paris, France) is a low-dose bi-planar imager with three-dimensional reconstruction capabilities that uses fan beam x-rays to construct standing sagittal and frontal images of subjects. It contains isotropic 254 μm pixels with a resolution of 193x185 μm and 179x185 μm, in the frontal and lateral perspectives, respectively (Deschênes et al. 2010). This contrasts with the Canon CXDI-55C digital x-ray flat-panel detectors in the local RSA suite with an imaging area of 35 cm x 43 cm and a pixel size of 160x160μm (Canon USA, Inc., Lake Success, NY). The EOS offers 1:1 magnification full-body standing images of patients, or any part thereof; offering unique diagnostic value. A full body scan requires up to 20 seconds while a lower limb scan requires up to six seconds, dependent on subject height and radiograph acquisition speed (Deschênes et al. 2010). The x-ray sources and detectors mounted on a C-arm descend during a scan to capture radiographs.

The low radiation dose EOS modality is a potential candidate for the implementation of a novel RSA technique. The phantom study has demonstrated acceptable accuracy and precision of the EOS RSA technique in the SCFE model (Chapter 3). There has been no in-vitro or in-vivo

demonstration of RSA in the EOS imaging modality. Currently, no cohort of paediatric population exists at the local children's hospital with RSA beads previously implanted to recruit into this study. Therefore, a Total Knee Arthroplasty (TKA) cohort was explored. TKA is a procedure conducted to replace knee joints deteriorated by osteoarthritis and rheumatoid arthritis. Surgeons at the local hospital implant 16 RSA beads in three separate bead clusters; tibial, femoral and polyethylene bead, illustrated in Figure 25 (Dunbar et al., 2009; Wilson et al., 2010 and 2012).

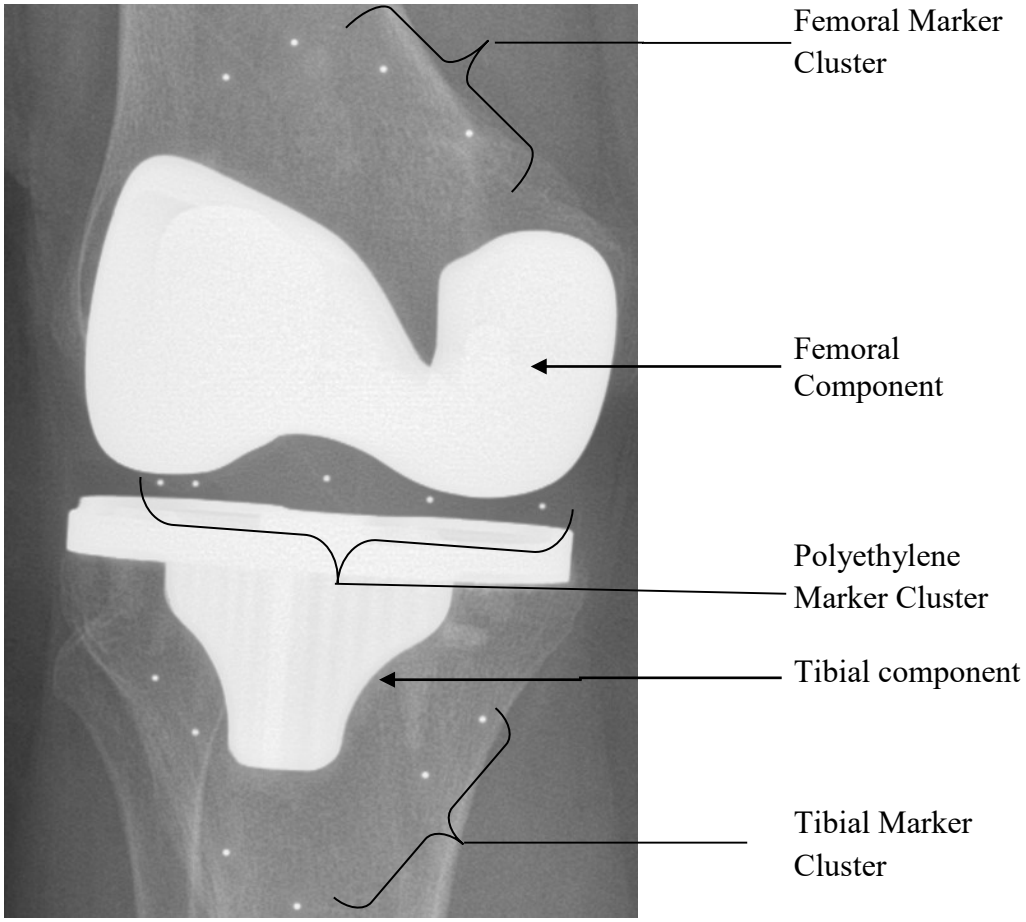

Figure 25: Posterior-anterior radiograph of a typical total knee replacement highlighting implant components and RSA marker clusters.

The purpose of this proof-of-concept study was to demonstrate RSA in the EOS imaging modality using human participants with implanted beads, and to indicate the in-vivo precision of this technique. This study primarily investigated the effect of patient motion artifacts, along with the increased pixel widths of the EOS and vertical translation of EOS C-arm on the in-vivo precision of the RSA technique.

METHODS

Participants were identified and recruited for participation in this study from a cohort part of a larger study (REB #2010388) in Nova Scotia Health Authority (NSHA) Halifax Infirmary Orthopaedic Department looking to assess post-operative total knee arthroplasty tibial implant stability. All participants agreed to be contacted for further and future studies. Exclusion criteria was: less than 2 years since arthroplasty, revision surgery after arthroplasty, and serious or uncommon postoperative pain. Three participants were recruited and invited to attend a single visit at the IWK Health Centre. Following the consent process, the participants changed into Johnny gowns. Immediately prior to imaging, the calibration protocol developed in LIO (Laboratoire de recherche en imagerie et orthopédie, Montreal, Canada) was run and is described in detail in Chapter 3. Next, with the help of a Diagnostic Imaging Technologist, participants were positioned inside the imager so the sagittal and transverse anatomical axes were offset 15° to both EOS beams in an effort to minimize super positioning from contralateral knee (LIO, Montreal, Canada).

a)  **b)** 

Figure 26: The subject stood in double leg stance with anatomical frame rotated by 15°. The subject gripped hand during the scan.

The participants stood in double leg stance, feet parallel to each other, shoulder width apart and the operated knee positioned at the isocenter (Figure 26). Subjects gripped handles to

minimize motion artefact. The commencement and termination of the scan was 10 cm above and below the condyles, respectively.

At the EOS workstation, the beam strength was set to 80 kV and 200 mA for both beams corresponding to the standard values for a lower limb scan. The vertical translation speed of the X-ray beams was set to '4' corresponding to the C-arm descending at a rate of 4.57 cm/s. The presence of knee prostheses was indicated in EOS workstation. The reference planes were set to intersect perpendicularly at the isocenter, defined as the point of intersection of both EOS x-ray beams in the imaging column. With this, two radiographs were produced.

Following the initial image capture, the aforementioned image capture protocol was repeated once more for each participant, concluding the zero displacement double exam (Bragdon et al., 2002; Nebergall et al., 2015; ISO 16087:2013). The acquisition of four radiographs per subject concluded the image capture protocol.

Radiographic Analysis

Radiographs were loaded into MATLAB 2014a and analyzed with programming code developed jointly with LIO (Montreal, Canada). Bead detection algorithm utilized in the analysis is described in greater detail in Chapter 3. Briefly, coarse detection of beads was based on user prompted initial estimate and subpixel localization was performed with simulated template matching with normalized cross correlation (Jurie & Dhome 2002; Briechle & Hanebeck 2001). One hundred forty-four sub-pixel shifted beads were simulated and correlated with each initial estimate. The simulated template with highest correlation to the detected signal was used to determine the subpixel location of each bead.

Marker projections from both radiographs facilitated the reconstruction of each implanted marker in Euclidian space, using the height of the scan and distance from the left edge of the detectors. With all beads reconstructed in Euclidean space, migration analysis was performed between the polyethylene and tibial bead clusters, with the latter as the reference. Euler rigid body kinematic analysis, based on singular value decomposition method described in detail in (Valstar et al. 2002) and (Challis 1995), was used to determine relative micromotion occurring between two subject scans. Relative migration and rotation along and about the x-, y- and z-axes

was recorded for each subject along with the Condition Number, Mean Error of Rigid Body Fitting, Maximum Total Point Motion (MTPM) as per (ISO 16087:2013).

Precision was based on the Standard Deviation (ISO 16087:2013). The Standard Deviation of the observed translations and rotations in each plane was calculated in Microsoft Excel 2014.

RESULTS

Table 10 presents subject demographics, the output of RS analysis for each subject and the precision of the in-vivo EOS technique.

Table 10: The results of migration analysis for Total Knee Arthroplasty (TKA) subjects utilizing the EOS RSA technique.

Subject Demographics	Translation (mm)			Rotation (°)			#Matched Markers		Rigid Body Error (mm)		Condition Number		MTPM (mm)
	x	y	z	Rx	Ry	Rz	Migrating	Reference	Migrating	Reference	Migrating	Reference	
Subject 1- Gender: F Age: 68 Weight: 83kg BMI - 35.74 Post-op: >3 yrs	-0.21	-0.01	0.42	-0.07	0.08	0.10	3	5	0.0298	0.0351	41.5	47.4	0.528
Subject 2- Gender: F Age: 69 Weight: 94kg BMI - 34.49 Post-op: >4 yrs	0.35	0.05	0.44	-0.30	-0.02	-0.29	5	5	0.0382	0.1058	27.7	49.2	0.592
Subject 3- Gender: F Age: 68 Weight: 93kg BMI - 33.71 Post-op: >3 yrs	-0.25	0.01	-0.30	0.58	0.39	0.05	3	5	0.0189	0.1326	180.7	47.8	0.479
PRECISION	**±0.67mm**	**±0.06mm**	**±0.84mm**	**±0.91°**	**±0.42°**	**±0.42°**							

DISCUSSION

This study was the first demonstration of the RSA technique in the novel EOS imager with a precision higher than ±0.84mm and ±0.91°. Reported precision of RSA employing conventional radiography lies between 0.15mm and 0.6mm and 0.3° and 2° (Kärrholm et al. 1997). The precision of the EOS technique, although near the limit of accepted RSA precision, was on the same order of magnitude seen previously.

The first subject was imaged off-center in the first exam and then repositioned at the isocenter in the subsequent. The first exam being in suboptimal conditions contributed to the observed migration. The second subject was imaged at the isocenter in both exams, however indicated extraordinary difficulty in maintaining static posture during the scan possibly explaining the observed migration and increased mean error of rigid body fitting in the tibial cluster. Due to excessive leaning of the third subject, bead visibility in both scans was minimal contributing to the high Condition Number in the migrating cluster. Results from this subject merit suspicion as clusters with higher Condition Number negatively affect rotational precision (Onsten et al. 2001). High rotational results from this subject disproportionately influenced the overall rotational precision, as well.

Overall, the precision along the x- and z-axes was an order of magnitude greater than observed migrations along the y-axis. A likely explanation is patient motion as movement along the x- and z-axes between scans was likely but along the y-axis (i.e. change in patient height) was not. This accounts for the order of a magnitude difference in accuracy along the y-axis over the remainder.

The fixation of the beads in the polyethylene liner was not expected to be different from fixation in bone. Furthermore, stable fixation in both mediums was expected between scans facilitating a candid assessment of system precision. Migration analysis was performed under this assumption as there have been no reports of bead instability or independent migration of tantalum markers (Alberius 1983).

The added benefit unique to this novel implementation is the reduced radiation dose associated with each RSA exam. Additionally, as per the results of the phantom study, the

current embodiment of the RSA technique in the EOS does not require the presence of calibration markers in radiographs to facilitate RS analysis. The lack of calibration beads excludes any likelihood of calibration-marker projections occluding implanted-marker projections. The absence of calibration markers however also contributes to the decrease in RSA precision off-center, as seen in the phantom study.

The amount of post-surgical micromotion following physiodesis exists between 0.22mm and 0.52mm and at 1.12° (Gunderson et al. 2013; Khoury et al. 2007). It remains to be seen whether the EOS RSA technique offers translational and rotational precision below these thresholds.

Limitations:

The largest departure from the phantom study was the employment of the technique in the adult total knee replacement model as opposed to the paediatric SCFE hip. In the former, the presence of substantial hardware and differing RSA bead clusters were the largest irreconcilable differences. Despite these differences, EOS RSA accuracy in SCFE is expected to be on the same order of magnitude as seen in this study.

Beam characteristics utilized in this study were not optimized for RS analysis. Further investigation can optimize kV and mA values for visibility while maintaining controlled exposure to radiosensitive tissue, optimizing subpixel marker localization.

Bead visibility was problematic in all subjects and recommended number of matchers markers were not used in analysis (ISO 16087:2013). This is partly due to the bead implantation protocol employed intraoperatively was optimized for the uniplanar RSA suite of the local hospital and partly due to the patient positioning protocol employed is susceptible to subject lean. An optimized protocol will decrease patient related factors that deteriorate visibility.

Another limitation not specific to the TKA cohort was motion artefact during scan. A lower limb EOS acquisition requires up to 6 seconds depending on the scan distance and system settings. This increased time span introduces patient motion during acquisition leading to increasing marker projection distortion and drift, negatively affecting RSA precision.

The precision of the EOS RSA technique is expected to be lower than the precision seen in this study due to inherently larger periarticular soft tissue in the hip. To counter significant soft tissue attenuation, and to mitigate super positioning by contralateral hip, post-operative hip scans can potentially be conducted with the anatomical and EOS axes offset by 45°. This patient orientation, emulated in the phantom study, does not negatively affect the precision of the technique.

Future Work

A calibration object present in EOS radiographs can rectify patient motion artefact. For example, a radiolucent - but visible - vertical bar attached to the subject during a scan would allow the quantification of patient motion by examining deformation in the radiographic projection of the vertical edge. Rectifying this deformation would mitigate patient motion that confounds in-vivo EOS RSA results.

To rectify improper patient positioning, further testing off-center with a calibration cage will allow the quantification of bead projection deformation at various locations within the imaging volume. Observed deformations can be rectified in post-processing or through improvements in the calibration procedure, potentially mitigating the lower precision of EOS RSA off-center seen in the phantom study. If this does not provide the clinically relevant precision sought, calibration markers on EOS radiographs may be warranted.

CONCLUSION

The EOS RSA technique was more precise than ±0.84mm and ±0.91°. The effects of motion artifacts, larger pixel widths and vertical displacement of the C-arm were elucidated and not found to substantially decrease the precision of this novel implementation over the conventional technique. Nevertheless, the preliminary results of this implementation merit further investigation with larger and more variable subject population and in models that allow analysis with recommended number of markers before clinical application of EOS RSA in the post-surgical SCFE population.

Chapter 5: Conclusion

Summary

The phantom model study in Chapter 3 investigated the effects of larger pixel size and vertical translation of C-arm under the hypothesis that both would lead to lower RSA accuracy and precision in this novel implementation. This hypothesis was rejected due to the EOS RSA technique demonstrating comparable accuracy to the conventional technique. Several reasons explain this finding including: The C-arm configuration of the EOS system, significant post-processing on EOS radiographs and normalized cross-correlation template matching procedure employed in subpixel localization. The calibrated C-arm facilitated precise spatial awareness of the EOS source and detectors over the temporal domain. In calibration step errors in source-detector distances and discrepancies in source-detector heights along with perturbations in the orthogonal axes of the detectors were quantified and corrected. The vertical drift and eccentricity of bead projections were significantly rectified with proprietary EOS post-processing. The C-arm configuration, allowing the precise determination of marker projection radii, laid the framework for the utilization of a template matching technique. The concurrent effects of these three elements contributed to the high accuracy and precision of RSA in the EOS modality.

Chapter 3 demonstrated the provenance of the in-vivo RSA technique with the EOS modality. To establish the utility of this novel application, the precision of the technique was characterized under the hypothesis the vertical translation of C-arm spanning several seconds during a scan would introduce motion artefacts decreasing precision. This hypothesis was not rejected because the in-vivo precision of the technique was better than ±0.84mm and ±0.91°, near the limit of currently accepted precision of the conventional RSA studies (Kärrholm et al. 1997). The likely explanation for low precision is patient motion artefact made possible by the increased time associated with the EOS acquisition- spanning several seconds. The observed precision along the x and z axes was an order of magnitude worse than along the y-axis, supporting this conclusion. It remains to be seen whether EOS RSA offers the in-vivo precision required for post-surgical assessment in SCFE cohorts.

Thesis Impact

The work of this thesis contains the novel implementation of the RSA technique in the EOS imaging modality. This represents a significant leap for the RSA body of research and EOS modality alike. The reduced radiation dose of the EOS imager combined with the high accuracy of the RSA technique presents substantial benefit to the paediatric and adult population.

The development of a RSA marker placement protocol in the proximal femur also presents a significant addition to the paediatric orthopaedic and RSA research realms. The likelihood of intraoperative implementation of this protocol remains to be seen. Furthermore, the intraoperative repeatability of this protocol is uncharacterized. The closed surgical and the dimensional constraints of the paediatric proximal femur along with the anterolateral approach and the presence of the fixation screw(s) all present challenges in the successful and reliable implementation of this marker placement protocol. The deposition is further challenged by the presence of the artery of Brodetti in the posterior-superior quadrant, which should be avoided to diminish risk of blood supply withdrawal.

An additional benefit of the RSA technique in the EOS imager is that a calibrated EOS system does not require the presence of control or fiducial markers in radiographs for RS analysis. Therefore, no bead occlusion of implanted markers due to control or fiducial markers in EOS radiographs is expected. Moreover, the biplanar set up of the EOS system provides higher visibility compared to the uniplanar set up of the conventional x-ray suites (Cai et al. 2008; Trozzi et al. 2008; Gascoyne et al. 2014). The higher bead visibility in the EOS is expected to increase accuracy of EOS RSA compared to the standard technique.

Clinical Implications

The results of the thesis suggest favourable clinical implications in the post-surgical SCFE and TKA populations. The phantom study indicated that within the confines of the SCFE model, RS analysis was possible and provided acceptable system accuracy and precision in detecting literature indicated post-surgical micromotion. This result provides support to the framework of implementing the EOS RSA technique in the postoperative SCFE population for fusion assessment, following further testing. Preliminary in-vivo precision was an order of

magnitude lower than precision in the phantom study. Patient motion artefact, less than optimal patient positioning, presence of soft tissue and lower than recommended number of beads used in analysis predominantly explains the in-vitro and in-vivo discrepancy of EOS RSA precision. Further in-vivo testing with a bead placement optimized for EOS visibility and recommended number of beads used in analysis are all expected to better indicate the true precision of this technique. In an effort to mitigate patient motion artefact the implementation of a vertical calibration bar attached to patient during EOS scans is warranted.

Technical Implications

This thesis demonstrates a significant addition to the RSA literature as the first demonstration of this technique in the novel slot scanning x-ray imager. Furthermore, the accuracy of the EOS technique was comparable to the standard technique. Analysis without a calibration box was possible by the C-arm configuration of the EOS, allowing the precise spatial localization of source and detectors at all time points during a scan. The absence of calibration markers on radiographs in the current embodiment of the EOS RSA technique further increases its accessibility for research centers around the world as dedicated RSA suites and hardware modifications to the EOS system are not necessary.

Limitations

A prominent limitation was the small subject population of the in-vivo study in (Chapter 4). In RSA studies, a study population of N=15 is the recommended lower limit (ISO 16087:2013). A larger and variable subject population is expected to better indicate the in-vivo precision of the EOS RSA technique.

Patient motion confounded the results of the in-vivo study and resulted in precision near the accepted limit of previous RSA studies employing conventional radiography (Kärrholm et al. 1997). This artefact also challenged the assumption of no movement between zero displacement double exams.

Recommendations and Future directions

The phantom precision study suggested that due to the fan beam configuration of the EOS x-rays, imaging off-center increased errors in bead triangulation reducing accuracy of RSA. Preliminary in-vivo exploration suggested patient motion unduly affected the precision of this technique. The results of the thesis work suggest an optimal patient positioning protocol allowing repeatable stabilized positioning at the isocenter is vital for RS analysis. To counteract patient motion artefacts incorporating a vertical calibration bar during EOS RSA exams warrants exploration. To offset lower off-center precision further testing at detector extremities allowing the quantification of distortion, and therefore the calibration required, warrants investigation. Furthermore, optimizing x-ray beam characteristics is expected to result in improved segmentation and visibility leading to higher RS analysis fidelity.

In an effort to minimize or exclude patient positioning variability a local anatomical coordinate system merits development. This system built from anatomical landmarks or features common in all post-operative radiographs (i.e. fixation screws) would also increase RSA fidelity across patients.

A stipulation underlying the thesis work was adequate intraoperative access to the proximal femur for bead cluster implantation. Mimicking a closed fixation surgical procedure, steps were taken to imitate constrained access to the proximal femur, like implanting RSA markers not exceeding a perpendicular distance of 1 cm from the longitudinal axis of the screw. Nevertheless, to be clinically possible, an improved implanting device over the conventional straight tip bead inserter (i.e. a 'curved' bead inserter) and a jig is likely needed to achieve adequate and repeatable marker spread intraoperatively. This would utilize a single incision to deposit an adequate bead cluster mitigating damage to surrounding vascular structures and retrograde femoral blood circulation.

Following the successful demonstration of the EOS RSA technique with SCFE radiographs, the benefit of this technique will increase further with the implementation of an inducible displacement protocol as the two in tandem will allow an instantaneous postoperative assessment of physeal fusion. This will build the framework to develop metrics related to persistent physeal non-union. In the event an inducible displacement protocol does not afford

diagnostic advantage, the employment of RSA to quantify long term migration in the SCFE hip will still prove useful in the clinical setting as serial RSA examinations over the postoperative period can indicate the persistence of physeal non-union. The results of pooled examinations can lead to the development of metrics indicating postsurgical success or failure.

The high accuracy and low radiation dose of this novel technique warrants its expansion to other postoperative orthopaedic models requiring prosthesis stability assessment. In the paediatric realm, this technique offers acceptable accuracy in assessing stability following spinal fusion, percutaneous epiphysiodesis and fracture fixation. Limits of clinical significance in lumbosacral micromotion leading to successful spinal fusion has been found to be 0.3mm, 0.5mm, and 0.7mm in the transverse, frontal and sagittal planes, respectively (Pape et al. 2002). Similarly, in the knee epiphysiodesis model, 0.22-0.52mm of longitudinal growth across the physis has been found to precede fusion (Gunderson et al. 2013). These studies indicate the level of clinical significance of both paediatric models: scoliosis and leg length discrepancy, is near the accuracy afforded by the EOS RSA technique. In the adult realm, there has been widespread demonstration of the utility of the RSA technique in assessing post-surgical implant stability (Valstar et al. 2002; Kärrholm et al. 1997). The accuracy afforded by this technique is near the threshold indicated in prominent orthopaedic models employing RSA: 0.2mm is the accuracy threshold in the TKA model (Ryd et al. 1995) while prosthesis subsidence of 0.33mm is indicative of an increased risk of revision in THA (Kärrholm et al. 1994).

Concluding Remarks

The EOS imager has redefined the ALARA principle in paediatric orthopaedics. RSA has demonstrated its utility in post-surgical prosthesis stability assessment. The results of this thesis suggest that the RSA technique employed in the EOS modality offers high accuracy with reduced radiation dose. The EOS RSA technique has the potential to foster widespread implementation of RSA technique in the paediatric research realm. Future research should endeavour to characterize the clinical utility of this technique for paediatric orthopaedic conditions including scoliosis and SCFE.

Bibliography

Alberius, P., 1983. Bone reactions to tantalum markers. A scanning electron microscopic study. *Acta anatomica*, 115(4), pp.310–8.

Ashmore, A.M. et al., 2012. A new technique for the radiostereometric analysis of soft tissues. *Journal of biomechanics*, 45(16), pp.2931–4.

Barbadoro, P. et al., 2014. Tibial component alignment and risk of loosening in unicompartmental knee arthroplasty: a radiographic and radiostereometric study. *Knee surgery, sports traumatology, arthroscopy : official journal of the ESSKA*.

Bland, J.M. & Altman, D.G., 1986. Statistical methods for assessing agreement between two methods of clinical measurement. *Lancet*, 1(8476), pp.307–10.

Bojan, A.J. et al., 2015. Three-dimensional bone-implant movements in trochanteric hip fractures: Precision and accuracy of radiostereometric analysis in a phantom model. *Journal of orthopaedic research : official publication of the Orthopaedic Research Society*.

Borlin, N., 2000. *Model-based Measurements in Digital Radiographs*. Umeå University.

Bottner, F. et al., 2005. Radiostereometric analysis: the hip. *HSS journal : the musculoskeletal journal of Hospital for Special Surgery*, 1(1), pp.94–9.

Bragdon, C.R. et al., 2002. Experimental assessment of precision and accuracy of radiostereometric analysis for the determination of polyethylene wear in a total hip replacement model. *Journal of orthopaedic research : official publication of the Orthopaedic Research Society*, 20(4), pp.688–95.

Bragdon, C.R. et al., 2006. Standing versus Supine Radiographs in RSA Evaluation of Femoral Head Penetration. , (448), pp.46–51.

Briechle, K. & Hanebeck, U.D., 2001. Template matching using fast normalized cross correlation. In D. P. Casasent & T.-H. Chao, eds. *Aerospace/Defense Sensing, Simulation, and Controls*. International Society for Optics and Photonics, pp. 95–102.

Cai, R. et al., 2008. Development of an RSA calibration system with improved accuracy and precision. *Journal of biomechanics*, 41(4), pp.907–11.

Challis, J.H., 1995. A procedure for determining rigid body transformation parameters. *Journal of biomechanics*, 28(6), pp.733–7.

Clohisy, J.C. et al., 2007. The frog-leg lateral radiograph accurately visualized hip cam impingement abnormalities. *Clinical orthopaedics and related research*, 462, pp.115–21.

Delin, C. et al., 2014. Ionizing radiation doses during lower limb torsion and anteversion

measurements by EOS stereoradiography and computed tomography. *European journal of radiology*, 83(2), pp.371–7.

Deschênes, S. et al., 2010. Diagnostic imaging of spinal deformities: reducing patients radiation dose with a new slot-scanning X-ray imager. *Spine*, 35(9), pp.989–94.

Duda, R.O. & Hart, P.E., 1972. Use of the Hough transformation to detect lines and curves in pictures. *Communications of the ACM*, 15(1), pp.11–15.

Dujovne, A.R., Fassier, F. & Gladevitch, M., 2014. Cannulated telescopic femoral neck screw device and related fixation method.

Dunbar, M.J. et al., 2009. Fixation of a trabecular metal knee arthroplasty component. A prospective randomized study. *The Journal of bone and joint surgery. American volume*, 91(7), pp.1578–86.

Edmondson, M. et al., 2014. Prospective randomised clinical trial assessing subsidence and rotation, using radiostereometric analysis, of two modular cementless femoral stems (Global K2 and Apex). *Journal of orthopaedics*, 11(2), pp.96–102.

Engelsma, Y. et al., 2012. Progressive slip after removal of screw fixation in slipped capital femoral epiphysis: two case reports. *Journal of medical case reports*, 6(1), p.405.

Folinais, D. et al., 2013. Measuring femoral and rotational alignment: EOS system versus computed tomography. *Orthopaedics & traumatology, surgery & research : OTSR*, 99(5), pp.509–16.

Gascoyne, T.C., Morrison, J.B. & Turgeon, T.R., 2014. The effect of patient positioning on the precision of model-based radiostereometric analysis. *Journal of biomechanics*, 47(8), pp.1914–7.

Glyn-Jones, S. et al., 2006. RSA-measured inducible micromotion and interface modeling with finite element methods. *Clinical orthopaedics and related research*, 448, pp.98–104.

Green, D.L. et al., 1983. Biplane radiographic measurements of reversible displacement (including clinical loosening) and migration of total joint replacements. *The Journal of bone and joint surgery. American volume*, 65(8), pp.1134–43.

Guenoun, B. et al., 2014. Reliability of a New Method for Evaluating Femoral Stem Positioning After Total Hip Arthroplasty Based on Stereoradiographic 3D Reconstruction. *The Journal of arthroplasty*.

Gunderson, R.B. et al., 2013. Negative correlation between extent of physeal ablation after percutaneous permanent physiodesis and postoperative growth: volume computer tomography and radiostereometric analysis of 37 physes in 27 patients. *Acta orthopaedica*, 84(4), pp.426–30.

Hägglund, G. et al., 1986. Longitudinal growth of the distal fibula in children with slipped capital femoral epiphysis. *Journal of pediatric orthopedics*, 6(3), pp.274–7.

Horn, J. et al., 2013. Percutaneous epiphysiodesis in the proximal tibia by a single-portal approach: evaluation by radiostereometric analysis. *Journal of children's orthopaedics*, 7(4), pp.295–300.

Ioppolo, J. et al., 2007. Validation of a low-dose hybrid RSA and fluoroscopy technique: Determination of accuracy, bias and precision. *Journal of biomechanics*, 40(3), pp.686–92.

ISO 16087:2013(E). Implants for surgery — Roentgen stereophotogrammetric analysis for the assessment of migration of orthopaedic implants.

Jurie, F. & Dhome, M., 2002. Real Time Robust Template Matching. *Bmvc*, pp.1–10.

Kaptein, B.L. et al., 2003. A new model-based RSA method validated using CAD models and models from reversed engineering. *Journal of Biomechanics*, 36(6), pp.873–882.

Karrholm, J. et al., 1994. Does early micromotion of femoral stem prostheses matter? 4-7-year stereoradiographic follow-up of 84 cemented prostheses. *J Bone Joint Surg Br*, 76-B(6), pp.912–917.

Kärrholm, J. et al., 1997. Radiostereometry of hip prostheses. Review of methodology and clinical results. *Clinical orthopaedics and related research*, (344), pp.94–110.

Kärrholm, J., Hansson, L.I. & Selvik, G., 1984. Longitudinal growth rate of the distal tibia and fibula in children. *Clinical orthopaedics and related research*, (191), pp.121–8.

Kedgley, A.E., Birmingham, T. & Jenkyn, T.R., 2009. Comparative accuracy of radiostereometric and optical tracking systems. *Journal of biomechanics*, 42(9), pp.1350–4.

Kendrick, B.J.L. et al., 2015. Cemented versus cementless Oxford unicompartmental knee arthroplasty using radiostereometric analysis: A randomised controlled trial. *The bone & joint journal*, 97-B(2), pp.185–91.

Khoury, J.G. et al., 2007. Results of screw epiphysiodesis for the treatment of limb length discrepancy and angular deformity. *Journal of pediatric orthopedics*, 27(6), pp.623–8.

Kocher, M.S. et al., 2004. Prophylactic pinning of the contralateral hip after unilateral slipped capital femoral epiphysis. *The Journal of bone and joint surgery. American volume*, 86-A(12), pp.2658–65.

Krouwer, J.S., 2008. Why Bland-Altman plots should use X, not (Y+X)/2 when X is a reference method. *Statistics in medicine*, 27(5), pp.778–80.

Laende, E.K. et al., 2009. Implementation and validation of an implant-based coordinate system for RSA migration calculation. *Journal of biomechanics*, 42(14), pp.2387–93.

Lazennec, J.Y. et al., 2011. Pelvis and total hip arthroplasty acetabular component orientations in sitting and standing positions: Measurements reproductibility with EOS imaging system versus conventional radiographies.

Li, Y. et al., 2014. Comparison of two different Radiostereometric analysis (RSA) systems with markerless elementary geometrical shape modeling for the measurement of stem migration. *Clinical biomechanics (Bristol, Avon)*.

Lloyd-Roberts, G.C. & Ratliff, A.H.C., 2013. *Hip Disorders in Children: Postgraduate Orthopaedics Series*, Elsevier Science.

Loder, R.T. et al., 1993. Acute slipped capital femoral epiphysis: the importance of physeal stability. *The Journal of bone and joint surgery. American volume*, 75(8), pp.1134–40.

Loder, R.T., 1996. The demographics of slipped capital femoral epiphysis. An international multicenter study. *Clinical orthopaedics and related research*, (322), pp.8–27.

Loder, R.T. & Skopelja, E.N., 2011. The epidemiology and demographics of slipped capital femoral epiphysis. *ISRN orthopedics*, 2011, p.486512.

Lorenzen, N.D. et al., 2013. Marker-based or model-based RSA for evaluation of hip resurfacing arthroplasty? A clinical validation and 5-year follow-up. *Archives of orthopaedic and trauma surgery*, 133(11), pp.1613–21.

Madanat, R. et al., 2005. Accuracy and precision of radiostereometric analysis in the measurement of three-dimensional micromotion in a fracture model of the distal radius. *Journal of orthopaedic research : official publication of the Orthopaedic Research Society*, 23(2), pp.481–8.

Madanat, R., Moritz, N. & Aro, H.T., 2007. Three-dimensional computer simulation of radiostereometric analysis (RSA) in distal radius fractures. *Journal of biomechanics*, 40(8), pp.1855–61.

Mjöberg, B., 1997. The theory of early loosening of hip prostheses. *Orthopedics*, 20(12), pp.1169–75.

Mjöberg, B., Hansson, L.I. & Selvik, G., 1984. Instability, migration and laxity of total hip prostheses. A roentgen stereophotogrammetric study. *Acta orthopaedica Scandinavica*, 55(2), pp.141–5.

Moreland, J.R., Bassett, L.W. & Hanker, G.J., 1987. Radiographic analysis of the axial alignment of the lower extremity. *The Journal of bone and joint surgery. American volume*, 69(5), pp.745–9.

Murphy, R.F. et al., 2013. Implant Failure in Slipped Capital Femoral Epiphysis. , pp.1–6.

Nebergall, A.K. et al., 2015. Precision of radiostereometric analysis (RSA) of acetabular cup stability and polyethylene wear improved by adding tantalum beads to the liner. *Acta orthopaedica*, 86(5), pp.563–8.

Nuttall, D., Haines, J.F. & Trail, I.A., 2012. The early migration of a partially cemented fluted pegged glenoid component using radiostereometric analysis. *Journal of shoulder and elbow surgery / American Shoulder and Elbow Surgeons ... [et al.]*, 21(9), pp.1191–6.

Onsten, I. et al., 2001. Accuracy and precision of radiostereometric analysis in the measurement of THR femoral component translations: human and canine in vitro models. *Journal of orthopaedic research : official publication of the Orthopaedic Research Society*, 19(6), pp.1162–7.

Ordeberg, G., Hansson, L.I. & Sandström, S., 1987. Slipped capital femoral epiphysis in southern Sweden. Long-term result with closed reduction and hip plaster spica. *Clinical orthopaedics and related research*, (220), pp.148–54.

Pape, D. et al., 2002. Lumbosacral stability of consolidated anteroposterior fusion after instrumentation removal determined by roentgen stereophotogrammetric analysis and direct surgical exploration. *Spine*, 27(3), pp.269–74.

Pijls, B.G. et al., 2012. Early migration of tibial components is associated with late revision: a systematic review and meta-analysis of 21,000 knee arthroplasties. *Acta orthopaedica*, 83(6), pp.614–24.

Pineau, V. et al., 2010. Dual mobility hip arthroplasty wear measurement: Experimental accuracy assessment using radiostereometric analysis (RSA). *Orthopaedics & traumatology, surgery & research : OTSR*, 96(6), pp.609–15.

Ranstam, J. & Ryd, L., 2000. Erratum – Accurate accuracy assessment. 71(1), pp.106–108.

Riley, P.M. et al., 1990. Hazards of internal fixation in the treatment of slipped capital femoral epiphysis. *The Journal of bone and joint surgery. American volume*, 72(10), pp.1500–9.

Ronckers, C.M. et al., 2010. Cancer mortality among women frequently exposed to radiographic examinations for spinal disorders. *Radiation research*, 174(1), pp.83–90.

Ryd, L. et al., 1995. Roentgen stereophotogrammetric analysis as a predictor of mechanical loosening of knee prostheses. *J Bone Joint Surg Br*, 77-B(3), pp.377–383.

Salemyr, M. et al., 2014. Porous titanium construct cup compared to porous coated titanium cup in total hip arthroplasty. A randomised controlled trial. *International orthopaedics*.

Sankar, W.N. et al., 2010. The unstable slipped capital femoral epiphysis: risk factors for osteonecrosis. *Journal of pediatric orthopedics*, 30(6), pp.544–8.

Sarnäs, K.-V., Aberg, M. & Svensson, H., 2012. Mandibular widening in hemifacial microsomia: a roentgen stereometric study of 11 patients with the aid of metallic implants. *American journal of orthodontics and dentofacial orthopedics,* 141(4 Suppl), pp.S88–91.

Seehaus, F. et al., 2009. Experimental analysis of Model-Based Roentgen Stereophotogrammetric Analysis (MBRSA) on four typical prosthesis components. *Journal of biomechanical engineering*, 131(4), p.041004.

Seehaus, F. et al., 2012. Markerless Roentgen Stereophotogrammetric Analysis for in vivo implant migration measurement using three dimensional surface models to represent bone. *Journal of Biomechanics*, 45(8), pp.1540–1545.

Selby, M.D. et al., 2012. Radiologic assessment of spinal fusion. *The Journal of the American Academy of Orthopaedic Surgeons*, 20(11), pp.694–703.

Selvik, G., 1989. Roentgen stereophotogrammetry. A method for the study of the kinematics of the skeletal system. *Acta orthopaedica Scandinavica. Supplementum*, 232, pp.1–51.

Shapiro, F., 2002. *Pediatric Orthopedic Deformities*, Gulf Professional Publishing.

Solomon, L.B. et al., 2010. The accuracy and precision of radiostereometric analysis in monitoring tibial plateau fractures. *Acta orthopaedica*, 81(4), pp.487–94.

Solomon, L.B. & Callary, S.A., 2011. Emerging ideas: soft tissue applications of radiostereometric analysis. *Clinical orthopaedics and related research*, 469(5), pp.1512–6.

Song, K.M. et al., 2004. Gait abnormalities following slipped capital femoral epiphysis. *Journal of pediatric orthopedics*, 24(2), pp.148–55.

Souder, C.D., Bomar, J.D. & Wenger, D.R., 2014. The Role of Capital Realignment Versus In Situ Stabilization for the Treatment of Slipped Capital Femoral Epiphysis. *Journal of pediatric orthopedics*.

Spurway, A.J., 2012. *Radiostereometric Analysis Origin Styles: Their Impact On The Accuracy And Precision In The Assessment Of Spinal Fusion Success*. Dalhousie University.

Stilling, M. et al., 2012. Superior accuracy of model-based radiostereometric analysis for measurement of polyethylene wear: A phantom study. *Bone & joint research*, 1(8), pp.180–91.

Sutherland, C.J. et al., 1982. A ten-year follow-up of one hundred consecutive Müller curved-stem total hip-replacement arthroplasties. *The Journal of bone and joint surgery. American volume*, 64(7), pp.970–82.

Theivendran, K. & Hart, W.J., 2009. Is the tip of the greater trochanter a reliable reference for the rotation centre of the femoral head in total hip arthroplasty? *Acta orthopaedica Belgica*,

75(4), pp.472–6.

Thomas, G.E.R. et al., 2011. The seven-year wear of highly cross-linked polyethylene in total hip arthroplasty: a double-blind, randomized controlled trial using radiostereometric analysis. *The Journal of bone and joint surgery. American volume*, 93(8), pp.716–22.

Tokmakova, K.P., Stanton, R.P. & Mason, D.E., 2003. Factors influencing the development of osteonecrosis in patients treated for slipped capital femoral epiphysis. *The Journal of bone and joint surgery. American volume*, 85-A(5), pp.798–801.

Trozzi, C. et al., 2008. Precision assessment of model-based RSA for a total knee prosthesis in a biplanar set-up. *The Knee*, 15(5), pp.396–402.

Valstar, E.R. et al., 2000. Digital automated RSA compared to manually operated RSA. , 33, pp.1593–1599.

Valstar, E.R. et al., 2005. Guidelines for standardization of radiostereometry (RSA) of implants. *Acta orthopaedica*, 76(4), pp.563–72.

Valstar, E.R. et al., 2002. The use of Roentgen stereophotogrammetry to study micromotion of orthopaedic implants. *ISPRS Journal of Photogrammetry and Remote Sensing*, 56(5-6), pp.376–389.

Vrooman, H. a. et al., 1998. Fast and accurate automated measurements in digitized stereophotogrammetric radiographs. *Journal of Biomechanics*, 31(5), pp.491–498.

Walter, R.P., Jeffery, R.S. & Holroyd, B., 2013. Bilateral epiphyseal migration following fixation for slipped capital femoral epiphyses in a hypothyroid child. *Acta orthopaedica Belgica*, 79(2), pp.235–8.

Wensaas, A., Svenningsen, S. & Terjesen, T., 2011. Long-term outcome of slipped capital femoral epiphysis: a 38-year follow-up of 66 patients. *Journal of children's orthopaedics*, 5(2), pp.75–82.

Wheeless, C., 2011. Duke orthopedics: Wheeless' textbook of orthopaedics.

Wilson, D., 2007. *Radiostereometric Analysis Of Migration And Inducible Displacement Of A Novel Porous Biomaterial Used In Total Knee Arthroplasty*. Dalhousie University.

Wilson, D.A.J. et al., 2012. Continued stabilization of trabecular metal tibial monoblock total knee arthroplasty components at 5 years-measured with radiostereometric analysis. *Acta orthopaedica*, 83(1), pp.36–40.

Wilson, D.A.J. et al., 2010. Inducible displacement of a trabecular metal tibial monoblock component. *The Journal of arthroplasty*, 25(6), pp.893–900.

Witbreuk, M. et al., 2013. Slipped capital femoral epiphysis and its association with endocrine, metabolic and chronic diseases : a systematic review of the literature. pp.213–223.

Appendix A - Output from Standard RS Analysis

Appendix A1 - Medial Displacements

Reference Exam [Medial Displacement] (mm)	Migrating Exam [Medial Displacement] (mm)	Translation x (mm) [Medial]	Translation y (mm) [Superior]	Translation z (mm) [Anterior]	Rotation about x (°) [Anterior-Tilt]	Rotation about y (°) [External Rotation]	Rotation about z (°) [Varus Rotation]	#Matched Markers	#Matched Reference Markers	Rigid Body Error (mm)	Rigid Body Error Reference (mm)	Condition Number	Condition Number Reference	Maximum Total Point Motion (mm)
0.00	-0.10	-0.1209	0.0188	-0.0078	0.0564	-0.0268	-0.0333	4	7	0.0112	0.0075	63.4	25.9	0.133
0.00	-0.10	-0.1211	0.0179	-0.0189	0.0227	0.0222	0.008	4	7	0.0061	0.0087	63.7	26	0.1281
0.00	-0.10	-0.1232	0.0125	-0.0111	-0.0809	-0.1813	0.0284	4	7	0.0265	0.0235	63.7	26	0.1474
0.00	-0.25	-0.300	0.0185	-0.0215	0.0167	-0.0299	-0.0067	4	7	0.0103	0.0074	63.4	25.9	0.3068
0.00	-0.25	-0.2532	-0.0078	0.0243	-0.0405	0.0006	0.0371	4	7	0.0066	0.0188	63.7	26	0.3215
0.00	-0.25	-0.2381	-0.0186	0.0279	-0.0456	-0.0135	0.0671	4	7	0.0087	0.0223	63.7	26	0.3487
0.00	-0.50	-0.5309	0.0216	0.0077	0.066	0.0000	-0.0032	4	7	0.0088	0.006	63.4	25.9	0.5378
0.00	-0.50	-0.499	-0.026	0.027	-0.0185	0.0682	0.0697	4	7	0.0097	0.0165	63.7	26	0.5655
0.00	-0.50	-0.4863	-0.0261	0.0463	0.0093	0.0679	0.0452	4	7	0.0069	0.0137	63.7	26	0.5471
0.00	-0.75	-0.7987	-0.0006	0.0411	0.0268	0.044	0.027	4	7	0.0063	0.0184	63.7	26	0.819
0.00	-0.75	-0.7704	0.0057	0.0365	-0.0216	0.0059	-0.0137	4	7	0.015	0.0195	63.7	26	0.7775
0.00	-0.75	-0.7763	-0.0091	0.0264	-0.1031	-0.1027	-0.003	4	7	0.0248	0.0169	63.7	26	0.8174
0.00	-1.00	-1.0015	-0.0033	0.0332	-0.0091	-0.0828	-0.005	4	7	0.0186	0.0176	63.7	26	1.0256
0.00	-1.00	-0.9868	-0.0027	0.0215	-0.0114	0.1056	0.0614	4	7	0.0195	0.0138	63.7	26	1.008
0.00	-1.00	-0.9954	-0.0033	0.0159	0.072	0.0677	0.0395	4	6	0.0121	0.0157	63.7	27.9	1.0079
0.00	-1.50	-1.5113	0.0058	0.0089	0.0421	0.0397	0.0544	4	7	0.0113	0.0143	63.7	26	1.537
0.00	-1.50	-1.4986	0.0006	-0.0015	0.0562	0.0741	0.0952	4	7	0.0182	0.0162	63.7	26	1.5056
0.00	-1.50	-1.4973	0.0135	0.0036	0.0146	0.0289	0.0331	4	7	0.0071	0.0129	63.7	26	1.5092
0.00	-2.00	-2.0106	0.0191	0.022	0.0492	0.0185	0.0419	4	7	0.0046	0.0214	63.7	26	2.0378
0.00	-2.00	-2.0190	0.0256	0.0184	0.0104	-0.0845	0.0188	4	7	0.0027	0.0142	63.7	26	2.0468
0.00	-2.00	-1.9856	0.0118	0.0519	-0.083	-0.1275	-0.0116	4	7	0.0156	0.0208	63.7	26	2.0371

Appendix A2 - Superior Displacements

Reference Exam [Superior Displacement] (mm)	Migrating Exam [Superior Displacement] (mm)	Translation x (mm) [Medial]	Translation y (mm) [Superior]	Translation z (mm) [Anterior]	Rotation about x (°) [Anterior-Tilt]	Rotation about y (°) [External Rotation]	Rotation about z (°) [Varus Rotation]	#Matched Markers	#Matched Reference Markers	Rigid Body Error (mm)	Rigid Body Error Reference (mm)	Condition Number	Condition Number Reference	Maximum Total Point Motion (mm)
0.00	0.10	0.0065	0.0911	-0.0026	-0.0153	-0.073	0.0003	4	7	0.0059	0.016	62.8	26	0.0941
0.00	0.10	0.0195	0.0988	-0.0037	0.0002	0.0296	0.0092	4	7	0.0054	0.0095	63.1	26	0.1059
0.00	0.10	0.0094	0.1014	-0.0149	0.159	0.2119	0.0498	4	7	0.0327	0.0131	62.8	26	0.1332
0.00	0.25	0.0443	0.2490	-0.0053	0.0167	-0.0741	0.0231	4	7	0.007	0.0236	62.8	26	0.2591
0.00	0.25	-0.0140	0.2503	-0.0064	0.0335	0.0217	0.0241	4	7	0.0064	0.0084	63.1	26	0.2546
0.00	0.25	0.0390	0.2479	-0.0015	0.0389	-0.0427	-0.0244	4	7	0.0112	0.0164	62.8	26	0.2612
0.00	0.50	-0.0244	0.4908	0.0348	-0.0116	-0.0111	-0.0209	4	7	0.0122	0.0143	62.8	26	0.5009
0.00	0.50	0.0260	0.4991	-0.0167	-0.0573	0.0217	0.0159	4	7	0.009	0.0095	63.1	26	0.5059
0.00	0.50	-0.0085	0.5007	0.0258	0.0414	-0.0625	-0.0377	4	7	0.0102	0.0172	62.8	26	0.5192
0.00	0.75	0.0262	0.7435	0.0279	-0.0043	-0.0171	-0.0180	4	7	0.0165	0.0144	62.8	26	0.7600
0.00	0.75	-0.0169	0.7291	0.0187	0.0566	-0.0310	-0.0032	4	7	0.0142	0.0212	62.8	26	0.7486
0.00	0.75	0.0264	0.7675	0.047	0.0564	-0.009	-0.0075	4	7	0.004	0.0172	62.8	26	0.7740
0.00	1.00	-0.0369	0.9769	0.0375	0.0130	-0.0189	0.0283	4	7	0.0072	0.0276	62.8	26	0.9855
0.00	1.00	0.0241	1.0086	-0.0188	-0.0019	0.0239	0.0034	4	7	0.0076	0.009	63.1	26	1.0099
0.00	1.00	0.029	0.9765	0.0384	-0.0209	-0.0708	-0.0299	4	7	0.0155	0.0282	62.8	26	0.9884
0.00	1.50	-0.0226	1.4934	0.0854	-0.0188	-0.0943	-0.0186	4	7	0.0153	0.021	62.8	26	1.5093
0.00	1.50	0.0414	1.4920	0.0755	-0.0237	-0.0415	0.0029	4	7	0.0117	0.0253	62.8	26	1.5082
0.00	1.50	-0.0354	1.4850	0.0828	0.0387	-0.0352	-0.0204	4	7	0.0085	0.0255	62.8	26	1.5012
0.00	2.00	0.0572	1.9713	0.1037	-0.0300	-0.0676	-0.0003	4	7	0.0107	0.0211	62.8	26	1.9800
0.00	2.00	0.0350	2.0098	0.1122	0.1270	-0.0216	0.0253	4	7	0.0149	0.016	62.8	26	2.0265
0.00	2.00	-0.0577	2.0018	0.116	0.1283	0.0425	0.0349	4	7	0.0141	0.0147	62.8	26	2.0181

Appendix A3 - Anterior Displacements

Reference Exam [Anterior Displacement] (mm)	Migrating Exam [Anterior Displacement] (mm)	Translation x (mm) [Medial]	Translation y (mm) [Superior]	Translation z (mm) [Anterior]	Rotation about x (°) [Anterior-Tilt]	Rotation about y (°) [External Rotation]	Rotation about z (°) [Varus Rotation]	#Matched Markers	#Matched Reference Markers	Rigid Body Error (mm)	Rigid Body Error Reference (mm)	Condition Number	Condition Number Reference	Maximum Total Point Motion (mm)
0.00	0.10	0.0048	-0.0163	0.1482	-0.1288	-0.1138	-0.0747	4	6	0.0421	0.037	65.2	27.4	0.234
0.00	0.10	-0.0306	-0.0045	0.0623	-0.015	-0.0063	0.0632	4	7	0.0188	0.0118	64.7	26.1	0.0806
0.00	0.10	-0.0076	0.0193	0.0909	-0.0397	-0.1046	-0.0027	4	7	0.0175	0.011	64.7	26.1	0.1105
0.00	0.25	-0.0243	-0.0091	0.2772	-0.1075	-0.0133	0.0018	4	7	0.0247	0.0300	65.2	25.7	0.3129
0.00	0.25	-0.009	0.0085	0.2903	0.0833	0.1455	0.0549	4	7	0.0175	0.0132	64.7	26.1	0.3257
0.00	0.25	0.0305	0.0134	0.2663	-0.0062	-0.0099	-0.0026	4	7	0.0054	0.0095	63.1	26.0	0.2775
0.00	0.50	0.0452	-0.0193	0.5935	-0.1174	-0.1333	-0.0681	4	7	0.027	0.0238	65.2	25.7	0.6354
0.00	0.50	-0.0017	0.0017	0.5326	-0.0729	0.0316	0.0127	4	7	0.0076	0.0104	64.7	26.1	0.5506
0.00	0.50	-0.0203	-0.0082	0.5247	0.0296	0.0552	0.0219	4	7	0.0169	0.0131	64.7	26.1	0.5416
0.00	0.75	0.0076	0.0224	0.7641	0.0236	-0.0012	0.0344	4	7	0.0201	0.013	64.7	26.1	0.7709
0.00	0.75	-0.0034	0.0159	0.7686	-0.0556	-0.0297	0.033	4	7	0.0095	0.0116	64.7	26.1	0.7827
0.00	0.75	0.0084	0.009	0.7711	-0.0613	-0.0642	-0.0065	4	7	0.0122	0.0081	64.7	26.1	0.7818
0.00	1.00	0.0044	-0.0237	1.0161	-0.1511	-0.0724	-0.0668	4	7	0.0225	0.0319	65.2	25.7	1.0432
0.00	1.00	0.0122	0.0218	1.0318	0.0016	0.0393	-0.0214	4	7	0.0102	0.0168	64.7	26.1	1.0398
0.00	1.00	0.0078	0.0164	1.0517	-0.1382	-0.0869	-0.0123	4	7	0.0148	0.0146	64.7	26.1	1.0782
0.00	1.50	-0.0131	0.0522	1.5319	-0.052	0.0229	0.039	4	7	0.0088	0.0131	64.7	26.1	1.5404
0.00	1.50	-0.0036	0.0515	1.5335	-0.0135	0.0287	-0.0179	4	7	0.0116	0.0146	64.7	26.1	1.5476
0.00	1.50	0.0382	0.021	1.4928	-0.5401	0.0996	0.1544	4	7	0.0781	0.0157	64.7	26.1	1.5625
0.00	2.00	-0.0038	0.0665	2.0238	-0.022	0.0108	0.0144	4	7	0.0063	0.0163	64.7	26.1	2.0343
0.00	2.00	0.0013	0.0512	2.0289	-0.0474	-0.0131	-0.0084	4	7	0.0091	0.0117	64.7	26.1	2.0449
0.00	2.00	0.0008	0.0558	2.0243	-0.0141	0.015	0.0088	4	7	0.0164	0.0093	64.7	26.1	2.0408

Appendix A4 - Anterior-Tilt Rotation

Reference Exam Anterior-Tilt Rotation (°)	Migrating Exam Anterior-Tilt Rotation (°)	Translation x (mm) [Medial]	Translation y (mm) [Superior]	Translation z (mm) [Anterior]	Rotation about x (°) [Anterior-Tilt]	Rotation about y (°) [External Rotation]	Rotation about z (°) [Varus Rotation]	#Matched Markers	#Matched Reference Markers	Rigid Body Error (mm)	Rigid Body Error Reference (mm)	Condition Number	Condition Number Reference	Maximum Total Point Motion (mm)
0.00	0.17	0.000	-0.0323	0.2629	0.1324	0.0446	0.0123	4	7	0.0071	0.0083	58.9	25.4	0.2876
0.00	0.33	-0.004	-0.0728	0.5729	0.291	0.0094	-0.0128	4	7	0.0067	0.008	58.9	25.4	0.6254
0.00	0.50	0.0025	-0.1242	1.0011	0.5196	-0.0166	-0.0358	4	7	0.0094	0.0095	58.9	25.4	1.0918
0.00	1.00	0.0135	-0.2559	2.0392	0.9754	0.0335	-0.028	4	7	0.0121	0.008	58.9	25.4	2.2084
0.00	2.00	0.0344	-0.538	4.0851	1.9125	0.0086	-0.0184	4	7	0.0053	0.0129	58.9	25.4	4.4224
0.00	4.00	0.0782	-1.2382	8.3673	4.0004	-0.0095	-0.0452	4	7	0.0128	0.0118	58.9	25.4	9.092

Appendix A5 - External Rotation

Reference Exam External Rotation (°)	Migrating Exam External Rotation (°)	Translation x (mm) [Medial]	Translation y (mm) [Superior]	Translation z (mm) [Anterior]	Rotation about x (°) [Anterior-Tilt]	Rotation about y (°) [External Rotation]	Rotation about z (°) [Varus Rotation]	#Matched Markers	#Matched Reference Markers	Rigid Body Error (mm)	Rigid Body Error Reference (mm)	Condition Number	Condition Number Reference	Maximum Total Point Motion (mm)
0.00	0.17	0.0262	0.0016	0.121	-0.021	0.1081	0.028	4	7	0.0109	0.0174	61.7	24.9	0.1476
0.00	0.33	0.0866	-0.0189	0.3221	0.0083	0.3289	0.0462	4	7	0.0091	0.016	61.7	24.9	0.3775
0.00	0.50	0.1242	-0.0263	0.4835	-0.0481	0.4216	0.0626	4	7	0.0081	0.0229	61.7	24.9	0.5648
0.00	1.00	0.2225	-0.0361	0.9524	-0.0249	0.9264	0.0992	4	7	0.0112	0.0217	61.7	24.9	1.1116
0.00	2.00	0.4352	-0.1091	1.9781	0.0882	1.9857	0.173	4	7	0.0124	0.0255	61.7	24.9	2.2926
0.00	4.00	0.7878	-0.2748	3.9866	0.1031	3.9296	0.3337	4	7	0.0092	0.0305	61.7	24.9	4.6068

Appendix A6 - Varus Rotation

Reference Exam Varus Rotation (°)	Migrating Exam Varus Rotation (°)	Translation x (mm) [Medial]	Translation y (mm) [Superior]	Translation z (mm) [Anterior]	Rotation about x (°) [Anterior-Tilt]	Rotation about y (°) [External Rotation]	Rotation about z (°) [Varus Rotation]	#Matched Markers	#Matched Reference Markers	Rigid Body Error (mm)	Rigid Body Error Reference (mm)	Condition Number	Condition Number Reference	Maximum Total Point Motion (mm)
0.00	-0.17	-0.1627	-0.0928	0.003	-0.0158	-0.0215	-0.1035	4	7	0.0044	0.0076	62.3	26.4	0.2033
0.00	-0.33	-0.3913	-0.2456	-0.0252	-0.0054	-0.0396	-0.2694	4	7	0.0081	0.0071	62.3	26.4	0.5008
0.00	-0.50	-0.6834	-0.4342	-0.0487	-0.0491	-0.0598	-0.46	4	7	0.0054	0.0074	62.3	26.4	0.8807
0.00	-1.00	-1.4009	-0.8846	-0.0901	-0.0409	-0.0759	-0.9258	4	7	0.0056	0.01	62.3	26.4	1.7916
0.00	-2.00	-2.8612	-1.8329	-0.2168	-0.1406	-0.1943	-1.8624	4	7	0.0308	0.0128	62.3	26.4	3.6847
0.00	-4.00	-5.7705	-3.8047	-0.5425	-0.024	-0.4937	-3.9233	4	7	0.0875	0.0165	62.3	26.4	7.5317

Appendix A7 - Precision

Test i - Aligned Phantom Pose at isocenter

Reference Exam	Migrating Exam	Translation x (mm) [Medial]	Translation y (mm) [Superior]	Translation z (mm) [Anterior]	Rotation about x (°) [Anterior-Tilt]	Rotation about y (°) [External Rotation]	Rotation about z (°) [Varus Rotation]	#Matched Reference Markers	#Matched Reference Markers	Rigid Body Error (mm)	Rigid Body Error Reference (mm)	Condition Number	Condition Number Reference	Maximum Total Point Motion (mm)
RSA exam 1	RSA exam 2	0.0295	-0.0276	0.0195	0.2086	0.1257	-0.0215	4	7	0.0482	0.0221	66.9	26.1	0.1441
RSA exam 2	RSA exam 3	-0.0272	-0.0078	-0.0119	-0.1875	-0.0837	0.0289	4	7	0.0372	0.0104	65.1	26.1	0.1097
RSA exam 3	RSA exam 4	0.0176	-0.0019	-0.0063	0.1255	0.123	-0.0138	4	7	0.0251	0.0115	64	26	0.0669
RSA exam 4	RSA exam 5	-0.0233	0.0143	0.0043	-0.1572	-0.1433	0.0225	4	7	0.0257	0.0125	64.5	26	0.0767
RSA exam 5	RSA exam 6	0.0035	-0.0068	-0.0001	0.0099	0.0441	-0.0072	4	7	0.0148	0.0113	63.6	25.9	0.0262
RSA exam 6	RSA exam 7	0.021	0.0013	-0.003	0.0062	-0.0449	0.0088	4	7	0.0164	0.0096	63.2	25.9	0.0325
RSA exam 7	RSA exam 1	-0.0131	-0.0003	-0.0016	-0.0071	-0.0317	-0.053	4	7	0.0102	0.0094	64.5	26	0.0284

Test ii - Aligned Phantom Pose displaced by ±10 cm

Reference Exam	Migrating Exam	Translation x (mm) [Medial]	Translation y (mm) [Superior]	Translation z (mm) [Anterior]	Rotation about x (°) [Anterior-Tilt]	Rotation about y (°) [External Rotation]	Rotation about z (°) [Varus Rotation]	#Matched Reference Markers	#Matched Reference Markers	Rigid Body Error (mm)	Rigid Body Error Reference (mm)	Condition Number	Condition Number Reference	Maximum Total Point Motion (mm)
RSA exam 1	RSA exam 2	-0.0018	-0.076	-0.0500	-0.0563	0.0713	0.0973	4	7	0.0159	0.0473	68.4	26.4	0.1015
RSA exam 2	RSA exam 3	0.0116	-0.0065	-0.0158	-0.0851	-0.0778	-0.0439	4	7	0.0091	0.0177	64.2	26.1	0.0361
RSA exam 3	RSA exam 4	0.0735	-0.0716	0.0400	0.1388	-0.0049	0.0134	4	7	0.0266	0.0177	59.4	25.8	0.1278
RSA exam 4	RSA exam 5	-0.0757	0.1140	0.0065	0.0200	-0.0121	0.0508	4	7	0.0105	0.0169	66.2	26.2	0.1537
RSA exam 5	RSA exam 6	0.0332	-0.0735	-0.0059	-0.3318	-0.1296	-0.0426	4	7	0.0451	0.0384	60.4	25.9	0.1277
RSA exam 6	RSA exam 7	-0.0223	0.0320	-0.0387	0.2179	0.1108	-0.0552	4	7	0.0349	0.0317	66.2	26.3	0.1133
RSA exam 7	RSA exam 1	0.0034	0.0669	-0.0229	0.0203	0.0472	0.0232	4	7	0.0098	0.0184	64.5	26.3	0.0828

Test iii - Phantom Pose rotated by ±15° at isocenter

Reference Exam	Migrating Exam	Translation x (mm) [Medial]	Translation y (mm) [Superior]	Translation z (mm) [Anterior]	Rotation about x (°) [Anterior-Tilt]	Rotation about y (°) [External Rotation]	Rotation about z (°) [Varus Rotation]	#Matched Reference Markers	#Matched Reference Markers	Rigid Body Error (mm)	Rigid Body Error Reference (mm)	Condition Number	Condition Number Reference	Maximum Total Point Motion (mm)
RSA exam 1	RSA exam 2	0.0307	0.0259	0.0133	-0.2099	-0.0262	-0.0546	4	7	0.0317	0.0174	63	26.1	0.0654
RSA exam 2	RSA exam 3	-0.0275	-0.0078	-0.0332	-0.0896	0.0239	0.0001	4	7	0.0146	0.0117	65.2	26.2	0.0612
RSA exam 3	RSA exam 4	-0.0744	0.1435	0.0225	-0.0599	-0.0666	0.0056	4	7	0.0248	0.0116	59.3	26.1	0.1874
RSA exam 4	RSA exam 5	-0.0309	0.3374	0.0266	0.1359	0.0951	0.0109	4	7	0.017	0.014	55.1	25.4	0.3532
RSA exam 5	RSA exam 6	0.0731	-0.1325	0.0035	0.0195	-0.0789	-0.0282	4	7	0.0124	0.0171	68.2	26.6	0.1665
RSA exam 6	RSA exam 7	0.0223	0.2912	0.2486	-0.1278	-0.2465	0.0758	4	7	0.0086	0.013	64.6	26.1	0.4353
RSA exam 7	RSA exam 8	-0.023	0.2292	0.1166	0.2277	0.2415	-0.0431	4	7	0.0555	0.027	63.5	26.3	0.5629
RSA exam 8	RSA exam 1	0.0098	0.1633	0.2217	0.0946	0.1289	0.0447	4	7	0.0523	0.0259	63.2	26.1	0.4084

Test vi - Phantom Pose rotated by ±15° and displaced by ±10 cm

Reference Exam	Migrating Exam	Translation x (mm) [Medial]	Translation y (mm) [Superior]	Translation z (mm) [Anterior]	Rotation about x (°) [Anterior-Tilt]	Rotation about y (°) [External Rotation]	Rotation about z (°) [Varus Rotation]	#Matched Reference Markers	#Matched Reference Markers	Rigid Body Error (mm)	Rigid Body Error Reference (mm)	Condition Number	Condition Number Reference	Maximum Total Point Motion (mm)
RSA exam 1	RSA exam 2	0.0783	-0.2012	0.0394	0.0091	0.0955	0.001	4	7	0.0071	0.0148	60.1	26.8	0.2212
RSA exam 2	RSA exam 3	-0.1634	0.0601	-0.0727	0.0347	-0.0665	0.0466	4	7	0.0133	0.0202	64	26.1	0.1938
RSA exam 3	RSA exam 4	-0.0452	-0.1979	0.0738	0.3171	0.1781	-0.0633	4	7	0.024	0.0396	56.5	25.7	0.2368
RSA exam 4	RSA exam 5	0.0464	0.0052	-0.0918	-0.2577	-0.2069	0.0966	4	7	0.0254	0.0396	59.8	25.9	0.1312
RSA exam 5	RSA exam 6	-0.02	0.13561	0.1125	-0.0861	-0.0146	0.004	4	7	0.0082	0.0145	63.8	26.3	0.5784
RSA exam 6	RSA exam 7	-0.0328	0.0528	0.0442	-0.0974	0.1638	-0.0619	4	7	0.0457	0.0162	67.1	26.6	0.1414
RSA exam 7	RSA exam 8	-0.0366	-0.0268	-0.0657	0.1037	-0.1686	-0.1814	4	7	0.0348	0.0469	53.4	26.2	0.1698
RSA exam 8	RSA exam 1	0.0764	-0.2882	0.0039	-0.1056	-0.0818	-0.0138	4	7	0.0152	0.0098	62.9	26.5	0.3096

Appendix B – Output from EOS radiograph analysis

Appendix B1 - Medial Displacements

Reference Exam [Medial Displacement] (mm)	Migrating Exam [Medial Displacement] (mm)	Translation x (mm) [Medial]	Translation y (mm) [Superior]	Translation z (mm) [Anterior]	Rotation about x (°) [Anterior-Tilt]	Rotation about y (°) [External Rotation]	Rotation about z (°) [Varus Rotation]	#Matched Markers in Epiphysis	#Matched Reference Markers in Metaphysis
0.00	-0.10	-0.1028	0.0057	0.0212	-0.0243	0.0026	0.0272	4	7
0.00	-0.10	-0.0833	-0.0081	0.0031	-0.0002	0.0717	-0.0357	4	7
0.00	-0.10	-0.1251	-0.0983	-0.1169	-0.0232	-0.0078	0.0147	4	7
0.00	-0.25	-0.2977	0.0584	-0.1381	0.0348	-0.0088	-0.0074	4	7
0.00	-0.25	-0.2681	-0.0145	-0.0241	0.0061	-0.0789	-0.0032	4	7
0.00	-0.25	-0.2409	-0.0094	-0.0322	0.0475	-0.1064	0.027	4	7
0.00	-0.50	-0.5263	-0.0016	-0.0143	0.0723	-0.0154	0.0076	4	7
0.00	-0.50	-0.5107	0.0027	0.0390	0.0758	0.0722	0.0254	4	7
0.00	-0.50	-0.5226	-0.0215	-0.0996	0.4547	0.214	0.0464	4	7
0.00	-0.75	-0.7810	0.0126	-0.0143	-0.0017	0.0203	-0.0045	4	7
0.00	-0.75	-0.7781	0.0200	-0.0518	0.0933	0.0873	-0.0033	4	7
0.00	-0.75	-0.7794	0.0393	-0.0430	-0.0318	-0.0575	0.0014	4	7
0.00	-1.00	-1.0135	0.0357	-0.0581	-0.0338	-0.0208	-0.0117	4	7
0.00	-1.00	-1.0153	0.0151	-0.0152	-0.0634	0.0217	-0.0376	4	7
0.00	-1.00	1.0096	0.0206	-0.0332	-0.2274	-0.1084	-0.0036	4	7
0.00	-1.50	-1.5218	0.0781	-0.0128	0.1877	0.0669	0.0223	4	7
0.00	-1.50	-1.5059	-0.0983	0.0021	-0.2108	-0.0225	-0.0354	4	7
0.00	-1.50	-1.5306	0.0584	-0.0146	-0.2115	-0.1293	-0.0177	4	7
0.00	-2.00	-2.0106	-0.0215	0.0252	0.0079	0.0197	-0.0116	4	7
0.00	-2.00	-2.0190	0.0357	-0.0028	-0.7034	-0.2031	-0.0974	4	7
0.00	-2.00	-2.0090	0.0677	-0.0029	-0.7208	-0.2606	-0.1377	4	7

Appendix B2 - Superior Displacements

Reference Exam [Superior Displacement] (mm)	Migrating Exam [Superior Displacement] (mm)	Translation x (mm) [Medial]	Translation y (mm) [Superior]	Translation z (mm) [Anterior]	Rotation about x (°) [Anterior-Tilt]	Rotation about y (°) [External Rotation]	Rotation about z (°) [Varus Rotation]	#Matched Markers in Epiphysis	#Matched Reference Markers in Metaphysis
0.00	0.10	-0.0202	0.1125	0.0303	-0.1154	-0.0367	-0.0123	4	7
0.00	0.10	0.0248	0.1068	0.0145	-0.1366	0.0568	-0.0491	4	7
0.00	0.10	0.0219	0.1164	0.0009	0.0665	0.1016	0.0392	4	7
0.00	0.25	-0.0353	0.2650	0.1020	-0.0823	-0.0722	-0.0308	4	7
0.00	0.25	-0.0485	0.2625	-0.0033	-0.0526	0.0714	-0.0786	4	7
0.00	0.25	0.0346	0.276	0.0037	0.1215	0.1521	-0.0179	4	7
0.00	0.50	0.0214	0.5171	0.0195	-0.0110	-0.0891	0.0344	4	7
0.00	0.50	0.0284	0.5377	0.0100	0.1892	0.1479	0.004	4	7
0.00	0.50	-0.0357	0.5054	-0.0047	-0.1352	0.0645	-0.0639	4	7
0.00	0.75	-0.0258	0.7443	0.0066	-0.1159	0.0245	-0.0769	4	7
0.00	0.75	0.005	0.7644	-0.0224	-0.1063	0.0118	-0.0857	4	7
0.00	0.75	-00069	0.7700	-0.0287	0.0108	0.0211	-0.0312	4	7
0.00	1.00	-0.0020	1.0369	-0.0142	-0.0557	-0.0209	-0.056	4	7
0.00	1.00	0.0142	0.9982	-0.019	-0.1728	-0.0064	-0.0416	4	7
0.00	1.00	0.0587	1.0171	0.0324	0.0223	-0.0695	0.0335	4	7
0.00	1.50	0.0359	1.4979	0.0099	0.0034	0.0446	0.0168	4	7
0.00	1.50	-0.0183	1.5051	0.0065	0.1001	0.0593	0.0696	4	7
0.00	1.50	-0.0394	1.4904	-0.0154	-0.3009	-0.0341	-0.0437	4	7
0.00	2.00	0.0043	1.987	-0.0523	-0.3285	-0.0083	-0.0588	4	7
0.00	2.00	0.0093	2.0143	-0.0438	0.0653	0.0669	0.0016	4	7
0.00	2.00	-0.0243	2.0344	-0.0497	-0.0676	0.0289	-0.0649	4	7

Appendix B3 - Anterior Displacements

Reference Exam [Anterior-Displacement] (mm)	Migrating Exam [Anterior-Displacement] (mm)	Translation x (mm) [Medial]	Translation y (mm) [Superior]	Translation z (mm) [Anterior]	Rotation about x (°) [Anterior-Tilt]	Rotation about y (°) [External Rotation]	Rotation about z (°) [Varus Rotation]	#Matched Markers in Epiphysis	#Matched Reference Markers in Metaphysis
0.00	0.10	0.0278	0.0159	0.0885	0.2438	0.0418	0.0629	4	7
0.00	0.10	0.0471	-0.0046	0.059	0.3731	0.1365	0.0129	4	7
0.00	0.10	0.0031	-0.0004	0.087	0.3923	0.2044	-0.0147	4	7
0.00	0.25	0.0879	0.0231	0.2307	0.0638	-0.0601	0.0031	4	7
0.00	0.25	0.0249	-0.0025	0.2435	0.1365	0.1045	0.0015	4	7
0.00	0.25	0.0571	0.0254	0.2442	0.2089	0.0699	0.0265	4	7
0.00	0.50	0.0392	0.0096	0.5393	-0.0114	0.0097	-0.0047	4	7
0.00	0.50	0.0568	0.0348	0.4710	0.6382	0.2799	-0.0208	4	7
0.00	0.50	0.0826	-0.0047	0.4952	0.7440	0.3455	0.1292	4	7
0.00	0.75	0.0614	0.0321	0.7476	0.7189	0.3077	0.043	4	7
0.00	0.75	0.0720	0.0254	0.758	0.5864	0.2402	0.0096	4	7
0.00	0.75	0.0600	0.0594	0.7444	0.6175	0.2398	-0.007	4	7
0.00	1.00	0.0256	0.0075	1.0102	0.4330	0.1544	0.0512	4	7
0.00	1.00	0.0277	0.0608	0.9581	0.7715	0.3455	0.0944	4	7
0.00	1.00	0.0432	0.0245	0.9867	0.6699	0.1668	-0.0019	4	7
0.00	1.50	0.0595	0.0051	1.5023	0.5528	0.3326	0.037	4	7
0.00	1.50	0.0281	0.0236	1.4907	0.5879	0.2247	0.0647	4	7
0.00	1.50	0.0244	-0.0010	1.4802	0.6631	0.2239	0.0972	4	7
0.00	2.00	0.0593	0.0084	1.9751	0.6713	0.2387	0.0946	4	7
0.00	2.00	0.0506	0.0180	1.9757	0.5854	0.3079	0.0367	4	7
0.00	2.00	0.0302	-0.0040	1.9754	0.4508	0.2736	0.0407	4	7

Appendix B4 - Anterior-Tilt Rotation

Reference Exam (Anterior-Tilt rotation) (°)	Migrating Exam [Anterior-Tilt rotation] (°)	Translation x (mm) [Medial]	Translation y (mm) [Superior]	Translation z (mm) [Anterior]	Rotation about x (°) [Anterior-Tilt]	Rotation about y (°) [External Rotation]	Rotation about z (°) [Varus Rotation]	#Matched Markers in Epiphysis	#Matched Reference Markers in Metaphysis
0.00	0.17	0.0323	0.0602	0.3948	0.1245	0.0693	0.0004	4	7
0.00	0.33	0.0345	0.0840	0.6173	0.1665	-0.0173	0.0004	4	7
0.00	0.50	0.0437	0.1758	1.1274	0.4227	0.0536	-0.0127	4	7
0.00	1.00	0.1422	0.3663	2.0757	0.9276	0.0264	-0.0766	4	7
0.00	2.00	0.3101	0.8296	4.3766	2.0021	-0.0670	-0.1330	4	7
0.00	4.00	0.5213	1.8371	8.5893	3.9408	0.0010	-0.2128	4	7

Appendix B5 - External Rotation

Reference Exam (External rotation) (°)	Migrating Exam [External rotation] (°)	Translation x (mm) [Medial]	Translation y (mm) [Superior]	Translation z (mm) [Anterior]	Rotation about x (°) [Anterior-Tilt]	Rotation about y (°) [External Rotation]	Rotation about z (°) [Varus Rotation]	#Matched Markers in Epiphysis	#Matched Reference Markers in Metaphysis
0.00	0.17	0.1189	-0.0056	0.1266	0.0579	0.1130	0.0110	4	7
0.00	0.33	0.2694	-0.0345	0.3195	0.0506	0.4594	0.0511	4	7
0.00	0.50	0.3003	-0.0186	0.4111	0.2049	0.5848	0.0893	4	7
0.00	1.00	0.5503	-0.0315	0.8576	0.2386	1.1599	0.0917	4	7
0.00	2.00	1.0022	-0.0110	1.7514	0.0210	2.0205	0.0379	4	7
0.00	4.00	1.8660	0.0501	3.4909	0.1209	4.0546	0.1106	4	7

Appendix B6 - Varus Rotation

Reference Exam (Varus rotation)	Migrating Exam (Varus rotation)	Translation x (mm) [Medial]	Translation y (mm) [Superior]	Translation z (mm) [Anterior]	Rotation about x (°) [Anterior-Tilt]	Rotation about y (°) [External Rotation]	Rotation about z (°) [Varus Rotation]	#Matched Markers in Epiphysis	#Matched Reference Markers in Metaphysis
0.00	0.17	0.6010	-0.2678	0.0045	-0.0023	0.0154	-0.2610	4	7
0.00	0.33	0.9271	-0.4050	-0.0098	-0.1442	-0.0343	-0.3808	4	7
0.00	0.50	1.2748	-0.5521	0.0257	0.2053	0.1716	-0.5594	4	7
0.00	1.00	2.4030	-1.1259	0.0337	0.1147	0.0985	-1.0887	4	7
0.00	2.00	4.5272	-2.2349	0.0452	-0.0054	0.1130	-2.0833	4	7
0.00	4.00	8.7512	-4.4858	0.1773	0.7811	0.3755	-4.0996	4	7

Appendix B7 - Precision study

Test i – Aligned phantom pose at isocenter

Reference Exam	Migrating Exam	Translation x (mm) [Medial]	Translation y (mm) [Superior]	Translation z (mm) [Anterior]	Rotation about x (°) [Anterior-Tilt]	Rotation about y (°) [External Rotation]	Rotation about z (°) [Varus Rotation]	#Matched Markers in Epiphysis	#Matched Reference Markers in Metaphysis
RSA exam 1	RSA exam 2	0.0157	0.0006	0.0072	0.0785	0.0175	0.0144	4	7
RSA exam 2	RSA exam 3	-0.0319	-0.0003	-0.0121	-0.1347	-0.0671	0.0364	4	7
RSA exam 3	RSA exam 4	-0.0011	0.0048	-0.0019	-0.2571	-0.0313	-0.0821	4	7
RSA exam 4	RSA exam 5	-0.0169	0.002	-0.0242	0.224	-0.1122	-0.0222	4	7
RSA exam 5	RSA exam 6	0.0034	0.0063	0.0291	0.0381	-0.1181	-0.0275	4	7
RSA exam 6	RSA exam 7	0.0007	-0.0184	-0.0538	-0.2186	0.0727	0.0351	4	7
RSA exam 7	RSA exam 1	-0.0037	0.0278	0.0136	0.0375	0.0407	0.0387	4	7

Test ii - Aligned Phantom Pose displaced by ±10 cm

Reference Exam	Migrating Exam	Translation x (mm) [Medial]	Translation y (mm) [Superior]	Translation z (mm) [Anterior]	Rotation about x (°) [Anterior-Tilt]	Rotation about y (°) [External Rotation]	Rotation about z (°) [Varus Rotation]	#Matched Markers in Epiphysis	#Matched Reference Markers in Metaphysis
RSA exam 1	RSA exam 2	0.0852	0.0799	0.0521	-0.2115	0.1660	-0.0736	4	6
RSA exam 2	RSA exam 3	-0.0165	-0.0387	-0.0304	0.0718	-0.0102	0.0512	4	6
RSA exam 3	RSA exam 4	0.0123	0.0145	0.0188	-0.0365	0.0404	-0.0240	4	6
RSA exam 4	RSA exam 5	-0.0969	-0.0534	-0.0284	0.1857	-0.2223	0.0690	4	7
RSA exam 5	RSA exam 6	-0.0098	-0.0964	-0.0232	0.1854	-0.0340	-0.0005	4	6
RSA exam 6	RSA exam 7	0.0344	0.1203	0.0219	-0.2676	0.1481	0.0028	4	6
RSA exam 7	RSA exam 1	0.0395	0.0944	0.0181	-0.1888	0.1225	0.0029	4	6

Test iii - Phantom Pose rotated by ±15° centered in FOV

Reference Exam	Migrating Exam	Translation x (mm) [Medial]	Translation y (mm) [Superior]	Translation z (mm) [Anterior]	Rotation about x (°) [Anterior-Tilt]	Rotation about y (°) [External Rotation]	Rotation about z (°) [Varus Rotation]	#Matched Markers in Epiphysis	#Matched Reference Markers in Metaphysis
RSA exam 1	RSA exam 2	0.0392	0.3705	0.0458	-0.1484	0.2437	-0.0843	4	7
RSA exam 2	RSA exam 3	0.0483	0.0673	0.0035	-0.1230	0.0314	-0.0065	4	7
RSA exam 3	RSA exam 4	0.0655	0.0861	-0.0480	0.0233	-0.0059	0.0469	4	7
RSA exam 4	RSA exam 5	0.0127	-0.3225	-0.0031	0.0028	-0.0678	0.0420	4	7
RSA exam 5	RSA exam 6	-0.1213	-0.0589	0.0472	0.0830	-0.0823	-0.1530	4	7
RSA exam 6	RSA exam 7	-0.0520	-0.0541	-0.1031	0.0954	-0.1046	0.0177	4	7
RSA exam 7	RSA exam 8	0.1007	0.0175	0.0200	-0.1451	0.2058	0.0297	4	7
RSA exam 8	RSA exam 1	0.2595	0.3641	0.0442	-0.1666	0.5196	0.1551	4	7

Test iv - Phantom Pose rotated by ±15° and displaced by ±10 cm

Reference Exam	Migrating Exam	Translation x (mm) [Medial]	Translation y (mm) [Superior]	Translation z (mm) [Anterior]	Rotation about x (°) [Anterior-Tilt]	Rotation about y (°) [External Rotation]	Rotation about z (°) [Varus Rotation]	#Matched Markers in Epiphysis	#Matched Reference Markers in Metaphysis
RSA exam 1	RSA exam 2	-0.0542	-0.0511	0.0067	-0.0570	0.1256	-0.0100	4	7
RSA exam 2	RSA exam 3	0.0390	-0.0002	-0.0072	0.1083	-0.1088	0.0498	4	7
RSA exam 3	RSA exam 4	-0.0485	0.0093	0.0129	0.1607	0.0569	-0.0577	4	7
RSA exam 4	RSA exam 5	0.0578	0.0391	0.0647	-0.1027	0.1301	-0.1133	4	7
RSA exam 5	RSA exam 6	0.2587	0.0600	-0.1448	0.1142	0.0537	-0.0108	4	7
RSA exam 6	RSA exam 7	0.0364	0.2583	0.0595	-0.0388	0.3334	-0.0090	4	7
RSA exam 7	RSA exam 8	-0.0229	0.0267	0.0056	-0.0429	-0.0064	-0.1459	4	7
RSA exam 8	RSA exam 1	-0.2375	-0.3005	0.0057	-0.1154	-0.1290	0.1382	4	7

EOS Detector Extremities

Location A - Left edge of AP detector and Left edge of Lateral detector

Reference Exam	Migrating Exam	Translation x (mm) [Medial]	Translation y (mm) [Superior]	Translation z (mm) [Anterior]	Rotation about x (°) [Anterior-Tilt]	Rotation about y (°) [External Rotation]	Rotation about z (°) [Varus Rotation]	#Matched Markers in Epiphysis	#Matched Reference Markers in Metaphysis
RSA exam 1	RSA exam 2	-0.015	-0.047	-0.031	0.1868	-0.1444	0.0159	4	7
RSA exam 2	RSA exam 3	0.014	0.031	0.025	-0.2229	-0.0345	0.0077	4	7
RSA exam 3	RSA exam 4	-0.0234	-0.0044	0.0976	0.1177	0.0018	-0.0146	4	7
RSA exam 4	RSA exam 5	0.0776	0.0218	-0.0167	-0.2098	0.0873	0.0226	4	7
RSA exam 5	RSA exam 6	-0.0294	-0.0041	0.0352	-0.0526	-0.0605	-0.0075	4	7
RSA exam 6	RSA exam 7	0.0388	-0.0005	-0.0377	0.0125	0.1762	-0.0107	4	7
RSA exam 7	RSA exam 1	-0.017	0.0014	-0.0783	-0.0544	-0.0108	-0.0038	4	7

Location B - Left edge of AP detector and Right edge of Lateral detector

Reference Exam	Migrating Exam	Translation x (mm) [Medial]	Translation y (mm) [Superior]	Translation z (mm) [Anterior]	Rotation about x (°) [Anterior-Tilt]	Rotation about y (°) [External Rotation]	Rotation about z (°) [Varus Rotation]	#Matched Markers in Epiphysis	#Matched Reference Markers in Metaphysis
RSA exam 1	RSA exam 2	0.0237	0.0078	-0.0338	0.0105	-0.0104	-0.0213	4	7
RSA exam 2	RSA exam 3	0.0155	-0.0339	-0.0267	-0.1135	0.1093	0.0037	4	7
RSA exam 3	RSA exam 4	0.0025	-0.0068	0.0230	-0.0875	0.1380	0.0077	4	7
RSA exam 4	RSA exam 5	-0.0229	-0.0445	0.0544	0.0487	0.0666	-0.0003	4	7
RSA exam 5	RSA exam 6	0.0265	0.0263	-0.0145	0.0217	-0.017	0.0071	4	7
RSA exam 6	RSA exam 7	0.0328	-0.0174	-0.0459	0.0297	0.0002	0.0282	4	7
RSA exam 7	RSA exam 1	-0.0267	0.0419	-0.0185	-0.0789	0.0112	-0.0559	4	7

Location C- Right edge of AP beam and Left edge of Lateral detector

Reference Exam	Migrating Exam	Translation x (mm) [Medial]	Translation y (mm) [Superior]	Translation z (mm) [Anterior]	Rotation about x (°) [Anterior-Tilt]	Rotation about y (°) [External Rotation]	Rotation about z (°) [Varus Rotation]	#Matched Markers in Epiphysis	#Matched Reference Markers in Metaphysis
RSA exam 1	RSA exam 2	-0.0391	-0.0497	-0.0089	0.0790	-0.0839	-0.0462	4	7
RSA exam 2	RSA exam 3	0.0342	0.0287	0.0108	-0.1226	0.0920	-0.0565	4	7
RSA exam 3	RSA exam 4	0.0246	-0.0174	-0.0157	0.0872	-0.0109	0.0829	4	7
RSA exam 4	RSA exam 5	-0.0283	0.0125	-0.0065	-0.0384	-0.0884	-0.0168	4	7
RSA exam 5	RSA exam 6	-0.0204	-0.0148	0.0148	0.0006	0.0164	0.0186	4	7
RSA exam 6	RSA exam 7	0.0242	-0.0469	-0.0195	0.1335	0.0586	0.0063	4	7
RSA exam 7	RSA exam 1	0.0017	0.0861	0.0260	-0.1418	0.0144	0.0028	4	7

Location D- Right edge of AP beam and Right edge of Lateral detector

Reference Exam	Migrating Exam	Translation x (mm) [Medial]	Translation y (mm) [Superior]	Translation z (mm) [Anterior]	Rotation about x (°) [Anterior-Tilt]	Rotation about y (°) [External Rotation]	Rotation about z (°) [Varus Rotation]	#Matched Markers in Epiphysis	#Matched Reference Markers in Metaphysis
RSA exam 1	RSA exam 2	0.0259	-0.0197	0.063	-0.1834	-0.0167	-0.0591	4	7
RSA exam 2	RSA exam 3	-0.0205	-0.0126	-0.0113	-0.0891	-0.0086	-0.0059	4	7
RSA exam 3	RSA exam 4	0.0272	0.0261	-0.0397	0.12	-0.0255	0.0059	4	7
RSA exam 4	RSA exam 5	-0.0207	-0.0401	0.0346	-0.0447	-0.0209	0.0268	4	7
RSA exam 5	RSA exam 6	0.0312	0.0465	-0.0565	-0.0398	-0.0628	-0.0755	4	7
RSA exam 6	RSA exam 7	-0.0333	0.0675	0.003	0.0418	0.0642	0.0626	4	7
RSA exam 7	RSA exam 1	0.0971	-0.0688	0.0961	0.0633	0.1022	0.0184	4	7

Centered in Field of View with 45° Vertical axis rotation

Reference Exam	Migrating Exam	Translation x (mm) [Medial]	Translation y (mm) [Superior]	Translation z (mm) [Anterior]	Rotation about x (°) [Anterior-Tilt]	Rotation about y (°) [External Rotation]	Rotation about z (°) [Varus Rotation]	#Matched Markers in Epiphysis	#Matched Reference Markers in Metaphysis
RSA exam 1	RSA exam 2	0.0276	-0.0748	-0.0316	0.0950	0.0430	0.0533	4	7
RSA exam 2	RSA exam 3	-0.0326	0.0605	0.0746	-0.0942	-0.0081	-0.0850	4	7
RSA exam 3	RSA exam 4	-0.0010	-0.0266	-0.0200	0.0968	-0.0617	0.0903	3	7
RSA exam 4	RSA exam 5	0.0274	-0.0226	0.0112	0.0181	0.0877	0.0698	3	7
RSA exam 5	RSA exam 6	0.0293	-0.0167	-0.0355	0.0500	0.0410	0.0049	4	7
RSA exam 6	RSA exam 7	-0.0460	0.0192	0.0102	-0.0375	-0.0664	-0.0450	4	7
RSA exam 7	RSA exam 1	-0.0115	0.0807	-0.0141	-0.1648	-0.0481	-0.0570	4	7

Appendix C - Computer Simulation Exercise

Rationale

There currently exists no RSA bead placement guide for the SCFE femoral head. This study will aim to determine the ideal placement of RSA beads for use in a bi-planar EOS system. The study will foresee and mitigate potential problems relating to bead placement and visibility in the SCFE femoral epiphysis and metaphysis. The results of this study will be used to guide future RSA bead implantation in the SCFE population.

Methods

The computer simulation required the use of several programs during the simulation and analysis of radiographs. Rhinoceros 5 Software (McNeel, Seattle, USA) was used to manipulate the scan file and rotate the CAD (Computer Aided Design) scan in 3D space. Solid Edge ST6 (Siemens, Munich, Germany) was used to transform the scan and apply displacements to the femoral head. Radiographs were simulated in The Persistence of Vision Raytracer (POV-Ray) software (Persistence of Vision Raytracer Pty. Ltd.). Lastly, Radiostereometric Analysis was performed in Model-Based RSA (MBRSA) software 3.41 (RSAcore, Leiden, The Netherlands). An overview of this methodology is presented in Figure C.1.

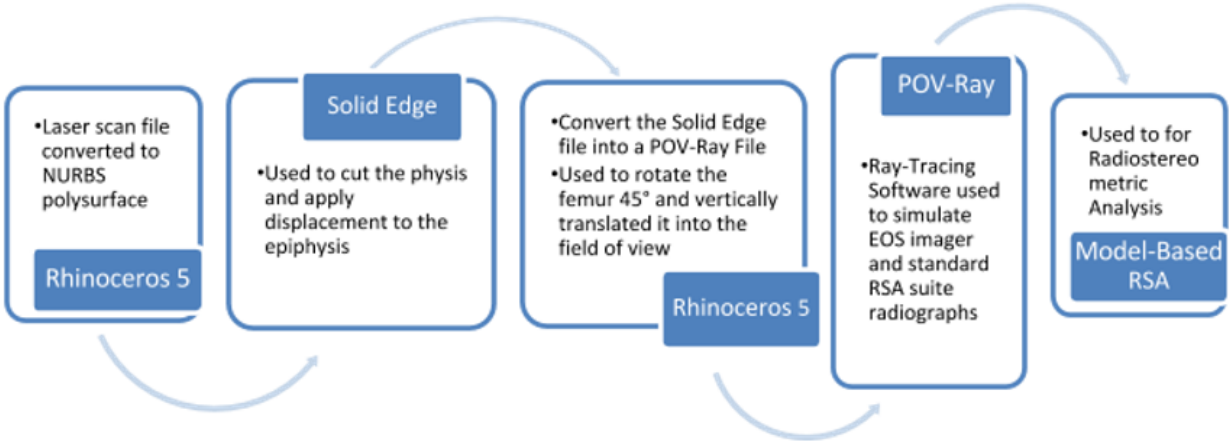

Figure C.1: An overview of the computer simulation process from the laser scan to Radiostereometric Analysis of simulated radiographs.

A SCFE femur phantom model ordered from Sawbones Inc. (Washon Island, USA) catalog number #1161 was laser scanned with a 3D scanner HD (NextEngine Inc., Santa Monica, USA). The femur was sparingly coated with corn starch to decrease shimmer and increase scan

fidelity; the scan quality was set to Medium-High. This setting translated to the femur being scanned for 10,000 points/ in^2 and it required 16 incremental rotations for the 360° scan. The output file was loaded into Rhinoceros 5 and was fixed for mesh holes and incongruities. The number of meshes was reduced to 21,037 to decrease computational load with the ReduceMesh command. Next, the MeshtoNURBS algorithm was run to convert the scan into a NURBS surface. Non-Uniform Rational Basis Spline (NURBS) polysurfaces are mathematical models defined by a series of piece-wise polynomial functions that define a surface in 3 dimensional space. This NURBS surface was then saved as a STP (STandard for the exchange of Product) file for manipulation in Solid Edge ST6, Figure C.2.

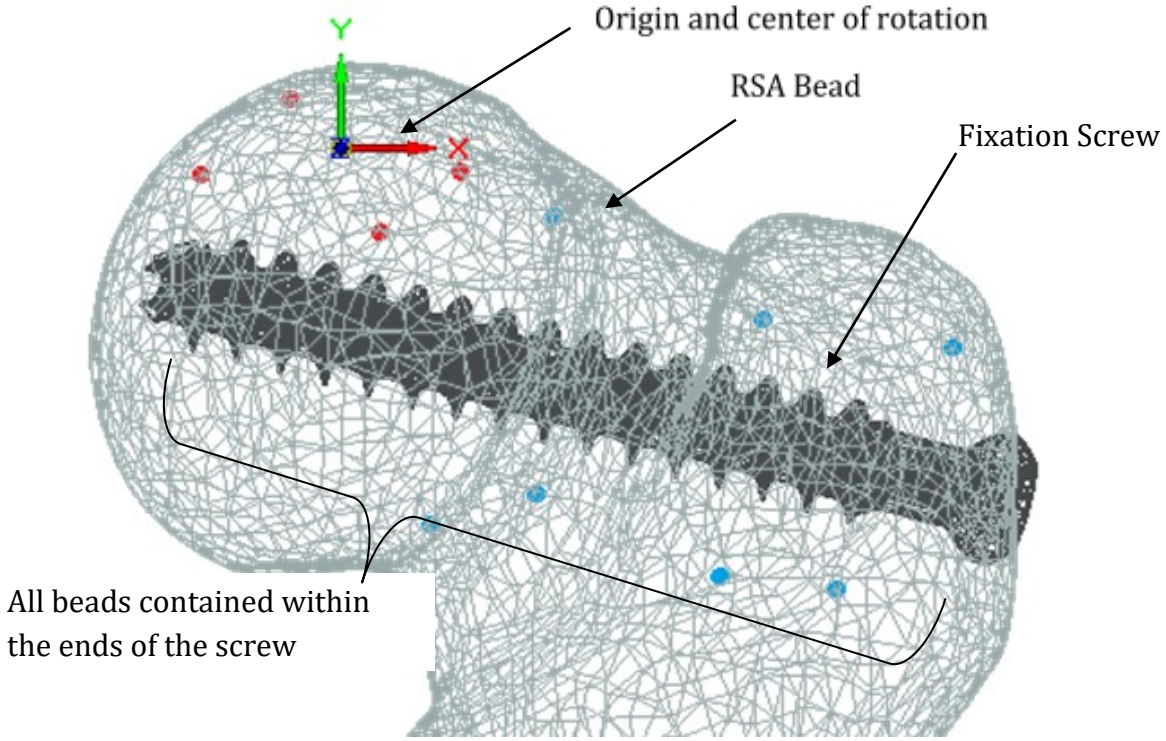

Figure C.2. The Anterio-Posterior view of the computer simulation for the SCFE femur with the 7.3mm cannulated fixation screw, 11 RSA beads and the Origin/Center of Rotation. Red markers and blue markers are epiphyseal and metaphyseal bead clusters, respectively.

Typical SCFE failure method described in the literature are the posterior displacement and internal rotation of the femoral head (Lloyd-Roberts & Ratliff 2013). With the metaphysis as the reference the computer simulation was developed to allow of translations of the epiphysis in the medio-lateral, superio-inferior and anterio-posterior directions corresponding to displacements in the x-, y- and z-axes. Additionally, the simulation was developed to rotate the epiphysis in the following sequential order; anterio-posterior tilt, internal-external rotation and

adduction-abduction corresponding to rotations about the x-, y- and z-axes (ISO 16087:2013). The center of rotation for the femoral head was determined using a horizontal line stretching from the tip of the Greater Trochanter towards the femoral head (Theivendran & Hart 2009). This radiographic method is used in Total Hip Arthroplasty (THA) planning to align the femoral component in an anatomical orientation. The translations and rotations applied to the epiphysis with the metaphysis as the reference body are presented in Tables C.1 and C.2, respectively.

Table C.1. The positive displacements applied to the proximal femoral epiphysis in relation to the femoral shaft in the computer simulation.

Direction of Movement of the epiphysis	Translations in (mm)								
X Plane - Lateral	-0.025	-0.05	-0.1	-0.25	-0.5	-1	-2	-4	-6
Y Plane - Inferior	-0.025	-0.05	-0.1	-0.25	-0.5	-1	-2	-4	-6
Z plane - Posterior	-0.025	-0.05	-0.1	-0.25	-0.5	-1	-2	-4	-6
X Plane - Medial	0.025	0.05	0.1	0.25	0.5	1	2	4	6
Y Plane - Superior	0.025	0.05	0.1	0.25	0.5	1	2	4	6
Z Plane - Anterior	0.025	0.05	0.1	0.25	0.5	1	2	4	6

Table C.2. The positive rotations applied to the proximal femoral epiphysis in relation to the femoral shaft in the computer simulation.

Axis of Rotation / Direction of Movement of the epiphysis	Rotations in degrees (°)					
X axis / Posterior Tilt	-0.17	-0.33	-0.50	-2.00	-5.00	-10.00
Y axis / External rotation	-0.17	-0.33	-0.50	-2.00	-5.00	-10.00
Z axis / Abduction	-0.17	-0.33	-0.50	-2.00	-5.00	-10.00
X axis / Anterior Tilt	0.17	0.33	0.50	2.00	5.00	10.00
Y axis / Internal rotation	0.17	0.33	0.50	2.00	5.00	10.00
Z axis / Adduction	0.17	0.33	0.50	2.00	5.00	10.00

Solid Edge ST6 was used to apply translations and rotations to the epiphysis. With this, the CAD file was loaded into Rhinoceros 5 and the femur was vertically translated +175 mm to bring the femur into the field of view of the simulation. The final orientation of the femur is

presented in Figure D.2. The file was subsequently saved for radiographic simulation in POV-Ray software. POV-Ray is a ray-tracing software which has previously been used to simulate radiographs for RS Analysis. This software has been implemented for the simulated distal radius fracture model (Madanat et al. 2007). Researchers at Dalhousie University and IWK Health Centre have also employed POV-Ray software for RS analysis (A. Spurway, 2012), (A. Francis 2009).

POV-Ray code for the Halifax Infirmary RSA suite, initially written by A. Francis and further developed by A. Spurway, was used to simulate standard RSA suite radiographs. POV-Ray code for the EOS imager, developed by A. Spurway and J. Hurry, was used to simulate EOS radiographs. Radiographs were simulated for both imaging modalities.

The simulated image pairs were loaded into MBRSA Software (RSAcore, Leiden, The Netherlands) to be analyzed for migration. Bead detection algorithms were run with a threshold of 20 and minimum and maximum bead size set to 3 and 6 pixels, respectively. Visual inspection followed to ensure proper detection of beads and the bead detection crosshair were modified in size and location in cases of inaccurate bead detection. Next the beads corresponding to the epiphysis and metaphysis bead clusters were respectively labeled and visual inspection of crossing line distances and the highlighted marker model followed. Using the metaphysis bead cluster as the reference and the epiphysis bead cluster as the migrating, migration calculations were run. The translations and rotations along and about the x-, y-, and z-axes, along with the number of Matched Markers were recorded from the output.

Statistical analysis followed allowing the characterization of the 95% Prediction intervals of observed movements for each nature and planes of movement (Onsten et al. 2001). The 95% Prediction Interval, based on the mean and variance of the sample population, proposes an interval in which 95% of future observations will occur. MATLAB Software was used to determine these intervals.

Bead Cluster Modifications following Primary Analysis

All beads were initially included within 0.5 cm from the cannulation. Bead placement within 0.5cm from the cannulation provided significant bead occlusion at the extremities of the proposed displacements. Therefore, a 1 cm distance from the cannulation was chosen to

minimize: bead occlusion and Condition Number; while simultaneously being in the realm of possibilities in the clinical setting.

Primary analysis also revealed the invariable occlusion of two epiphyseal bead positioned distal to the screw at displacements above 2 mm. This prompted the relocation of those two beads proximal to the screw increasing bead visibility. This configuration Figure C.1 was utilized in all analysis presented in this exercise.

RESULTS

Tables C.3 to C.8 present the applied and observed displacements obtained in the computer simulation. The upper and lower limits of the 95% prediction intervals are also presented. Figures C.3 to C.8 present the graphs for the line of best fits and 95% prediction intervals between the applied and observed displacements in the computer simulation.

Table C.3: The 95% Prediction Intervals of applied and observed Lateral (- x-plane) and Medial (+ x-plane) Displacements to the proximal femoral epiphysis in the computer simulation.

Lateral (-) Medial (+) Displacement of the Epiphysis (X Plane)

Applied Displacement (mm)	Observed Displacement (mm)	95% Prediction interval - Lower limit (mm)	95% Prediction Interval- Upper Limit (mm)	# of matched Markers	# of matched reference Markers
-6.000	-5.967	-6.076	-5.925	3	5
-4.000	-4.010	-4.074	-3.934	3	5
-2.000	-1.986	-2.075	-1.940	4	5
-1.000	-1.022	-1.076	-0.943	4	6
-0.500	-0.510	-0.577	-0.444	4	6
-0.250	-0.272	-0.327	-0.195	4	5
-0.100	-0.111	-0.177	-0.045	4	7
-0.050	-0.032	-0.127	0.005	4	7
-0.025	-0.006	-0.102	0.030	4	7
0.025	0.008	-0.053	0.080	4	7
0.050	0.037	-0.028	0.105	4	7
0.100	0.049	0.022	0.155	4	7
0.250	0.146	0.172	0.305	4	7
0.500	0.494	0.422	0.554	4	7
1.000	0.989	0.921	1.054	4	7
2.000	1.996	1.918	2.053	4	7
4.000	3.988	3.911	4.052	4	7
6.000	6.008	5.903	6.053	4	7

Table C.4: The 95% Prediction Intervals of applied and observed Superior (+ y-plane) and Inferior (- y-plane) Displacements to the proximal femoral epiphysis in the computer simulation.

Superior (+) Inferior (-) Displacement of the Epiphysis (y-plane)

Applied Displacement (mm)	Observed Displacement (mm)	95% Prediction interval - Lower limit (mm)	95% Prediction Interval- Upper Limit (mm)	# of matched Markers	# of matched reference Markers
-6.000	-6.022	-6.098	-5.976	4	7
-4.000	-4.027	-4.090	-3.975	4	7
-2.000	-2.025	-2.083	-1.973	4	7
-1.000	-1.029	-1.080	-0.972	3	7
-0.500	-0.525	-0.579	-0.471	3	7
-0.250	-0.273	-0.328	-0.220	3	7
-0.100	-0.131	-0.178	-0.070	3	7
-0.050	-0.076	-0.128	-0.020	4	7
-0.025	-0.050	-0.103	0.005	4	7
0.025	0.013	-0.052	0.055	4	7
0.050	0.028	-0.027	0.080	4	7
0.100	0.055	0.023	0.130	4	7
0.250	0.147	0.173	0.281	4	7
0.500	0.510	0.424	0.531	4	7
1.000	1.006	0.925	1.033	4	7
2.000	1.988	1.926	2.035	4	7
4.000	3.975	3.928	4.042	4	7
6.000	6.010	5.928	6.051	4	7

Table C.5: The 95% Prediction Intervals of applied and observed Anterior (+ z-plane) and Posterior (- z-plane) Displacements to the proximal femoral epiphysis in the computer simulation.

Anterior (+) Posterior (-) Displacement of the Epiphysis (Z Plane)

Applied Displacement (mm)	Observed Displacement (mm)	95% Prediction interval - Lower limit (mm)	95% Prediction Interval- Upper Limit (mm)	# of matched Markers	# of matched reference Markers
-6.000	-6.030	-6.138	-5.915	3	5
-4.000	-3.960	-4.127	-3.919	3	5
-2.000	-2.002	-2.118	-1.920	3	6
-1.000	-1.022	-1.115	-0.919	3	6
-0.500	-0.530	-0.614	-0.419	3	7
-0.250	-0.284	-0.364	-0.168	3	7
-0.100	-0.147	-0.213	-0.018	4	7
-0.050	-0.101	-0.163	0.032	4	7
-0.025	-0.085	-0.138	0.057	4	7
0.025	0.026	-0.088	0.107	4	7
0.050	0.044	-0.063	0.132	4	7
0.100	0.038	-0.013	0.182	4	7
0.250	0.154	0.137	0.333	3	7
0.500	0.505	0.388	0.583	3	7
1.000	1.038	0.888	1.085	3	6
2.000	2.052	1.889	2.088	3	5
4.000	4.067	3.888	4.096	3	5
6.000	5.959	5.884	6.107	3	5

Table C.6: The 95% Prediction Intervals of applied and observed Anterior (+about x-axis) and Posterior (- about x-axis) Tilt Rotations to the proximal femoral epiphysis in the computer simulation.

Anterior (+) Posterior (-) tilt Rotation of the Epiphysis (About x-axis)

Applied Rotation (°)	Observed Rotation (°)	95% Prediction interval - Lower limit (°)	95% Prediction Interval- Upper Limit (°)	# of matched Markers	# of matched reference Markers
-10.000	-10.174	-11.022	-8.989	4	7
-5.000	-5.081	-5.979	-4.158	3	7
-2.000	-2.026	-2.985	-1.227	4	7
-0.500	-0.601	-1.498	0.248	3	7
-0.333	-0.264	-1.333	0.413	4	7
-0.167	0.287	-1.169	0.577	4	7
0.167	0.231	-0.840	0.906	4	7
0.333	0.260	-0.675	1.071	4	7
0.500	0.333	-0.511	1.236	4	7
2.000	1.154	0.965	2.723	3	7
5.000	4.316	3.895	5.717	3	7
10.000	9.991	8.727	10.760	3	7

Table C.7: The 95% Prediction Intervals of applied and observed Internal (+ about y-axis) and External (- about y-axis) Rotations to the proximal femoral epiphysis in the computer simulation.

Internal (+) External (-) Rotation of the Epiphysis (About y-axis)

Applied Rotation (°)	Observed Rotation (°)	95% Prediction interval - Lower limit (°)	95% Prediction Interval- Upper Limit (°)	# of matched Markers	# of matched reference Markers
-10.000	-10.403	-10.787	-9.891	3	7
-5.000	-5.031	-5.524	-4.721	4	7
-2.000	-1.943	-2.380	-1.606	4	7
-0.500	-0.101	-0.812	-0.043	4	7
-0.333	-0.054	-0.638	0.131	4	7
-0.167	-0.246	-0.465	0.305	4	7
0.167	0.148	-0.117	0.652	4	7
0.333	0.386	0.057	0.826	4	7
0.500	0.544	0.231	1.000	4	7
2.000	1.961	1.793	2.568	4	7
5.000	5.240	4.909	5.712	3	7
10.000	10.626	10.079	10.975	4	7

Table C.8: The 95% Prediction Intervals of applied and observed Abduction (- about z-axis) and Adduction (+ about z-axis) Rotations to the proximal femoral epiphysis in the computer simulation.

Adduction (+) Abduction (-) Rotation of the Epiphysis (About z-axis)

Applied Rotation (°)	Observed Rotation (°)	95% Prediction interval - Lower limit (°)	95% Prediction Interval- Upper Limit (°)	# of matched Markers	# of matched reference Markers
-10.000	-10.010	-10.346	-9.772	4	6
-5.000	-5.035	-5.278	-4.764	4	6
-2.000	-2.063	-2.246	-1.750	3	7
-0.500	-0.410	-0.733	-0.240	4	7
-0.333	-0.288	-0.565	-0.072	4	7
-0.167	-0.124	-0.397	0.096	4	7
0.167	0.245	-0.061	0.432	4	7
0.333	0.340	0.107	0.600	4	7
0.500	0.519	0.275	0.768	4	7
2.000	1.745	1.785	2.281	4	6
5.000	5.157	4.799	5.313	4	6
10.000	10.136	9.808	10.382	3	6

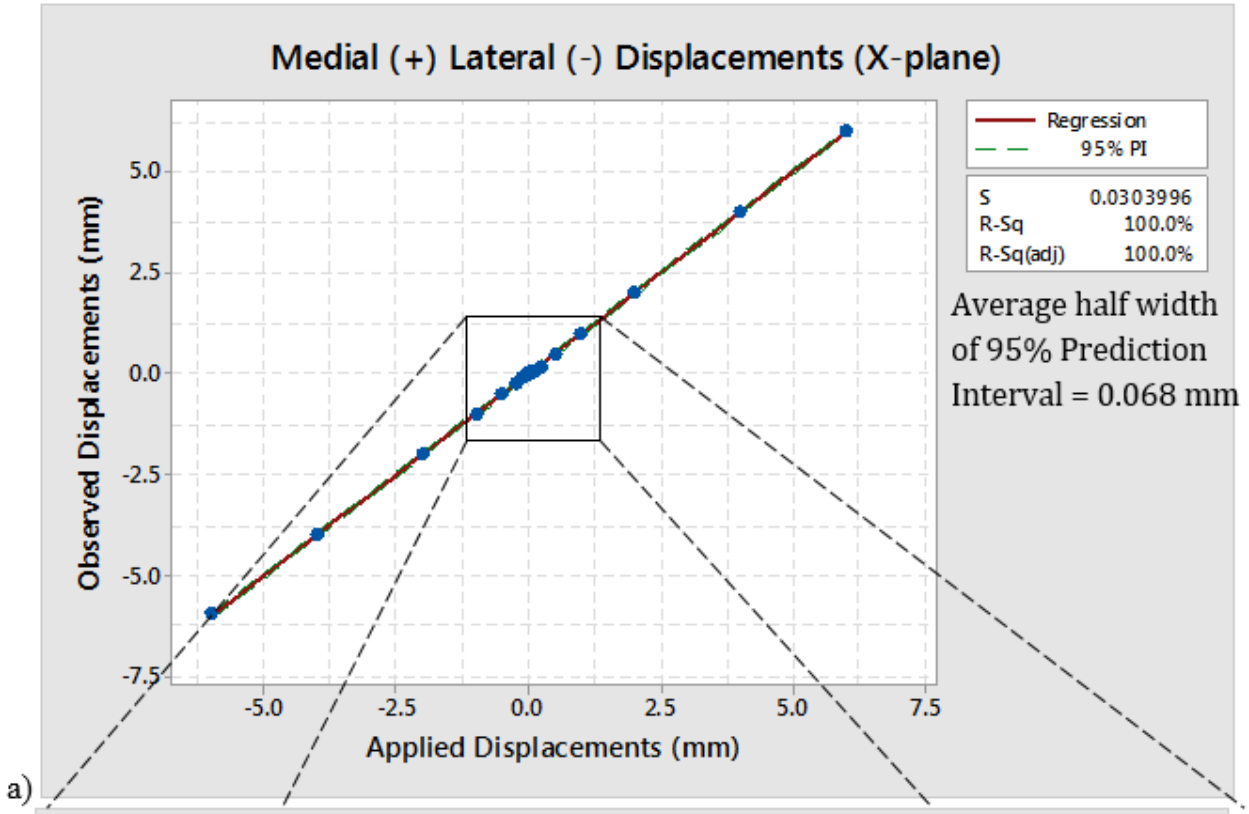

a)

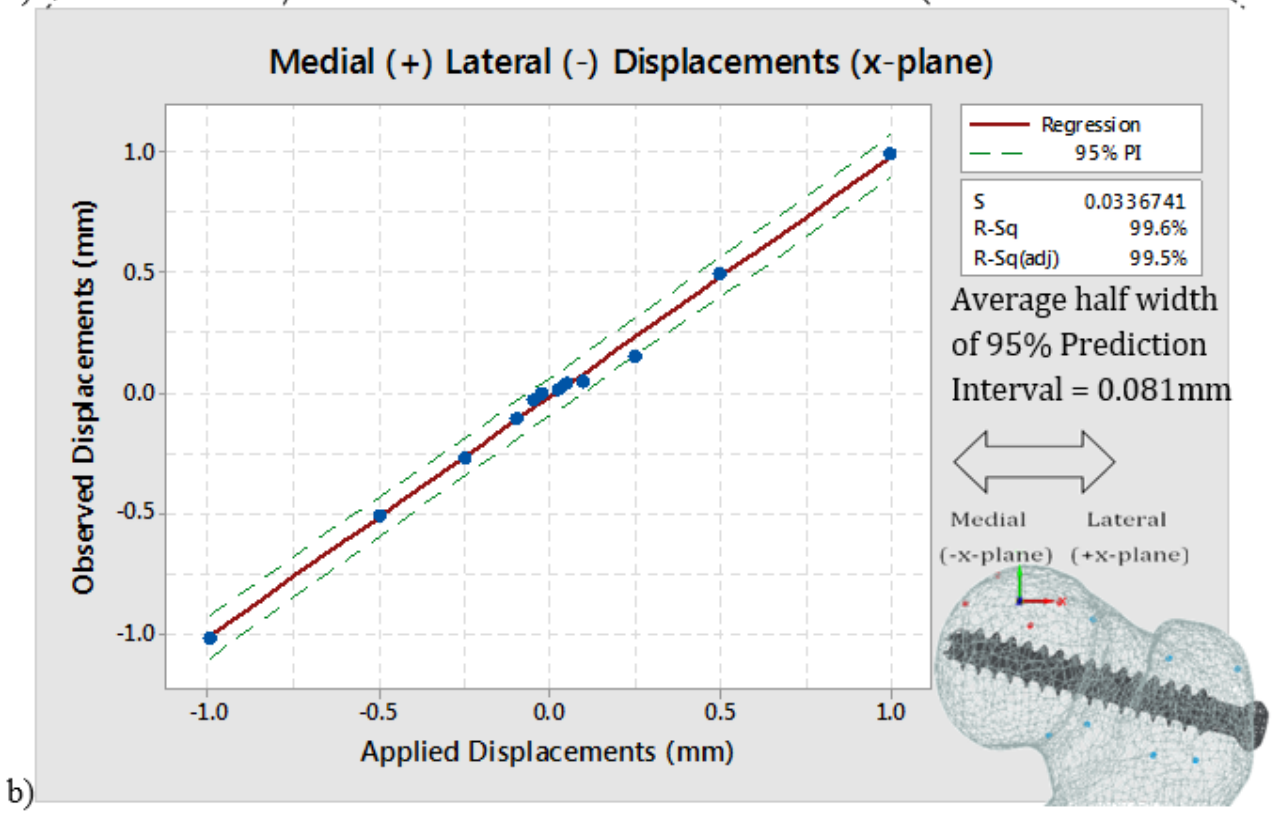

b)

Figure C.3: a) The 95% Prediction Intervals and the line of best fit between the applied and observed Medial (+) and Lateral (-) displacements ranging from -5.0 to +5.0 mm to the proximal femoral epiphysis in the computer simulation. b) Magnification of graph centered on -1.0mm to 1.0mm.

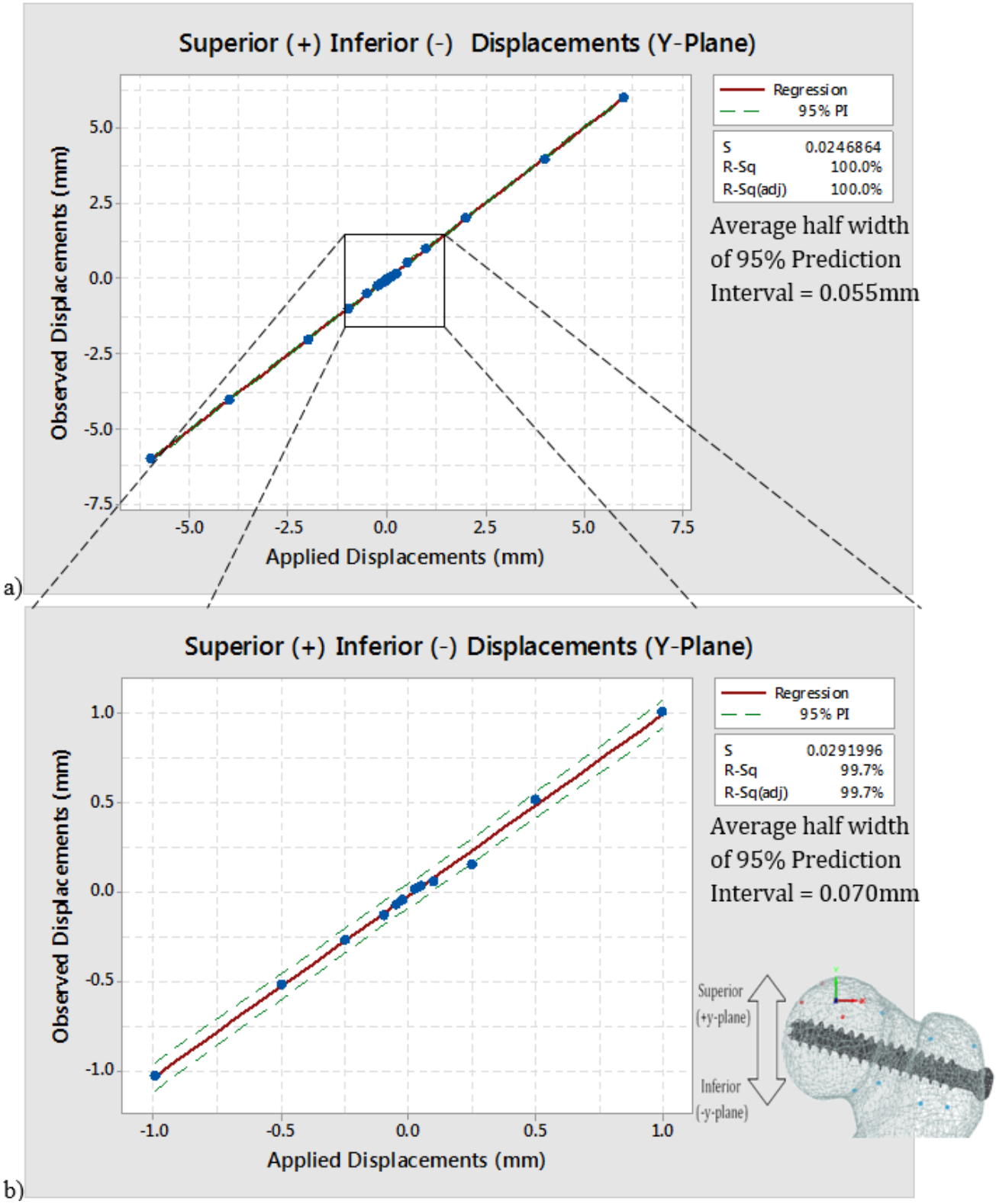

Figure C.4: a) The 95% Prediction Intervals and the line of best fit between the applied and observed Superior (+) and Inferior (-) displacements ranging from -5.0 to +5.0 mm to the proximal femoral epiphysis in the computer simulation. b) Magnification of graph centered on -1.0mm to 1.0mm and graphic presentation of nature of movement.

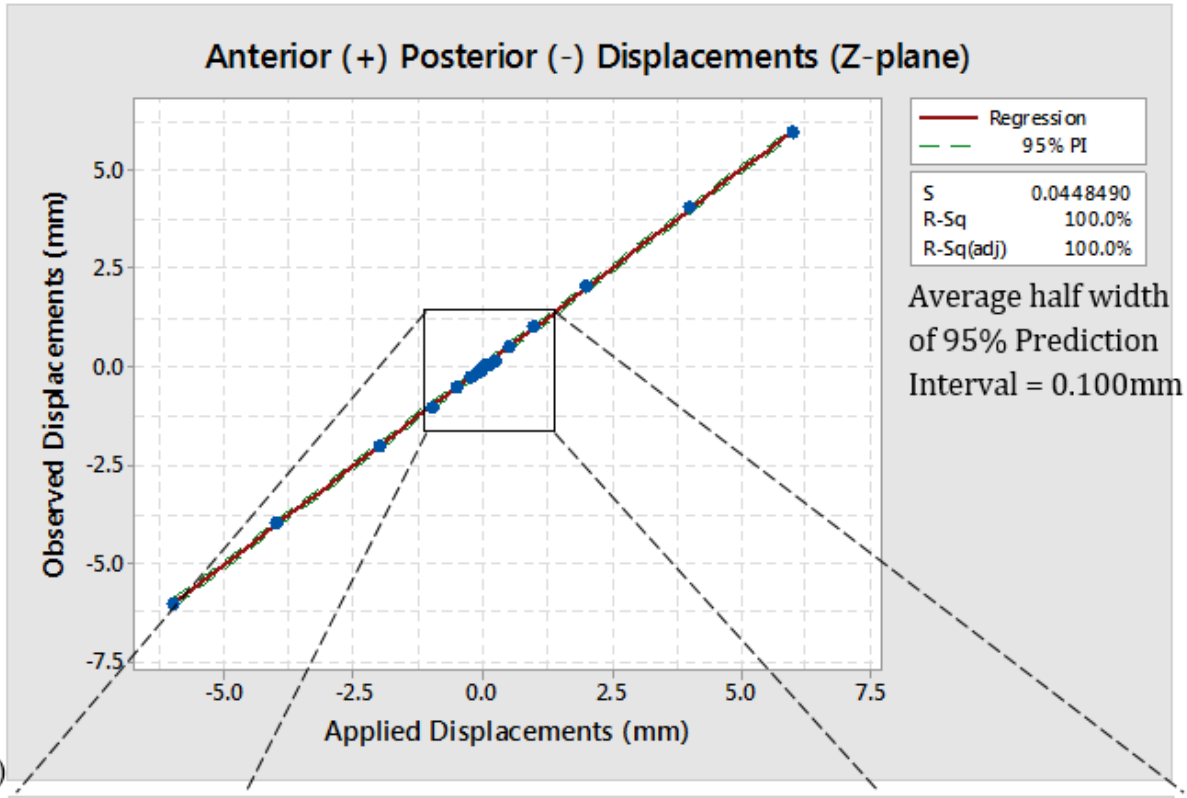

a)

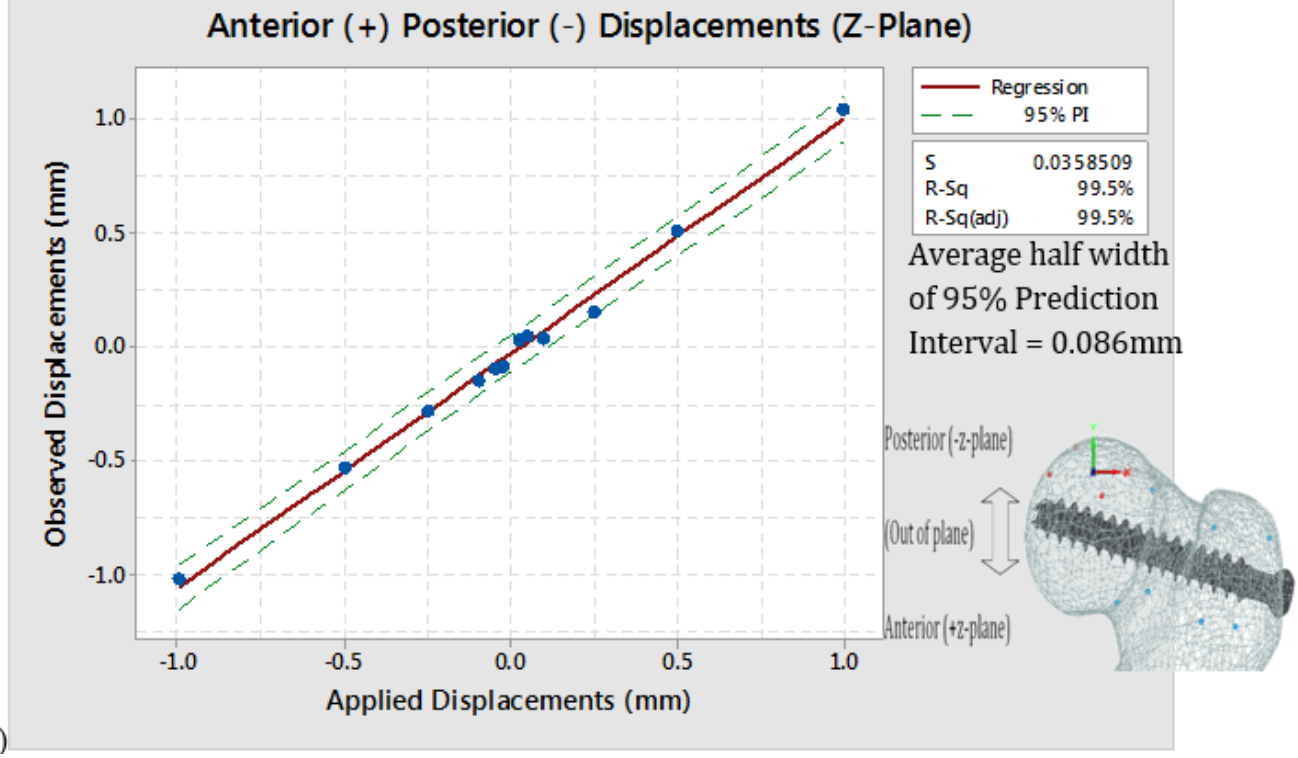

b)

Figure C.5: a) The 95% Prediction Intervals and the line of best fit between the applied and observed Anterior (+) and Posterior (-) displacements ranging from -5.0 to +5.0 mm to the proximal femoral epiphysis in the computer simulation. b) Magnification of graph centered on -1.0mm to 1.0mm and graphic presentation of nature of movement.

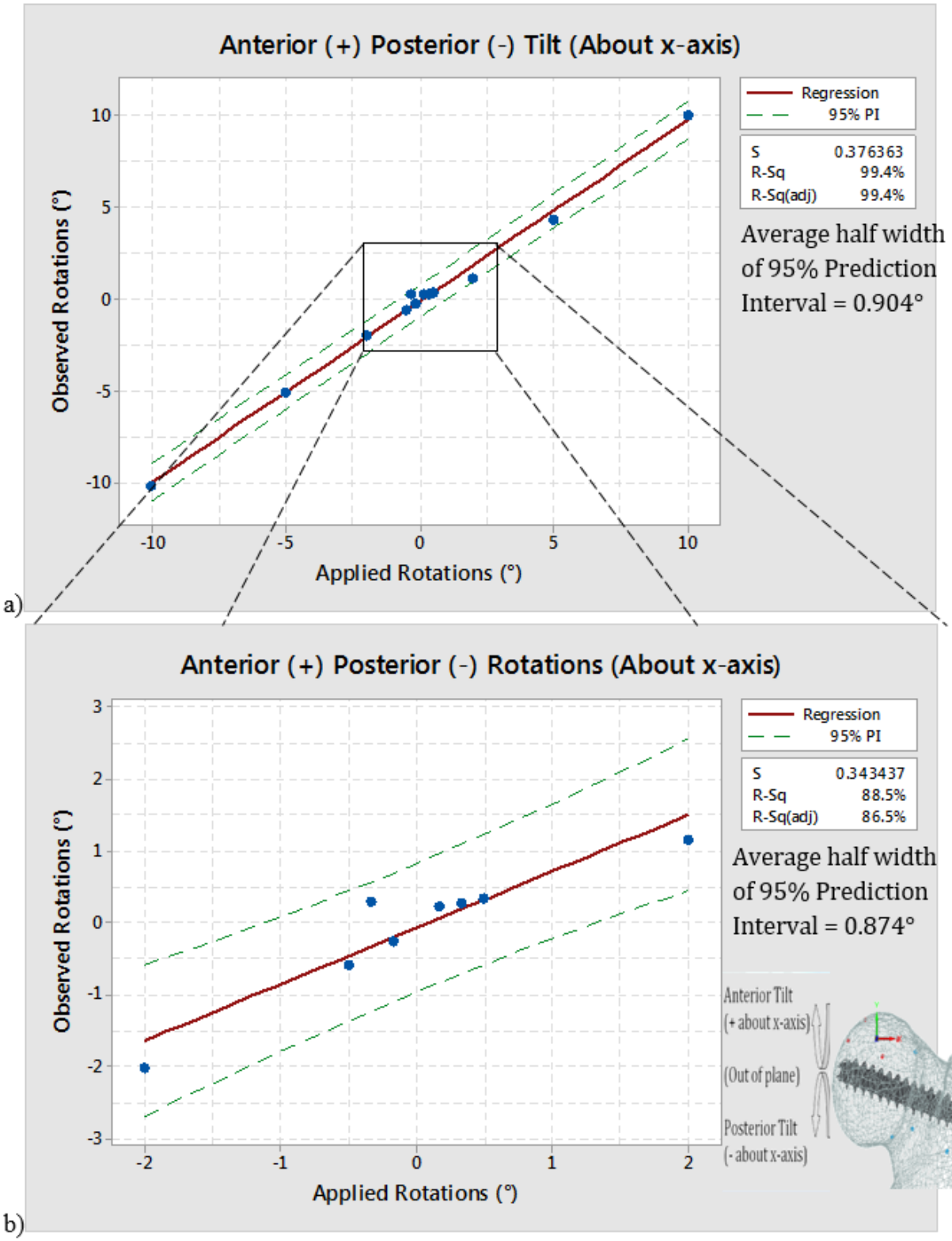

Figure C.6: The 95% Prediction Intervals and the line of best fit between the applied and observed Internal (-) and External (+) rotations to the proximal femoral epiphysis in the computer simulation. B) Magnification of the graph ranging from -2.0° to +2.0° and graphic presentation of nature of movement.

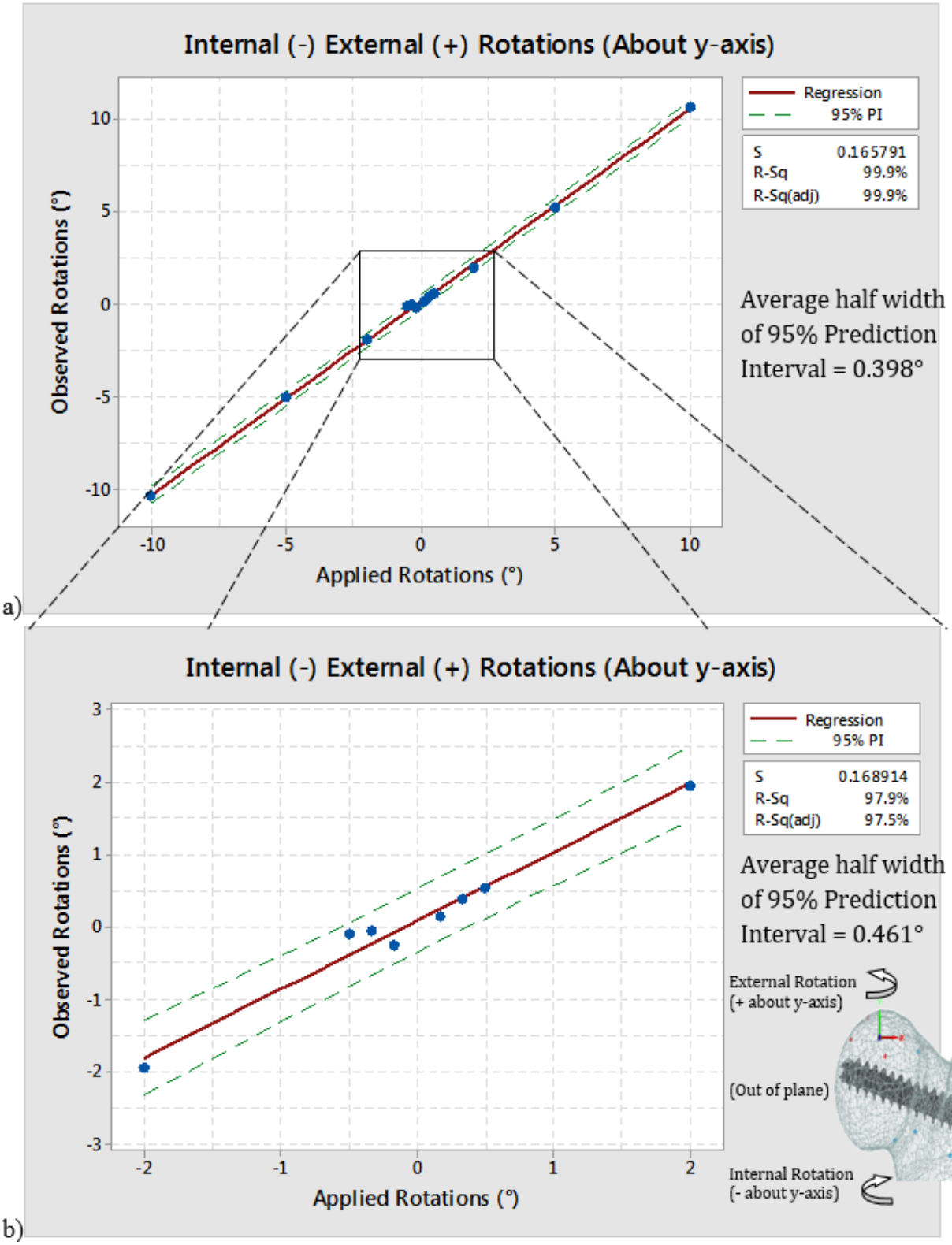

Figure C.7: a) The 95% Prediction Intervals and the line of best fit between the applied and observed External (+) and Internal (-) rotations to the proximal femoral epiphysis in the computer simulation. B) Magnification of the graph ranging from -2.0 to +2.0° and graphic presentation of nature of movement.

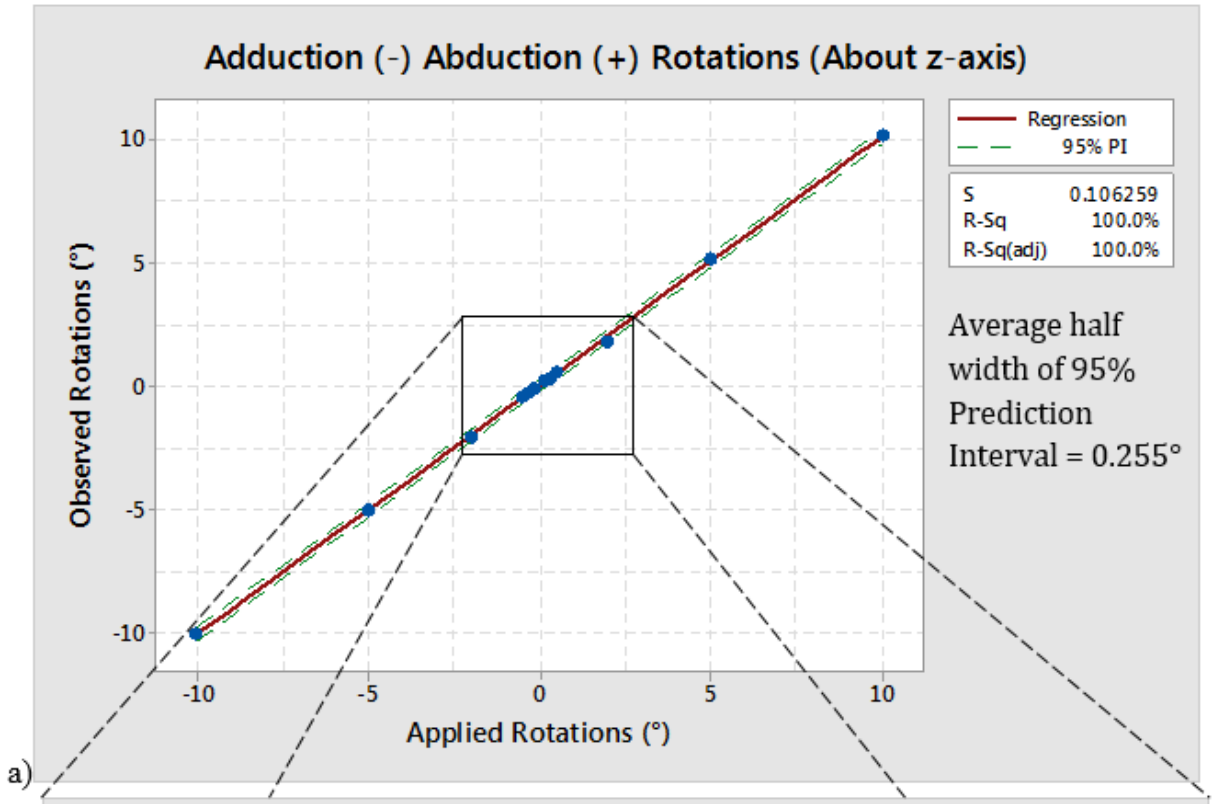

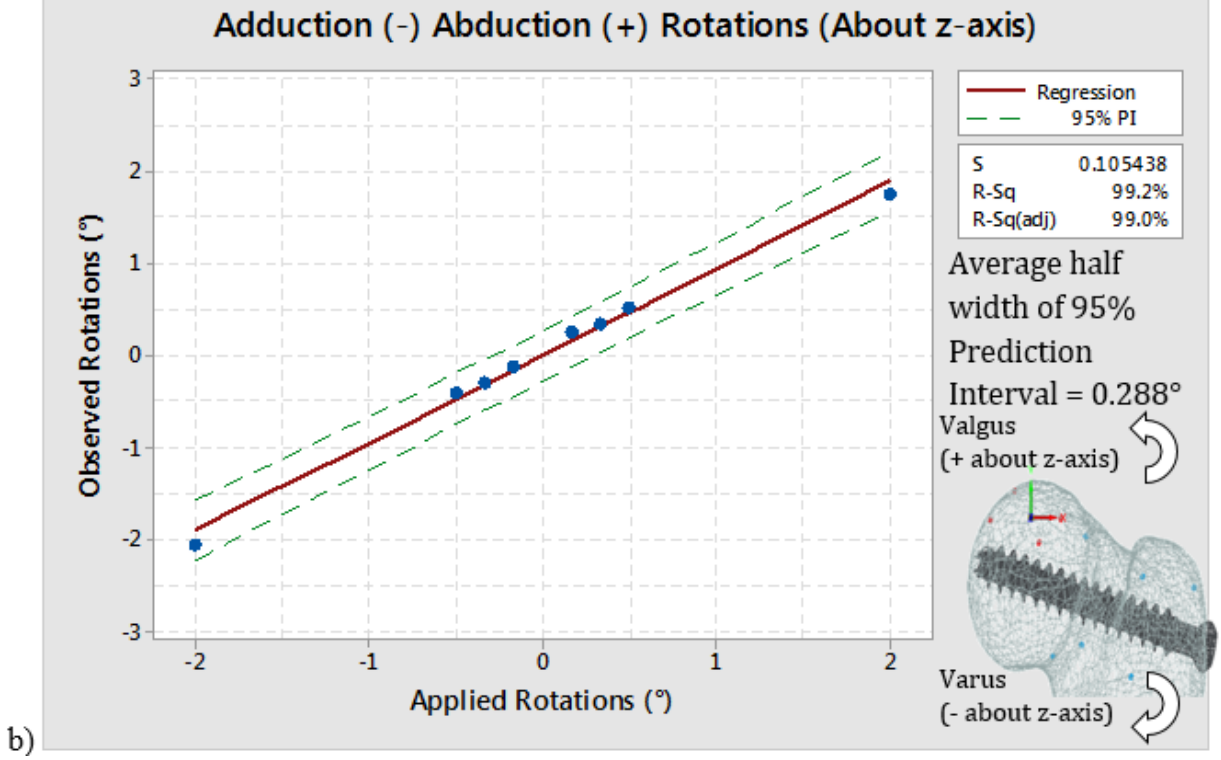

Figure C.8: a) The 95% Prediction Intervals and the line of best fit between the applied and observed Adduction (-) and Abduction (+) rotations to the proximal femoral epiphysis in the computer simulation. B) Magnification of the graph ranging from -2.0 to +2.0° and graphic presentation of nature of movement.

RECOMMENDATION

The results of the computer simulation firstly suggest that the proximal femur although dimensionally constrained, provides sufficient spatial freedom to construct bead clusters with Condition Numbers below 150, ISO 16087. The range of migrations, although superfluous in relation to what is indicative for post-surgical fusion, were prescribed to substantiate the validity of the developed marker cluster configuration. The absence of significant bead occlusion, promotes the utility of this technique in the SCFE model. Table C.9 summarizes the results from the computer simulation study.

Table C.9: Summary of RSA accuracy found in the computer simulation study.

Nature of Movement Applied	**Migration ranging from -6.00 mm to +6.0 mm**	**Migration ranging from -1.0 mm to +1.0 mm**
Mediolateral Movement	0.068 mm	0.081 mm
Inferiosuperior Movement	0.055 mm	0.070 mm
Anterioposterior Movement	0.100 mm	0.086 mm
	Rotations ranging from -10.00° to +10.00°	**Rotations ranging from -2.00° to +2.00°**
Anterior/Posterior Tilt	0.904°	0.874°
Internal/External Rotation	0.398°	0.461°
Varus/Valgus	0.255°	0.288°